ABSTRACT

TOMKINS, LAURA MARY. Synthesis of Radar-Observed Characteristics, Storm Structures, and Surface Snowfall Rates in 10+ Years of Northeast US Winter Storms. (Under the direction of Dr. Sandra Yuter).

Accurate forecasts of snowfall are crucial to minimize the impacts of winter weather. Current numerical weather prediction models struggle to accurately forecast the timing, intensity, and duration of snow. We use over 11 seasons of meteorological observations in the northeast US encompassing 264 days with substantial regional snowfall to investigate several characteristics of winter storms and their associations with high snow rates at the surface. Regional radar mosaics derived from the National Weather Service operational NEXRAD network are used to assess how mesoscale snow bands impact the surface snowfall rate. We developed two new objective image processing techniques as part of this work; one for identifying and reducing the visual prominence of mixed precipitation (rain with snow), and another for identifying locally-enhanced reflectivity features. Hourly surface snowfall rates from ASOS stations in the northeast US are compared to hourly statistics of locally-enhanced feature area in the vicinity of the surface weather measurements. Our results show that heavy snow rates (> 2.5 mm hr^{-1} liquid water equivalent) are rare and are not consistently associated with locally enhanced reflectivity features (i.e. snow bands). Detailed vertical cross-sections of winter storms from research radars demonstrate that snow particles do not fall straight down, rather they are blown sideways 10s of km as they fall. Ice streamers with heavier snow emanating from generating cells near cloud top are tilted and smeared on the way to the surface. In the absence of vertical column continuity in reflectivity, there is not a direct relationship between scanned operational radar observations above the ground and surface snow rates.

In addition to the radar reflectivity fields, we examine storm structure features related to vertical motions at 10s of km and 100s of km spatial scales. The observed radar Doppler velocity field is used to detect wave features (10s of km scale), known as velocity waves, to explore the relationship between propagating bands of upward and downward motions and surface snow rates. When comparing the distributions of snow rates from times with and without velocity waves, we found that times with waves have a slightly higher liquid equivalent snow rate (median: 0.76 mm hr^{-1}) than times without waves (median: 0.3 mm hr^{-1}). Low pressure center tracks derived from ERA5 reanalysis data are used to visualize the snow rates in a Lagrangian framework relative to the low pressure center. Patterns of snow rates that are generally consistent with the expected spatial patterns of frontogenesis at 100s of km scales. 86% of heavy surface snow rates (> 2.5 mm hr^{-1} liquid water equivalent) are observed when

the surface pressure is decreasing rather than increasing.

This comprehensive analysis gleaned from weather radar, surface stations, and focused observations from research aircraft highlights the large uncertainties and ambiguities in interpreting observed radar reflectivity in snow and the importance of using large sample sizes to gain representative physical insights.

Key implications of our findings are that primary bands (snow bands longer than 200 km that are persistent over several hours) are useful in identifying regions with heavier snow rates since primary bands are related to strong frontogenesis. In regions with weak to no frontogenesis, multi-bands (sets of parallel snow bands < 200 km in length) are a distraction since they are rarely associated with heavier snow rates.

Synthesis of Radar-Observed Characteristics, Storm Structures, and Surface Snowfall Rates in 10+ Years of Northeast US Winter Storms

by
Laura Mary Tomkins

A dissertation submitted to the Graduate Faculty of
North Carolina State University
in partial fulfillment of the
requirements for the Degree of
Doctor of Philosophy

Geospatial Analytics

Raleigh, North Carolina
2024

APPROVED BY:

Dr. Matthew Parker	Dr. L. Baker Perry
Dr. Mirela Tulbure	Dr. Sandra Yuter Chair of Advisory Committee

ACKNOWLEDGEMENTS

First and foremost, I would like to thank by advisor, Dr. Sandra Yuter, for her guidance and mentorship over the last 10+ years. This work would not have been possible without her and I am grateful for the invaluable opportunities she has provided for me. I appreciate her encouragement to challenge myself and grow, not only as a scientist but also as an individual.

I would also like to thank my committee members, Dr. Matthew Parker, Dr. Baker Perry, and Dr. Mirela Tulbure, for generously dedicating their time to serve on my committee and offering valuable insights. Special thanks also to Dr. Matthew Parker for his crucial instruction in mesoscale meteorology.

Many, many thanks to Dr. Matthew Miller for enlightening conversations which helped to advance this work, and for always being available to solve my never-ending technical problems. Similarly, thank you to both Luke Allen and Kevin Burris for all their help sharing data and methods, and general insightful conversations.

I am grateful to all past and current members of the Environment Analytics research group, without whom, this work would not have been possible. Thank you to Nicole Corbin, Nicole Hoban, and Sara Sienkiewicz whose contributions to previous work were invaluable in shaping this project into its current form. Thank you to Anya Aponte-Torres, Declan Crowe, Jordan Fritz, Cameron Gilbert, Robert Harley, McKenzie Peters, and McKenzie Sevier for all their help with data processing. Additional thanks to Logan McLaurin for providing helpful feedback on permutation testing. Finally, thank you to Rachel Kennedy and Laura Kent who were both wonderful office mates and provided great encouragement.

Additional thanks to Dr. Brian Colle, Phillip Yeh, and Erin Leghart at Stonybrook University and Dr. David Novak at the Weather Prediction Center for providing useful feedback on this work.

I would like to thank my parents, Lynn and Glyn Tomkins, for their consistent and unwavering support. None of this would have been possible without the opportunities that they provided to me. To all my friends, to my cat, Freddie, to my siblings, Anna and TomTom, to my best friend, Kara, and to my partner, Joel, I am so thankful for all your support and serving as a constant source of relief during challenging times.

Thank you to the Center for Geospatial Analytics (CGA) for the opportunity to take part in a unique, multi-disciplinary program. I am additional grateful to the CGA, NSF, and NASA for their financial support. Finally, I would like to thank the NASA IMPACTS team for all their hard work collecting and preparing the data used in this work.

TABLE OF CONTENTS

LIST OF TABLES

LIST OF FIGURES

Chapter 1

Introduction

1.1 Motivation

Winter storms in the northeast US cause significant societal and economic disruptions to the densely-populated regions of the mid-Atlantic and New England (Kocin and Uccellini 2004; Novak et al. 2023). The US Department of Transportation estimates that weather-related flight cancellations are twice as common in the winter compared to the summer (Guarino and Firestine 2010).

Accurate forecasts of winter storms are crucial for school districts, emergency managers, and transportation agencies to minimize the impacts from winter weather. Current numerical weather prediction models struggle to accurately predict the timing, intensity, and duration of snow. It is common for snowfall accumulation forecasts to have a range of a factor of two or more (i.e. "3 to 6 inches of snow expected") which complicates the planning for storm impacts. Small shifts of 10s of km in the cyclone track and/or temperature gradients can cause changes in the location and timing of the rain-snow line and whether snow falls over a given metropolitan area or during rush hour. Additionally, the forecast skill varies from event to event, so while one event might be well-forecast, the next may not be (Novak et al. 2023).

Snowfall accumulations are dependent on the snow rate which also has important societal impacts. Heavy snow rates make it difficult for snow plows to keep up with clearing roads and create poor visibility conditions (Rasmussen et al. 1999). Additionally, heavy snow rates can increase the risk for avalanches (Schweizer et al. 2003).

The general lack of skill in forecasting winter storms has motivated research to understand the physical processes within winter storms. In this study, we address basic questions about the structural characteristics of winter storms and the impact they have on surface snow fall.

1.2 Definitions and Concepts

Descriptions of key terms for non-meteorologist readers.

- **Radar reflectivity**: Active remote sensing measure of the magnitude of backscattered energy related to the characteristics of the set of precipitation particles in a scanned volume. In rain, radar reflectivity is a function of the number and size distribution of raindrops in a given volume. Generally, higher reflectivity values are associated with higher total mass of raindrops per unit volume. In snow, the relation between volumetric mass of ice and reflectivity is not monotonic and varies with the sizes, shapes, and densities of ice particles in a volume.

- **Doppler velocity**: Active remote sensing measure of the component along the radar beam of the precipitation-sized particle velocities in a given volume. Positive indicates motion away from the radar and negative indicates motion towards the radar. For radars that scan nearly at horizontal, Doppler velocity is indicative of horizontal wind motion. For radars that point vertically, Doppler velocity is the sum of the vertical air motions (upwards or downwards) and fall speed of precipitation (downwards).

- **Instability**: A condition where an air parcel continues to rise if perturbed upward from it's initial position. Instability is one cause of upward vertical motions and thus a contributing factor in cloud and precipitation development. There are many types of instabilities in the atmosphere associated with different vertical profiles of temperature, humidity, and wind.

- **Frontogenesis**: The strengthening of a weather front. Frontogenesis occurs when the temperature gradient along a front intensifies. Frontogenesis drives a circulation with upward motion and is often accompanied by instability. Locations with strong frontogenesis are usually favorable for precipitation development.

- **Vapor Deposition**: Water substance phase change from vapor to ice. Vapor deposition is a key process in the initial formation of ice crystals and their growth from cloud-size (< 0.2 mm diameter, too small to fall) to precipitation-size (large enough to fall) particles. The geometric shape of the depositional growth is a function of temperature and humidity.

- **Riming**: A process where super-cooled liquid droplets freeze on contact with precipitation-size ice crystals. Riming adds mass to ice particles about 16x faster than vapor deposition.

- **Aggregation**: A process where existing snow crystals collide and jumble together. Aggregation yields individually larger ice particles but since it just rearranges the existing mass, it doesn't change the total ice mass in a given volume.

1.3 Background

Winter storms in the northeast US often develop elongated features of enhanced reflectivity referred to as *snow bands*. Bands that are longer than 200 km are called primary bands and are associated with strong frontogenesis at low- and mid-levels in the storm(Fig. 1.1; Novak et al. 2004, 2010; Ganetis et al. 2018). Bands that are shorter than 200 km and typically occur in groups are known as multi-bands. Most previous work related to winter storms has focused on primary bands and understanding their associated physical mechanisms (Novak et al. 2004, 2008, 2009, 2010; Novak and Colle 2012; Kenyon et al. 2020; Baxter and Schumacher 2017; Stark et al. 2013). The relationship between multi-bands and frontogenesis is not clear as multi-bands are found in environments with strong, positive to negative frontogenesis (Fig. 1.2; Ganetis et al. 2018; Nicosia and Grumm 1999; Connelly and Colle 2019). Shields et al. (1991) and Ganetis et al. (2018) have suggested conditional symmetric instability as a mechanism for multi-band production but the relative importance of this type of instability in comparison to other types of instabilities is a topic of active research. Hoban (2016) found winter storms in the northeast US with multi-bands often exhibited wave-like features in the Doppler velocity field, known as velocity waves (Miller et al. 2022), suggesting multi-bands may be associated with wave activity. The lack of consistent signal between multi-bands and forcing mechanisms such as frontogenesis and instability makes these snow bands particularly difficult to forecast.

As part of this study, we examine recent field campaign observations of the detailed 3D structures of winter storms including vertically-pointing radar observations from aircraft deployed during the recent NASA IMPACTS field campaign (McMurdie et al. 2022) and vertical cross-sections from ground-based radars at Stonybrook University (KASPR; Oue et al. 2017). These research-quality observations provide new insights into typical vertical structures in winter storms including physical processes, and their relation to snow bands as detected in the coarser resolution radar data from the National Weather Service operational radars.

Most previous work on snow bands in northeast US winter storms has focused on case studies or small sample sizes with high snowfall accumulations (Picca et al. 2014; Varcie et al. 2022; Ganetis and Colle 2015; Novak et al. 2008; Han et al. 2007; Colle et al. 2014; Clark et al. 2002; Lackmann and Thompson 2019). While case studies can provide valuable information, they may not be representative of the relative importance of the roles of different physical processes in a large sample of winter storms. Case studies often focus on extreme events with

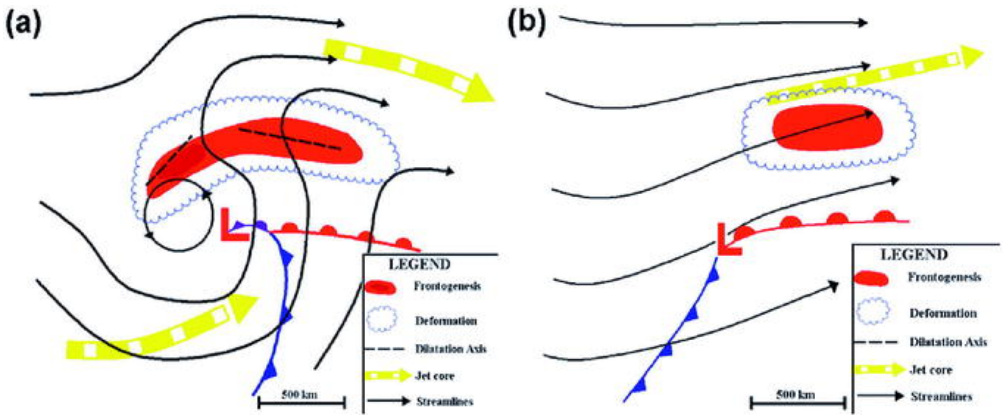

Figure 1.1: Conceptual diagram of the environments associated with (a) primary band event and (b) non-banded event. Regions of frontogenesis are shaded in red. Other key features described in legend. Figure 15 from Novak et al. (2004).

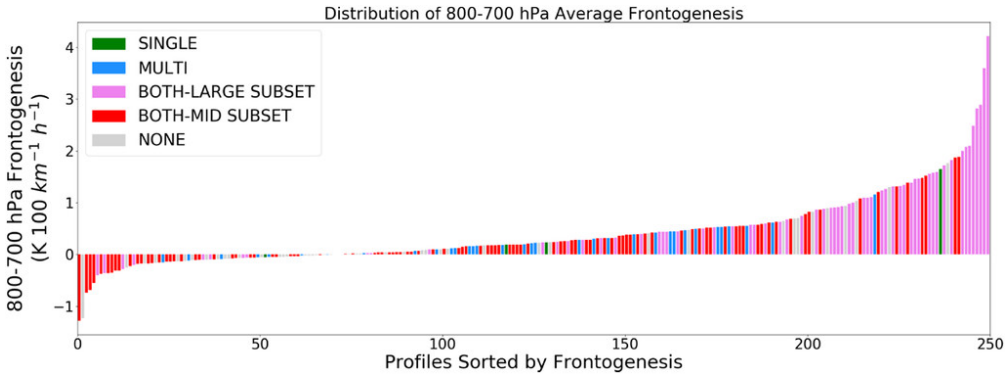

Figure 1.2: Distribution of 700-800 hPa frontogenesis for each event colored by types of bands present. Figure 10 from Ganetis et al. (2018).

the most intense impacts which may not be generalizable to more typical events.

A complicating factor in the analysis of winter storms using weather radar observations is the interpretation of radar reflectivity in snow. In warm-season precipitation systems it is reasonable to deduce that locally-enhanced radar reflectivity features are associated with stronger rain rates at the surface but that is not necessarily the case in cool-season precipitation systems. In snow, changes in radar reflectivity do not necessarily equate to changes in mass per unit volume as in rain (Table 1.1). Processes such as aggregation and partial melting increase the radar reflectivity but do not change the mass per unit volume which complicates the interpretation of radar reflectivity in winter storms.

Table 1.1: Table of microphysical processes and their associated change to mass per unit volume (IWC/LWC) and to radar reflectivity.

Process	**Change to IWC/LWC**	**Change to radar reflectivity**
Riming	Increase	Increase
Vapor Deposition	Increase	Increase
Collision-Coalescence	Increase	Increase
Condensation	Increase	Increase
Aggregation	*No change*	Increase
Melting	*No change*	Increase
Evaporation	Decrease	Decrease
Sublimation	Decrease	Decrease
Freezing	*No change*	Decrease
Fragmentation	*No change*	Decrease
Raindrop Breakup	*No change*	Decrease

Observations of ice water content (IWC) and radar reflectivity collected during research flights as part of the SNOWIE field campaign in the mountains of Idaho (Tessendorf et al. 2019) describe the relationship between IWC and reflectivity in ice clouds and light snow (Fig. 1.3; Zaremba et al. 2023). For a given radar reflectivity value, there is a wide range of possible associated IWC values. Similarly, for a given IWC value, there is a wide range of possible radar reflectivity values. Overall, for these data obtained in light falling snow as IWC increases radar reflectivity increases but even for this simple case without much aggregation or any partial melting the spread of the values makes it difficult to quantify volumetric ice mass as a function of radar reflectivity better than a factor of 2.

Snow falls slowly (~ 1 m s^{-1}) compared to rain (~ 5 m s^{-1}) so it is more easily transported by the horizontal winds of $\geq$10 m s^{-1} and rarely falls straight to the surface further complicating the interpretation of radar reflectivity aloft. The work we present here demonstrates that locally-

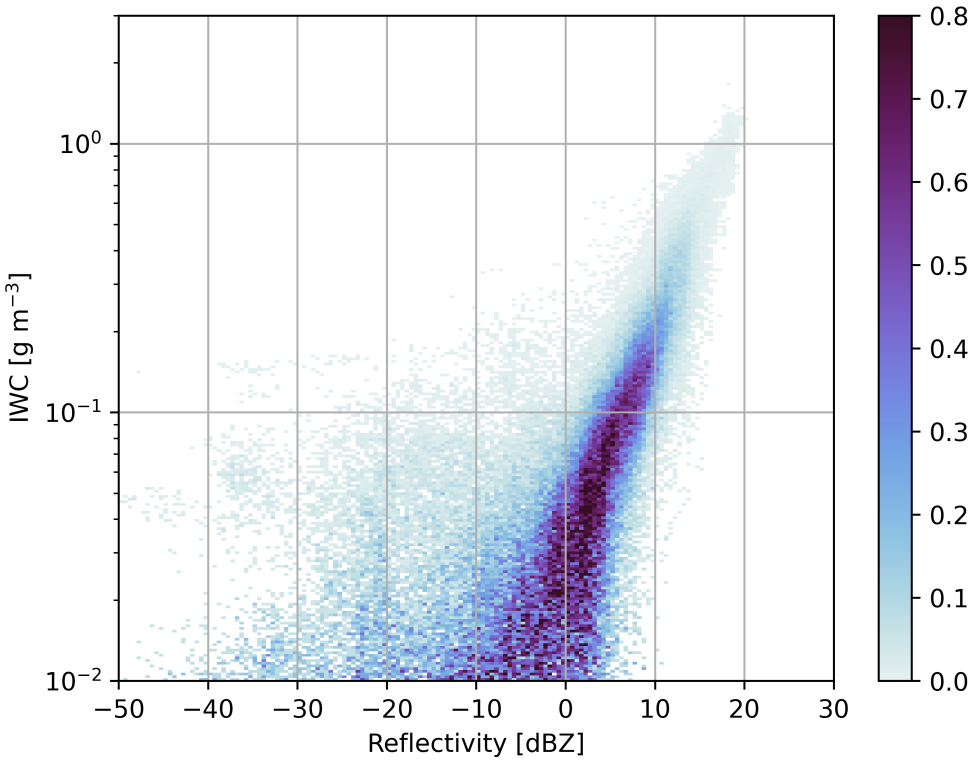

Figure 1.3: 2D distribution of ice water content (IWC) [g m^{-3}] from Nevzorov liquid water and total water content probe and radar reflectivity [dBZ] from the W-band Wyoming Cloud Radar (WCR) deployed on the University of Wyoming King Air (UWKA) aircraft during the SNOWIE field campaign. Figure 6 from Zaremba et al. (2023).

enhanced reflectivity features are rarely associated with heavy surface snow rates which argues that bands not strongly-forced (by frontogenesis or otherwise) are distracting when it comes to nowcasting (forecasting out to less than 6 hours) regions with heavy snow rates.

1.4 Thesis Organization

The overarching goal of this study is to explore and understand the relationships between surface snow rates and locally-enhanced reflectivity features (i.e. snow bands), Doppler radar observed velocity waves, and storm structures. Previous research related to storm structures and snow rates has primarily focused on the portions of winter storms with strong frontogenesis. We use a large sample size to address the full range of conditions in northeast US storms yielding at least 1-inch of snow in a 24 hour period. We use observations from 264 storm days in the northeast US from over 10 years (2012-2023) to ensure we are studying the relationships over a representative sample. To explore the relationship between locally-enhanced reflectivity features and surface snow rates we use regional radar mosaics created from National Weather Service NEXRAD radars and hourly precipitation rates from ASOS stations. The relationship between velocity waves and surface snow rates is examined by comparing the precipitation rates during hours when waves were present to hours when waves were not present. To understand the relationship between storm structures and surface snow rates, we analyze distributions of precipitation rate related to the distance from the storm's low pressure center and the pressure tendency.

Chapter 2 will document all data and methods used to analyze winter storms with the exception of two techniques that have been published and submitted as individual manuscripts and are included in their own separate chapters. Chapter 3 describes our technique for image muting radar reflectivity data and has been published in *Atmospheric Measurement Techniques*. Chapter 4 explains the method we developed to objectively identify locally-enhanced features in the radar data and is in review in *Atmospheric Measurement Techniques*. Both of these chapters include their own relevant introduction data, and methods sections. Chapter 5 will present the results from examining locally-enhanced reflectivity features and velocity waves in radar data and their relationship to surface snowfall rates. Chapter 6 examines the relationship between storm structures and surface snowfall rates. Chapter 7 will present the summary and conclusions.

Chapter 2

Data and Methods

To understand how different characteristics of winter storms impact the surface snowfall, we combine several types of observations for a large sample size of observed storms. This chapter as well as chapters 3 and 4 document both the datasets and methodology used in this study.

Since two papers detailing specific methods have already been accepted and submitted, the material on Data and Methods is organized in the following manner. This chapter covers data and methods that are relevant to the portions of the work that has not yet been submitted for publication. Chapter 3 covers our image muting technique to remove regions of melting and mixed precipitation in our analysis and Chapter 4 covers our algorithm for objectively identifying enhanced reflectivity in radar data. These chapters containing papers are self contained in the sense that they include their own Introduction, Data and Methods, Results, and Summary sections.

2.1 Winter Storm Dataset

We created a dataset of northeast US winter storm events between 2012 and 2023 following the methodology of Hoban (2016) and Ganetis et al. (2018). We define a winter storm as any date between October-March 2012-2023 where at least 1 inch of snow was reported over a 24-hour period at at least two out of 14 stations shown in Fig. 2.1. We used a threshold of 1 inch to include a wide range of storms in our analysis and not only those that produce a large amount of snow accumulation. The daily data at each station was gathered from the Global Historical Climatology Network daily (GHCNd) database (Menne et al. 2012). We selected the stations in Fig. 2.1 to include storms that were impactful to the more densely-populated regions of the

northeast US and to avoid identifying events that were lake-effect snow events. Our sample consists of 264 storm days from 2012-2023. The years 2012-2023 were chosen as this is when we have dual-polarization radar data available. Using radar data with dual-polarization products available allows us to "image mute" and remove remove melting and mixed precipitation observations, often confused for heavy snow, from our analysis (discussed in Sec. 2.2.2). The full list of storms is includes in Appendix A.

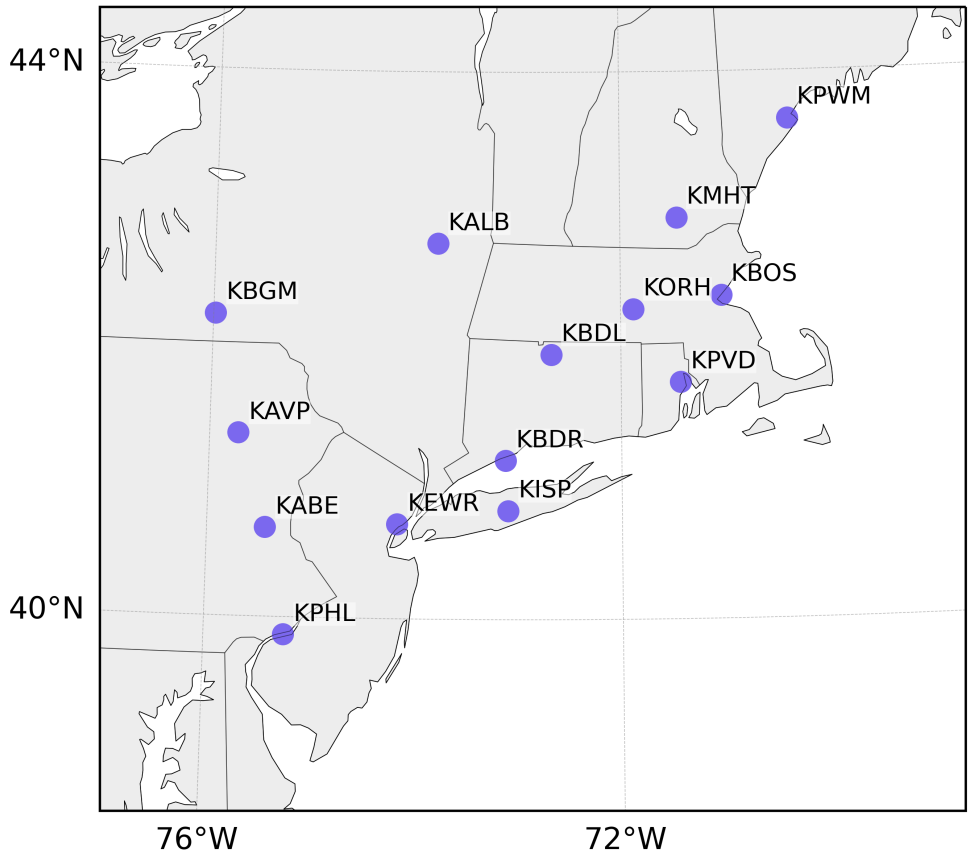

Figure 2.1: ASOS stations where daily snowfall accumulation is used to define a winter storm in this analysis.

2.2 Radar Observations

We use radar observations from the National Weather Service (NWS) Next-Generation Radar (NEXRAD) network in the northeast US to analyze features of the radar reflectivity and Doppler velocity field in winter storms. All NEXRAD data were obtained from the NOAA archive on

Amazon Web Services (Ansari et al. 2018). Our radar data processing utilizes the open-source Python Atmospheric Radiation Measurement (ARM) Radar Toolkit (Py-ART) developed by the Department of Energy ARM Climate Research Facility (Helmus and Collis 2016).

The NEXRAD radars scan 360° in azimuth over a set of elevation angles. In this analysis we primarily use the elevation angle at 0.5° above the horizon. The radar beam widens the further it is from the radar itself. This means that observations closer to the radar have a higher spatial resolution than those further away and the observations further away from the radar are more susceptible to non-uniform beam filling.

2.2.1 Regional Radar Mosaics

We combine data from multiple radars in the northeast US into a continuous mosaic. The radars used to create the mosaics are presented in Table 2.1 and shown in Fig. 2.2. The procedure to create the regional radar mosaics is detailed in Sec 3.2.1.

Table 2.1: List of radar names and locations used in the analysis. The central radar, KOKX, is annotated in bold.

Radar	Location
KOKX	**New York City, NY**
KBOX	Boston, MA
KDIX	Philadelphia, PA
KDOX	Dover, DE
KENX	Albany, NY
KGYX	Portland, ME
KTYX	Montague, NY
KBGM	Binghamton, NY
KBUF	Buffalo, NY
KLWX	Sterling, VA
KCCX	State College, PA
KCXX	Burlington, VT

2.2.2 Image muting of mixed precipitation

One goal of this project is to understand the relationship between locally-enhanced reflectivity features and surface snow rates. However, enhanced radar reflectivity in winter storms does not always indicate regions of enhanced ice mass. Transitions between snow, rain, and partially-melted snow are common in winter storms which complicates the interpretation of

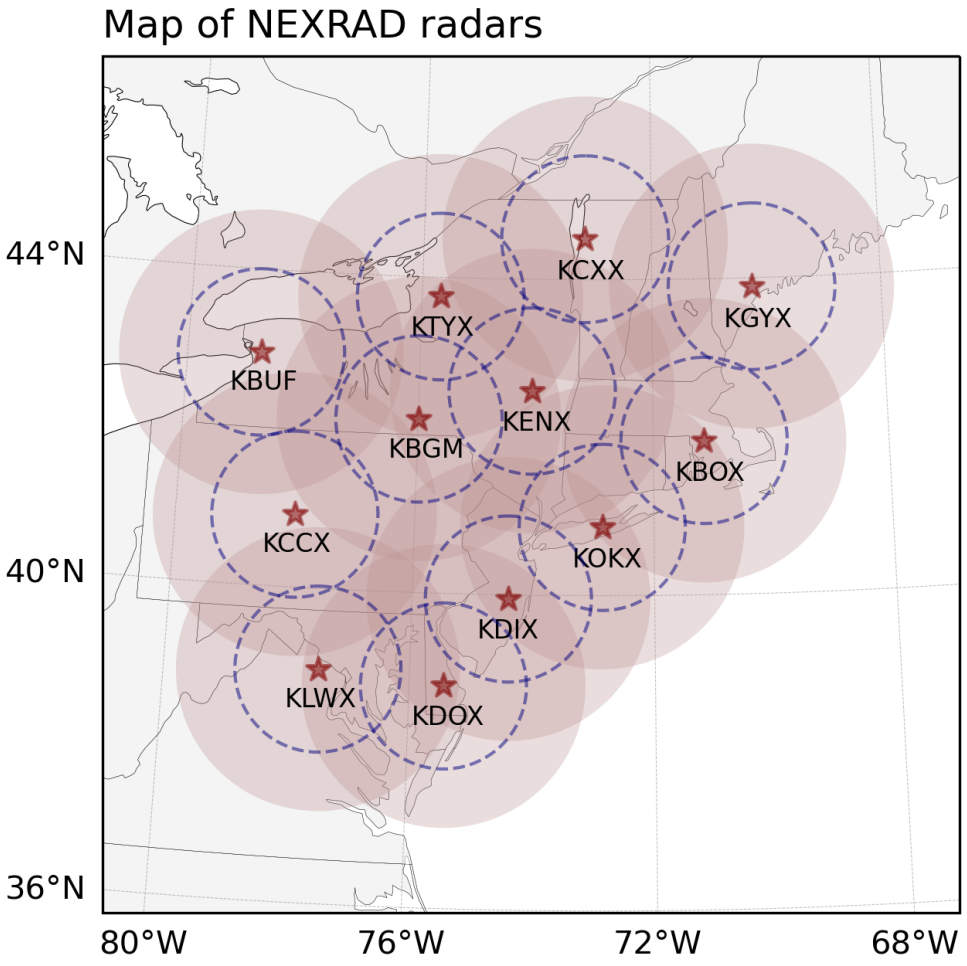

Figure 2.2: Map of NEXRAD radar locations (red stars). Shaded circles indicate 200 km radius used for reflectivity mosaics and blue dashed lines indicate 117 km radius used for velocity wave mosaics.

reflectivity since melting and mixed precipitation have higher reflectivities than volumes of only ice or only liquid particles of the same mass. We have developed a technique, called "image muting", which locates regions of mixed or melting precipitation by combining information from the dual polarization product, correlation coefficient. A journal article describing this technique, Tomkins et al. (2022), has been accepted and published in *Atmospheric Measurement Techniques* and is included as Chap. 3. We remove muted regions identified as mixed and melting precipitation from our analysis and reduce the visual prominence of these regions in our visualizations.

2.2.3 Objective detection of local reflectivity enhancements

Identifying and locating regions of locally-enhanced reflectivity can often be subjective and inconsistent from observer to observer. To mitigate this, we developed a technique that objectively identifies local enhancements in radar observations. Previous methods to detect enhancements in enhanced reflectivity features in the rain layers of storms, such as convective precipitation cells, did not work well for detecting snow bands which are more subtle in terms of relative differences compared to the background values and have more diffuse edges. A manuscript documenting the technique in detail is in review at *Atmospheric Measurement Techniques* and is included as Chap. 4. This technique is unique in the sense that it uses two adaptive thresholds to identify objects based on their distinctness (faint or strong) from the background average. This technique is also unique in the sense that we identify objects in a snow rate field that has been rescaled from reflectivity in order to represent the field more linearly in snow. The algorithm outputs a feature detection field which classifies points as "faint feature", "strong feature", or "background" which is used throughout this analysis to quantify the area of locally-enhanced reflectivity in radar observations.

2.2.4 Velocity Wave Mosaics

Velocity waves are calculated using the methods described in Miller et al. (2022) and Hoban (2016) whereby sequential scans of dealiased radial velocity are subtracted to obtain a difference field, which represents a temporal change in the radial velocity field. To discern separation between elements in the difference field, we apply a threshold to the difference field to create a binary wave field.

We calculate the waves on the first 0.5° elevation angle with velocity data available from each volume scan. Before calculating the wave field, we must dealias the velocities. The dealiasing works best with minimal noise and clutter so before dealiasing we remove small speckles in the velocity data and we mask data where the reflectivity is < 0 dBZ or invalid. Scan strategies,

and thus unambiguous ranges, vary between radars and time. We subset all velocity scans to a consistent range of 117 km to reduce the visual artifacts associated with changing scan strategies (see blue dashed circles in Fig. 2.2). 117 km was chosen as it is one of the shortest unambiguous ranges commonly used in this region during the cool season. We unfold the velocities using a region based algorithm developed by Py-ART (Helmus and Collis 2016).

Once we have the subset, trimmed, and dealiased velocity scans, we subtract sequential scans which yields a difference field (Fig. 2.3a–c). We apply a threshold to the difference field to obtain a binary field by setting the wave field to a value of 1 where the difference is <-1 m s^{-1} and a value of zero otherwise (Fig. 2.3d). We chose the value of -1 to not include difference values close to zero where there is a lot of noise.

For velocity waves moving towards a radar, positive values in the difference field (i.e. time 2 velocity > time 1 velocity) indicate acceleration and and negative values in the difference field (i.e. time 2 velocity < time 1 velocity) indicate deceleration. The sign of the difference field values reverses for waves moving away from the radar so that positive values are associated with deceleration. The binary flagged areas in the maps would have horizontal convergence for waves moving towards the radar and horizontal divergence for waves moving away from the radar. Since the interpretation of acceleration and deceleration is dependent on the motion relative to the radar it is challenging to directly map specific regions of convergence and divergence across the entire radar domain. Detection of velocity waves indicates regions of banded acceleration and deceleration in the wind field, and associated bands of convergence and divergence which in turn imply regions of upward and downward motion (Miller et al. 2022, their Figs. 3 and 4). We cannot get information about the velocity waves when the radar beam is perpendicular to the flow (Miller et al. 2022).

Up to this point the fields were kept in their native, polar coordinates, but in order to combine the fields from multiple radars we interpolate to a common grid. Similar to the radar reflectivity mosaics, the common grid is centered on KOKX, however, for the wave fields we interpolate to a 0.5 km Cartesian grid using a nearest neighbor technique, as opposed to Cressman weighting. After interpolating, we remove small speckles less than 16 km^2 (Fig. 2.3e).

To combine wave fields from multiple radars, instead of taking the maximum value where points overlap as we did with the reflectivity mosaics, we take the value from the southernmost radar. There are less regions of overlap between radars compared to the reflectivity mosaics since we subset the wave fields to a smaller range (117 km instead of 200 km; Fig. 2.2). An example of the combined velocity wave field is shown in Fig. 2.4.

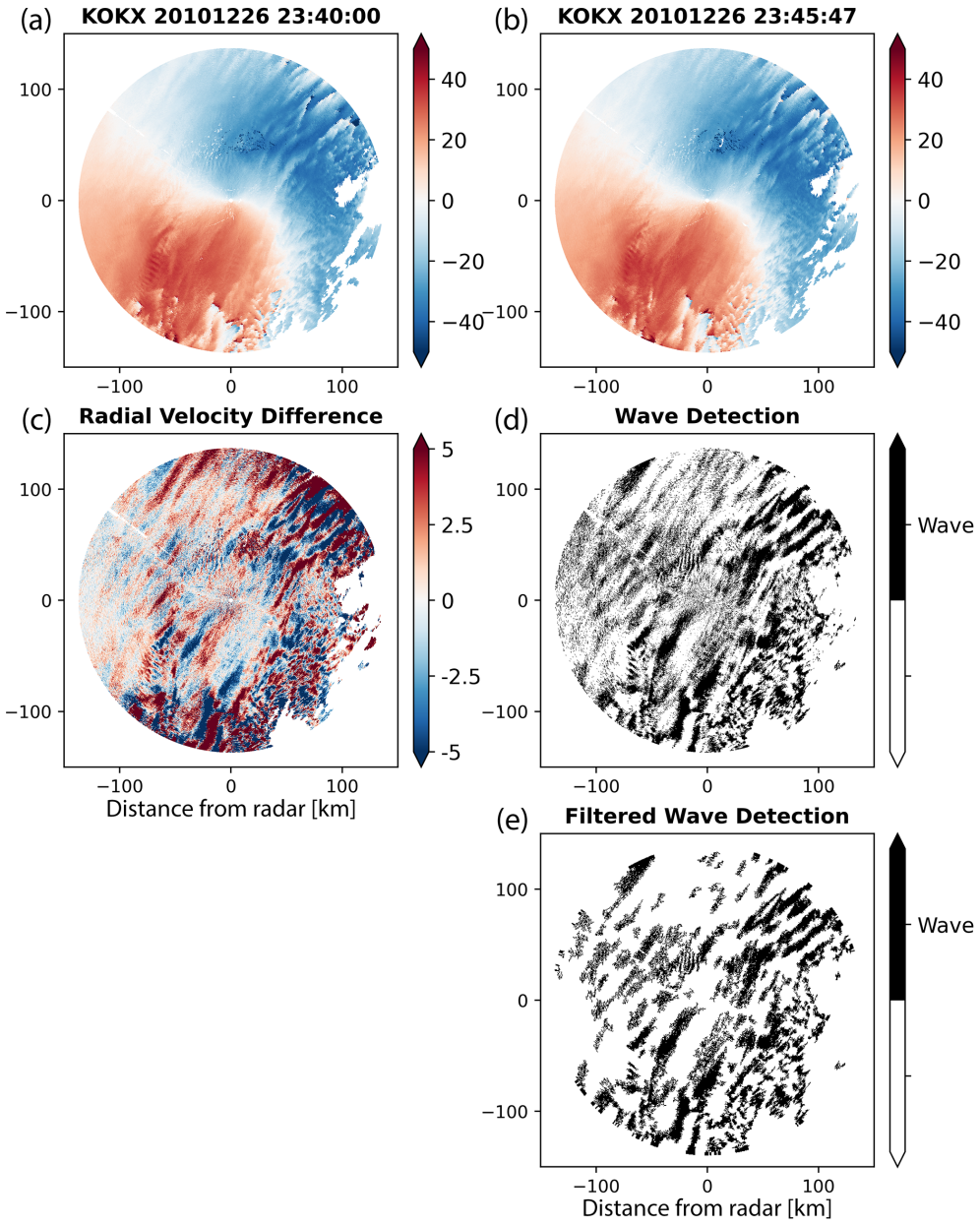

Figure 2.3: Step-by-step wave detection method illustrated using sequential PPI scans of radial velocity from NWS KOKX radar in Upton, NY, on 26 December 2010. Polar coordinate radial velocity fields at 0.5° elevation angle for consecutive scans at (a) 23:40:00 UTC and (b) 23:45:47 UTC. (c) The difference field computed from PPIs (b) minus (a) showing both positive and negative temporal velocity changes. (d) Binary version of the negative portion of the difference field from (c). (e) Cartesian coordinate (0.5 km grid spacing) filtered version of (d) with eight-connected areas < 16 km^2 removed. Figure 2 from Miller et al. (2022).

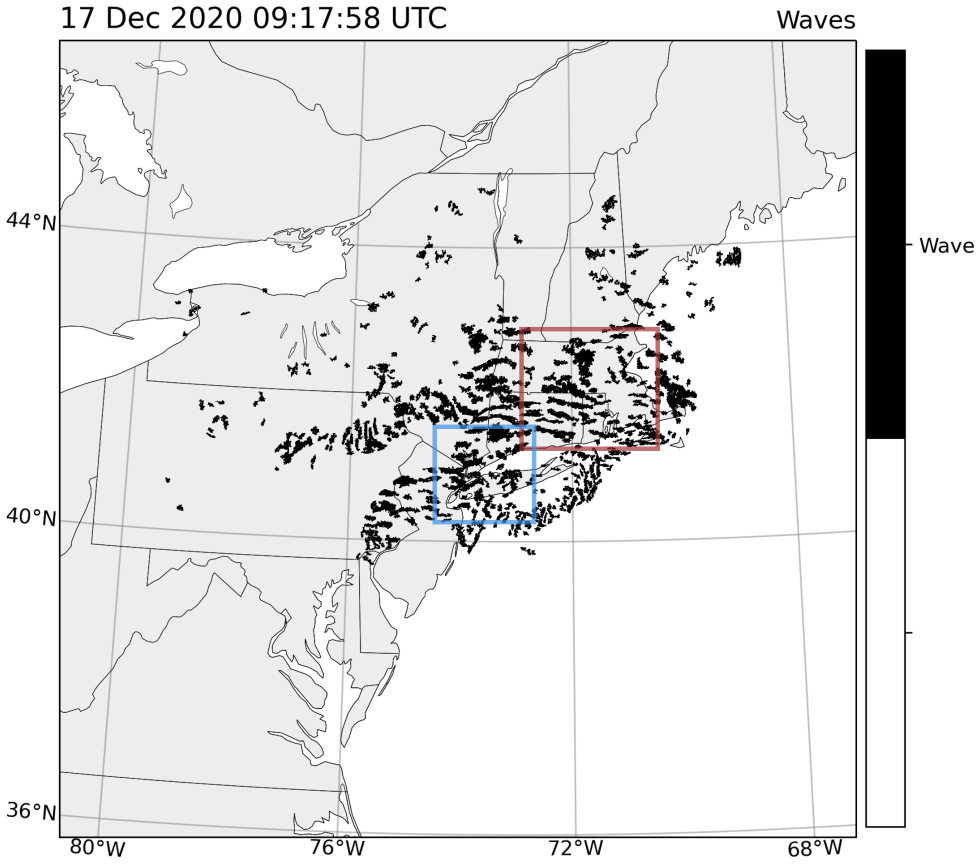

Figure 2.4: An example of the velocity wave mosaic from 27 December 2020 09:17 UTC. Red box indicates Massachusetts region and blue box indicates New York City region for classifying waves (discussed in Sec. 2.2.5).

2.2.5 Classifying velocity wave presence

To understand the relationship between velocity waves and snow rate, we classify wave presence over the hour. Unlike the feature detection field, it is difficult to automate an algorithm to detect waves in the velocity wave field so we do a manual classification. We only consider the presence of waves in two sub-regions of the domain, the first region centered over NYC (blue box in Fig. 2.4) and the second centered over Massachusetts (red box in Fig. 2.4). We chose these two smaller regions as they are both densely-populated regions and they contain a relatively large number of ASOS stations that we can analyze with (6 in the NYC box and 4 in the MA box).

Each region and hour in the 264 day subset was classified by two undergraduate students. The students classified the presence of waves for each hour as "YES", "NO" or "MAYBE". For an hour to be considered a "YES" there must have been waves present throughout the entire region for the entire hour. If waves were present but not necessarily in the entire region or for the entire hour, they were classified as a "MAYBE". Hours were classified as "NO" if there were no waves present in the region for the hour. For the analysis, we combine the "YES" and "MAYBE" categories. One student went back through the classifications and reconciled the times when the two original student's classifications disagreed. The number of hours of each classification for both the NYC and Massachusetts region are presented in Table 2.2. While waves are generally rare for a given *geographic* region, Hoban (2016) found velocity waves in 50% of winter storms so it is worthwhile to understand their impacts on surface snow rates.

Table 2.2: Number of hours each wave classification was observed for each region.

Wave ID	NYC No. Hours	MA No. Hours
YES	60	66
MAYBE	134	112
NO	5986	6002
No data	156	

2.3 Hourly surface station observations

Hourly observations from 29 ASOS stations in the northeast US are used to quantify the liquid equivalent snowfall rates for each winter storm day (Fig. 2.5). The hourly snowfall rates represent hourly liquid equivalent *accumulation* and are not instantaneous snow rates. ASOS

data is obtained through the MADIS database. Measuring snow in rain gauges at ASOS stations can be challenging as snow is easily blown sideways by the wind and doesn't always make it into the gauge (Rasmussen et al. 2012). To ensure we are getting the best measurements, we are only using ASOS stations equipped with all-weather precipitation accumulation gauges (AWPAG) as these gauges are more skilled at measuring liquid equivalent snow accumulation than other types of gauges (Martinaitis et al. 2015). The AWPAG sensors are equipped with Tretyakov or double Alter style shields, which are more accurate at measuring frozen precipitation than gauges with no shields (Rasmussen et al. 2012). AWPAG sensors do not have a heated rim and thus are subject to capping, although it is difficult to estimate how often this occurs in our dataset. If capping does occur, no snow would be reported for an hour. To further ensure that we are using reliable observations, only quality-controlled observations when the wind speed is < 5 m s^{-1} are used in our analysis (Rasmussen et al. 2012). The collection efficiency of frozen precipitation is 1.0 at 0 m s^{-1} and drops to 0.25 at 6 m s^{-1} for double Alter-shielded gauges which is why we chose a threshold of 5 m s^{-1} (Rasmussen et al. 2012). The wind speed threshold removes ∼45% of hourly snow observations, but relatively uniformly over the entire range of precipitation rate observations (Fig. 2.6). That is, the wind speed threshold is not only removing observations with heavy or light precipitation rates. Observations are only used in the analysis if the station has reported snow for at least 4 hours to ensure we are using observations from consistent snow observations, and not any short-lived, low-impact events.

Following the guidelines created by the Society of Automotive Engineers International Ground Deicing Committee and NCAR, we use a liquid equivalent precipitation rate threshold of 2.5 mm hr^{-1} to distinguish heavy snow from light (<1 mm hr^{-1}) and moderate (1-2.5 mm hr^{-1}) snow (Rasmussen et al. 2001). We will only use the term *heavy* to describe the snow rates >2.5 mm hr^{-1}.

We attempted to use visibility reported from the ASOS stations as visibility is commonly used to determine snowfall intensity (Rasmussen et al. 1999), however, the relationship between visibility and precipitation rate was too inconsistent for it to be meaningful. Details can be found in Appendix B.

An example time series of precipitation rate from Boston, MA on 7 February 2021 is shown in Fig. 2.7. Hourly observations that are used in the analysis are represented by a blue bar spanning the hour that the precipitation accumulates. Trace values (0 mm hr^{-1}) are considered in the analysis, but observations where no precipitation fell are not. The example also indicates observations not used in the analysis where the wind speed threshold is exceeded (plus sign in Fig. 2.7).

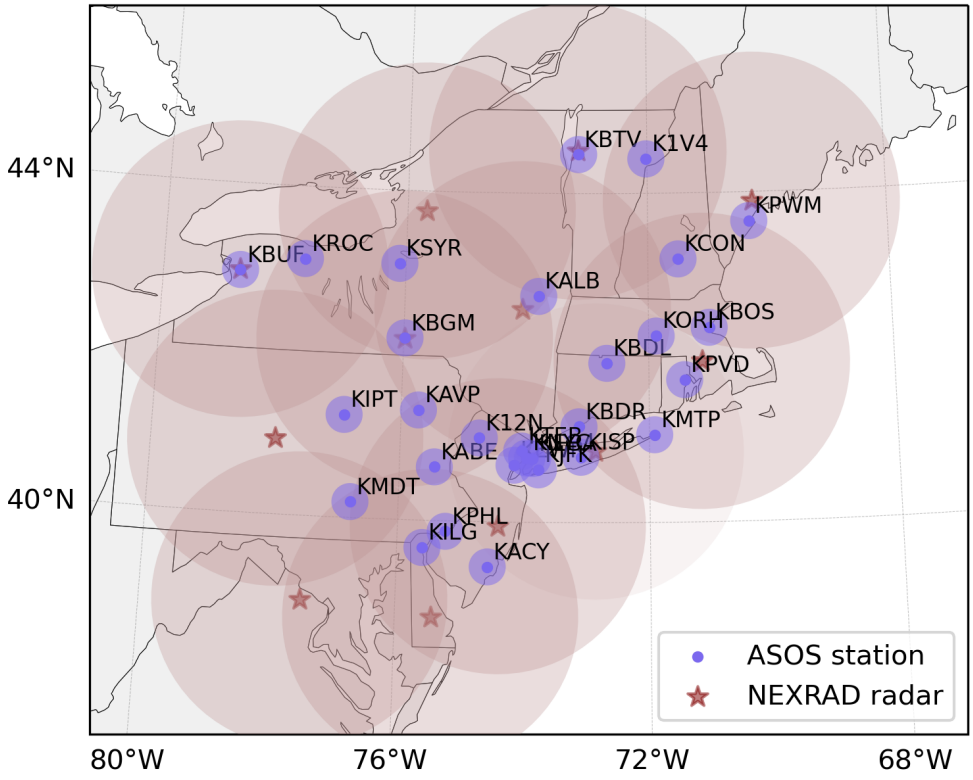

Figure 2.5: Map of ASOS stations (blue dots) used in the analysis. Blue ring surrounding ASOS stations indicates 25 km radius. Red stars and red ring indicate NEXRAD stations and a 200 km radius used to create radar mosaics in Sec. 2.2.

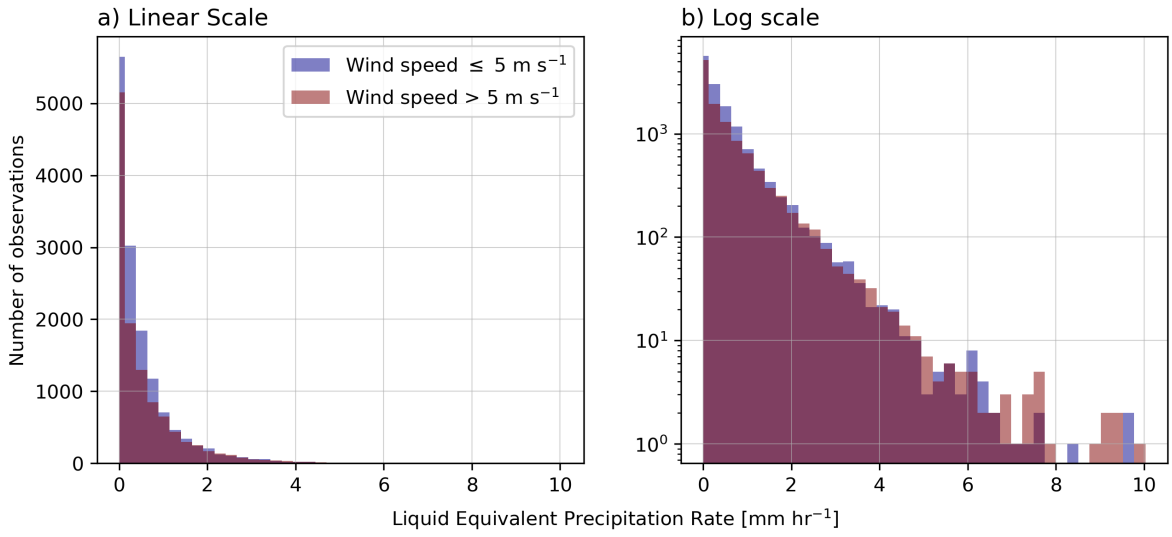

Figure 2.6: Histograms of Liquid Equivalent Precipitation Rate [mm hr^{-1}] for observations ≤ 5 m s^{-1} (blue) > 5 m s^{-1} (red) presented on a (a) linear y-axis scale and (b) log y-axis scale.

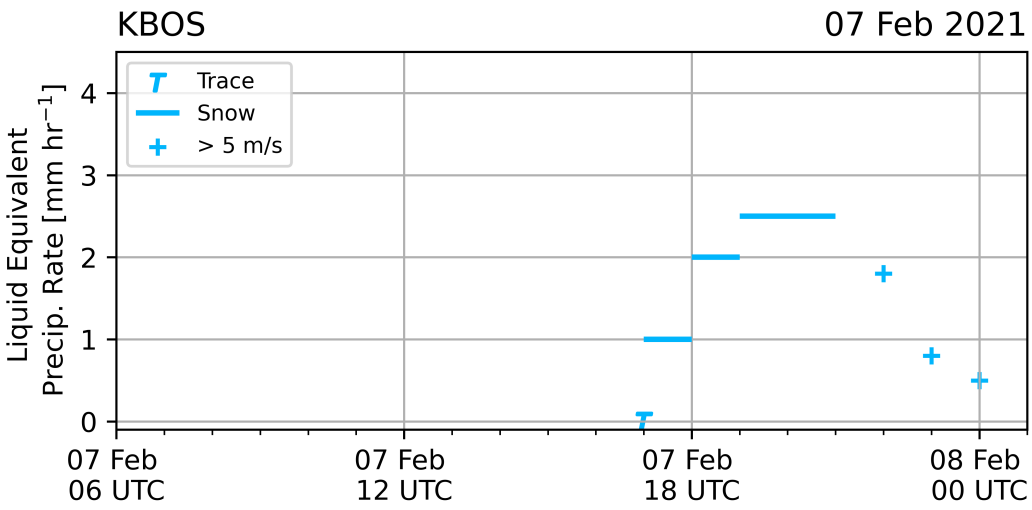

Figure 2.7: Example time series of liquid equivalent precipitation rate [mm hr^{-1}] from the Boston, MA ASOS station (KBOS) from 7 February 2021 06:00 UTC to 8 February 2021 01:00 UTC. Precipitation rates are represented as a bar spanning the hour they were accumulated. Plus signs indicates times when the wind speed is > 5 m s^{-1} and *T* indicates times when trace amounts of precipitation where observed.

2.4 Low pressure center tracks

For each winter storm, we found storm tracks from the ERA5 hourly reanalysis mean sea level pressure (Hersbach et al. 2020) using the methods of Crawford et al. (2021). We subset the global 0.25° resolution ERA5 mean sea level pressure (MSLP) field to the region of Eastern North America (-90 to -60°E, 25 to 55°N). For a given winter storm day, we track over ± 1 day to capture the full evolution of a given low pressure system. To find a single minimum for a given time, we first find all the local minima in the MSLP field using a 200 km search radius. Unlike Crawford et al. (2021), we are using the ERA5 data in native coordinates, so the grid size in km varies slightly between grid boxes. We only consider minima where at least 75% of the data within the footprint are valid to avoid finding minima along the edges of the subset Eastern North America field. Following Crawford et al. (2021), minima found from the MSLP field are only considered if they have a pressure gradient of at least 7.5 hPa/1000 km. We compared the low pressure center minimum to the set of pressures at 200 km range from the low pressure center. To meet the threshold criteria, the mean difference between minimum pressure and the set of pressures at 200 km range must be at least 1.5 hPa. Once all the local minima have been found for the entire period, we then loop through the period again to select a single minimum for each time since there may be no minimum, one minimum, or multiple minima for each time. In the case of multiple minima we choose the minimum that meets most of the following: minimum which is closest geographically to the previous minimum, minimum with

the strongest pressure gradient, and the minimum with the lowest MSLP value. If the closest, strongest, and deepest minima are all different points, we choose the closest minima. If the next point is more than 200 km away from the previous point, we consider this a new system and new track. We filter the tracks to remove tracks that travel less than 250 km or exist for less than 6 hours. Finally, we remove any points on the tracks where the MSLP is greater than 1010 hPa.

Figure 2.8 shows an example of a storm track on 5 December 2020. All tracks between 2012 and 2023 that meet our winter storm criteria defined in Section 2.1 are shown in Fig. 2.9a and the density of all the tracks is shown in Fig. 2.9b. The density of tracks shows a clear tendency for low pressure centers over the ocean moving northeast along the coast (Fig. 2.9b, Bentley et al. 2019). There is a lack of low pressure locations along/to the east of the Appalachian mountains which we suspect is due to our criteria for determining a winter storm. Since we are only looking at events where stations along the coast and slightly inland (Fig. 2.1) in the northeast US produce snow, tracks that come up the Appalachian corridor may not produce enough snow at the surface to be considered in our dataset. Figure 2.9b shows a high density of low pressure tracks off the East coast and a low density of tracks inland along the Appalachian mountains. This pattern is consistent with climatological studies of cyclone tracks (e.g., Bentley et al. 2019). Figure 2.10 from Bentley et al. (2019) shows extratropical cyclone track densities created from National Centers for Environmental Prediction (NCEP) Climate Forecast System Reanalysis (CFSR) which are consistent with our track densities in Fig. 2.9b.

Figure 2.11 shows a time series of the subset of tracks used in the analysis (2012-2023) normalized by the minimum pressure. For a portion of our analysis we further subset the dataset using a 3-hour pressure tendency threshold of -1 hPa hr^{-1} (Fig. 2.11b). The structure and evolution of winter storms is largely governed by the large-scale low pressure system, so information about the location and strength of the system is very useful when analyzing cool-season precipitation systems. We use the low pressure center track to put hourly ASOS observations in a Lagrangian framework. Additionally, we examine the relationship between the hourly ASOS observations and the strength of the low pressure center and distance to the low pressure center.

2.5 Area × Time fraction

A main goal of this project is to understand the impact that locally-enhanced reflectivity features have on the hourly surface snow rates. To accomplish this, we focus on the echo classified as features (from the methods discussed in Sec. 2.2.3) within 25 km of the ASOS station. The regional radar mosaics occur every 5-10 minutes, so in order to distill the echo

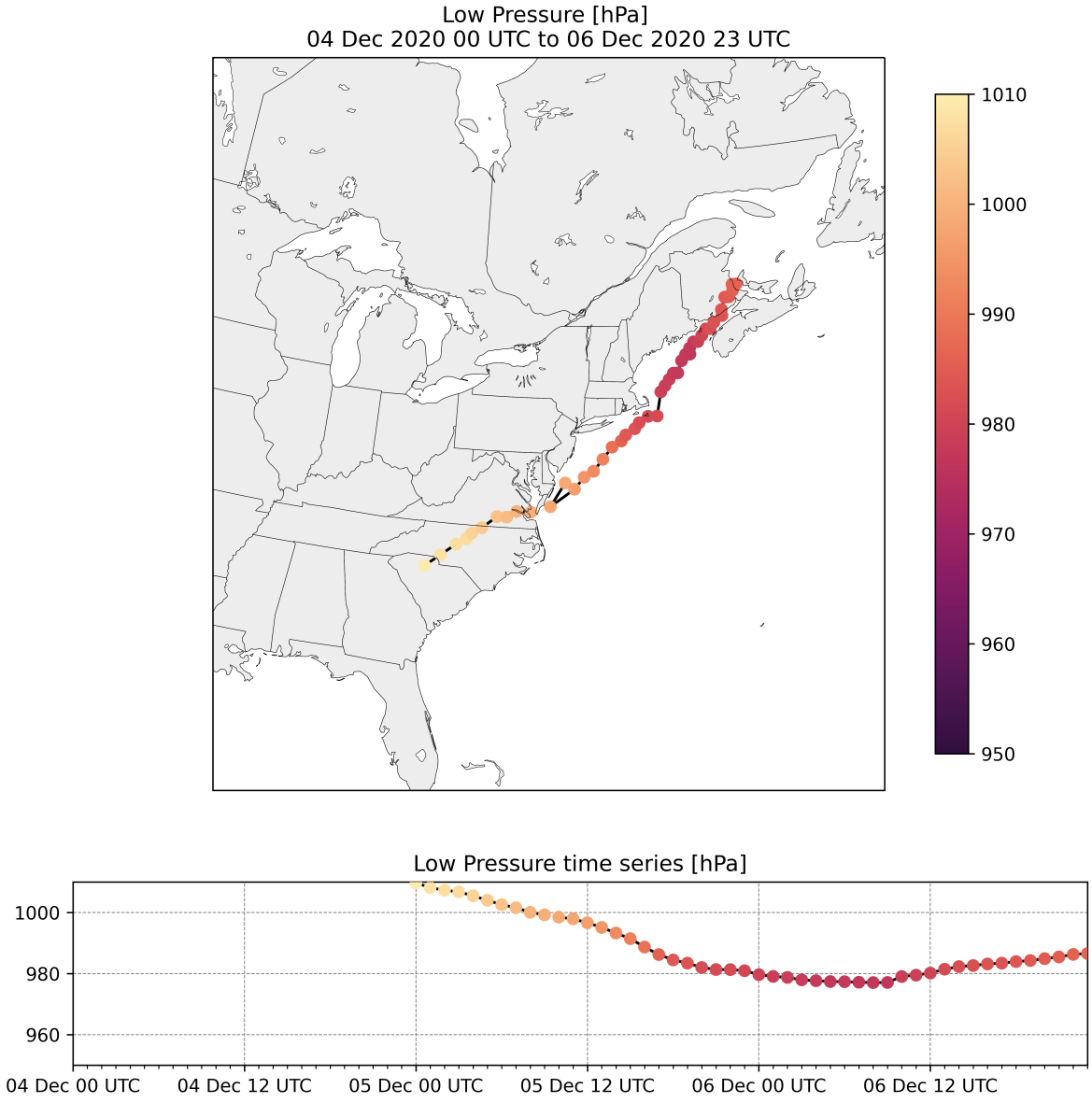

Figure 2.8: An example low pressure track for 5 December 2020. Map of geographic location of low pressure system (top panel) and time series of low pressure system (bottom panel) colored by MSLP value as in legend. Period covers 4 December 2020 00 UTC to 6 December 2020 23 UTC.

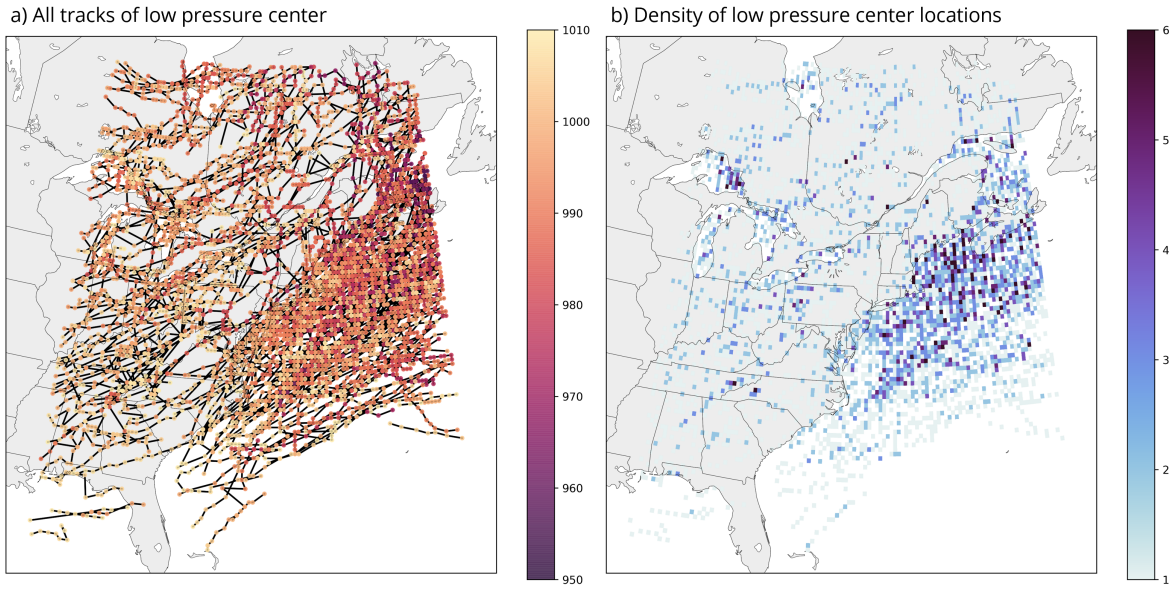

Figure 2.9: Map of (a) all tracks of low pressure centers and (b) density of low pressure center locations for events between 2012-2023.

area over the hour, we created an integrated metric called the area × time fraction. Figure 2.12 visualizes the echo area data that goes into calculating the area × time fraction. Most of the analysis uses the area × time fraction calculated for the echo classified as features (both strong and faint; yellow and orange echo in Fig. 2.12) surrounding a station, but a small part of the analysis uses the background area × time fraction which is calculated only using the echo classified as background (teal echo in Fig. 2.12).

To calculate the area × time fraction we sum the area surrounding the station within 25 km for that hour and then we divide by the total seconds in an hour and the total area surrounding the station within 25 km which leaves us with a unitless fraction. Fig. 2.13 demonstrates 3 scenarios (of many) that would yield an area × time fraction of 0.5. An area × time fraction of 1 would indicate the entire surrounding region is filled with feature echo for the entire hour and a fraction of 0 would indicate no feature echo in the surrounding region for the entire hour.

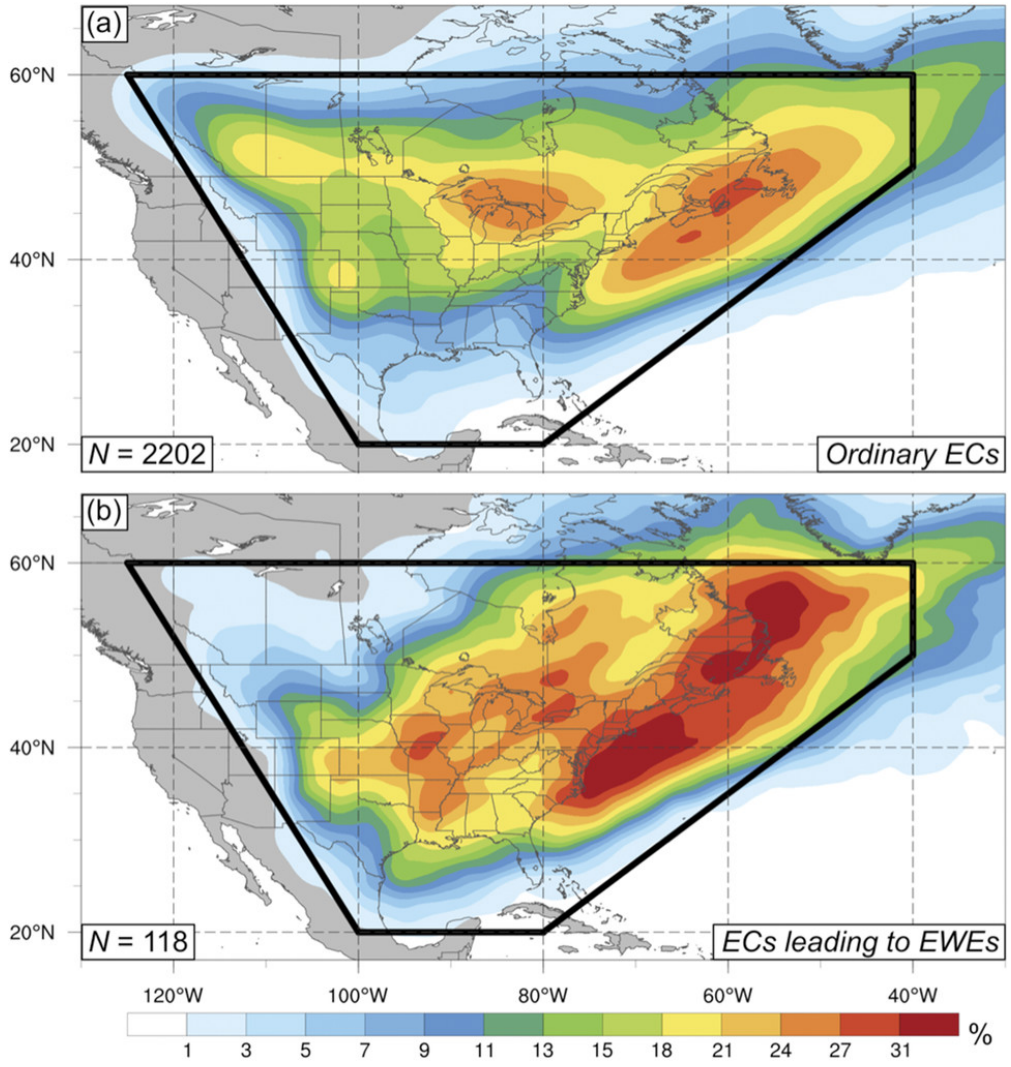

Figure 2.10: Track density of (a) ordinary extratropical cyclones and (b) extratropical cyclones leading to extreme weather events during October-March 1979-2016. Figure 8 from Bentley et al. (2019).

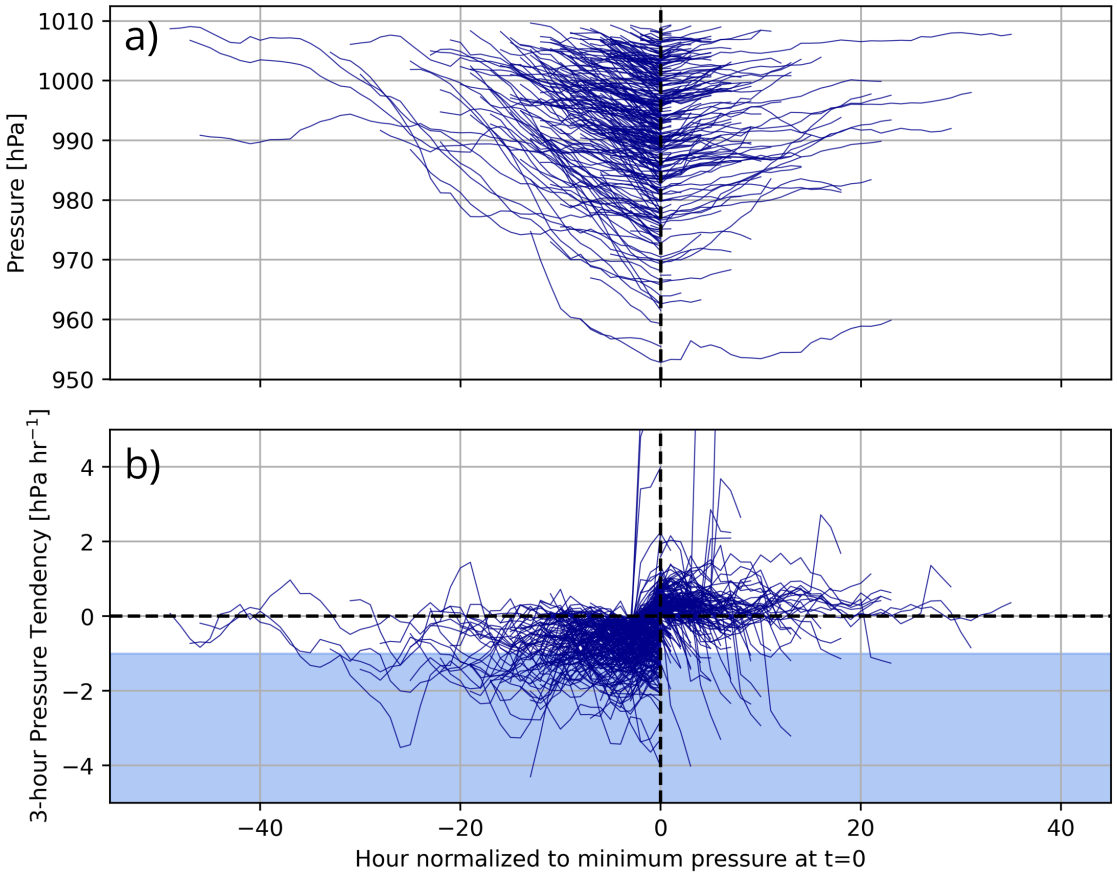

Figure 2.11: Time series of all low center pressure tracks between 2012-2023 normalized by the minimum pressure at time t=0. (a) low center pressure [hPa] and (b) 3-hour pressure tendency [hPa hr^{-1}] of low pressure centers. Blue colored panel in (b) indicates where the pressure tendency is ≤ 1 hPa hr^{-1}.

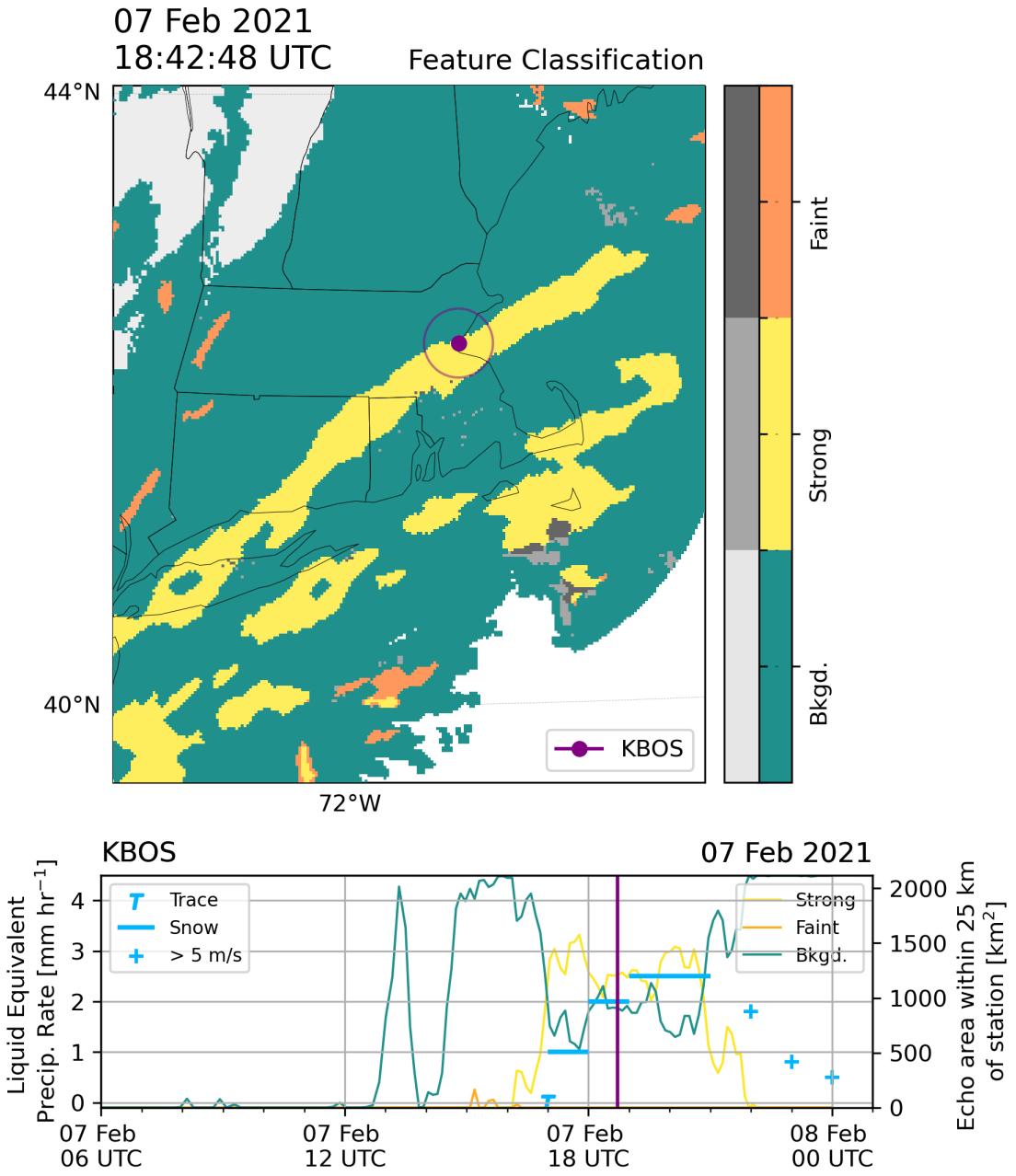

Figure 2.12: Top panel shows the feature detection field zoomed in on Massachusetts for 7 February 2021 18:42 UTC. The bottom panel shows an example time series of ASOS hourly precipitation rate valid from 7 February 2021 06 UTC to 08 February 2021 01 UTC (same as Fig. 2.7) and echo areas calculated within 25 km of Boston, MA ASOS station (KBOS; purple dot on map). Colored lines in time series correspond to background area (teal), strong area (yellow) and faint area (orange) within 25 km of the KBOS station (purple ring on top panel). Purple vertical line annotated on time series indicates the time of the map in the top panel.

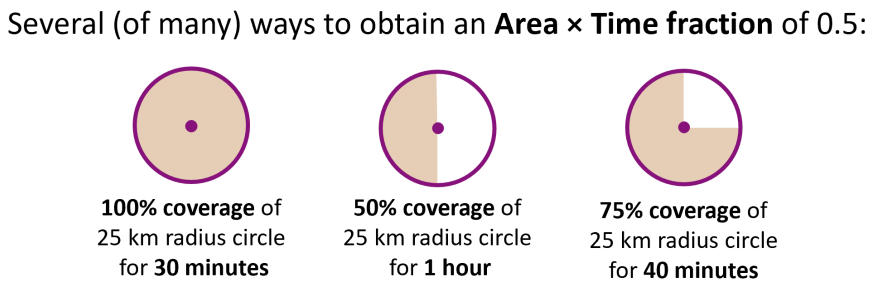

Figure 2.13: Several examples of echo patterns over a given time that would yield an area × time fraction of 0.5.

Chapter 3

Image Muting of Mixed Precipitation to Improve Identification of Regions of Heavy Snow in Radar Data

Published in Atmospheric Measurement Techniques in September 2022.

Citation Tomkins, L. M., S. E. Yuter, M. A. Miller, L. R. Allen, 2022: Image Muting of Mixed Precipitation to Improve Identification of Regions of Heavy Snow in Radar Data. *Atmospheric Measurement Techniques*, **15**, 5515-5525, https://doi.org/10.5194/amt-15-5515-2022

Authors Laura M. Tomkins[1], Sandra E. Yuter[1,2], Matthew A. Miller[2], and Luke R. Allen[1]

[1]Center for Geospatial Analytics, North Carolina State University, Raleigh, NC, 27695, USA

[2]Department of Marine, Earth and Atmospheric Science, North Carolina State University, Raleigh, NC, 27695, USA

Acknowledgements The authors express their appreciation to V. Chandrasekar (Colorado State University) and Scott Ellis (NCAR) for their insights into radar data quality issues. Special thanks also to McKenzie Peters, Anya Apontes-Torres, and Jordan Fritz for their assistance in data processing, to Kevin Burris and Rachel Kennedy for providing feedback on the manuscript, and to Christina Cartwright for editing the manuscript. This work was supported by the National Science Foundation (AGS-1347491 and AGS-1905736) and the National Aeronautics and Space Administration (80NSSC19K0354) and the Center for Geospatial Analytics at North Carolina State University.

Abstract In winter storms, enhanced radar reflectivity is often associated with heavy snow. However, some higher reflectivities are the result of mixed precipitation including melting snow. The correlation coefficient (a dual-polarization radar variable) can identify regions of and mixed precipitation, but this information is usually presented separately from reflectivity. Especially under time pressure, radar data users can mistake regions of mixed precipitation for heavy snow because of the high cognitive load associated with comparing data in two fields while simultaneously attempting to discount a portion of the high reflectivity values. We developed an image muting method for regional radar maps that visually deemphasizes the high reflectivity values associated with mixed precipitation. These image muted depictions of winter storm precipitation structures are useful for analyzing regions of heavy snow and monitoring real-time weather conditions.

3.1 Introduction

Weather radar data from ground-based scanning radars are crucial for monitoring the location, intensity, and evolution of storms. Winter storms in mid-latitude regions often contain subregions with rain, mixed precipitation, and snow that move and evolve over the storm lifetime (Schultz et al. 2019). Higher radar reflectivity values are generally associated with heavier precipitation. But the transition among rain, partially melted snow, and snow precipitation types creates a challenge when interpreting radar reflectivity because volumes with melting precipitation have higher reflectivities than volumes with the equivalent precipitation mass of only ice hydrometeors or only liquid hydrometeors (Vivekanandan et al. 1994; Straka et al. 2000; Rauber and Nesbitt 2018).

In particular, the changes in phase from ice to partially melted ice and then to rain modify the dielectric constant of the particles so that volumes with the same precipitation mass per unit volume can have different reflectivity values (Battan 1973). When analyzing banded snow features in winter storms, areas of mixed precipitation can be distracting and misleading (e.g. Picca et al. 2014). We define mixed precipitation as precipitation that includes combinations of rain or freezing rain, snow, sleet, and partially-melted snow.

Regions of mixtures of precipitation types can be identified with the dual-polarization radar variable known as the correlation coefficient (ρ_{HV}) (Table 3.1; e.g. Vivekanandan et al. 1994; Straka et al. 2000; Kumjian 2013a). Correlation coefficient is a statistical measure of how consistent the shapes and sizes of particles are within a radar resolution volume (Rauber and Nesbitt 2018). This variable is insensitive to radar calibration and yields comparable values for the same set of hydrometeors across radar networks with identical hardware and signal processing methods. Correlation coefficient is approximately one in regions with single

hydrometeor types (i.e. only rain or only snow) and decreases in regions where there is an increasing diversity of hydrometeor orientations and shapes (i.e. mixed precipitation such as rain with snow and/or partially melted ice) (Giangrande et al. 2008; Rauber and Nesbitt 2018). Additionally, correlation coefficient can have low values in various types of ground clutter and is used in identifying non-meteorological echo (e.g. Zrnić et al. 2006; Alku et al. 2015; Kumjian 2013b).

Table 3.1: Correlation coefficient values associated with physical mechanisms that increase radar reflectivities when Z > 20 dBZ and other conditions are held constant.

Description	**Increase number of ice particles in snow**	**Increase size of ice particles in snow**	**Mixtures of partially-melted ice, ice, and rain**
Change to water substance mass per unit volume	Increases	Increases	No change
ρ_{HV} value	~ 1	~ 1	< 0.97

With increasing range from a radar, radar resolution volume size increases and signal to noise ratio (SNR) decreases. For example near the melting layer, larger radar resolution volumes are more likely to have non-uniform beam filling than smaller radar resolution volumes. In theory, non-uniform beam filling would tend to decrease correlation coefficient (Ryzhkov 2007). Unlike radars that transmit at horizontal and vertical polarizations, the NEXRAD radar transmits at a single polarization oriented at 45 degrees. The current method used to compute correlation coefficient in US NEXRAD operational radars yields increased values with decreasing SNR (Ivić 2019). In practice, the impact of SNR tends to be much more prevalent than non-uniform beam filling. This suggests that the SNR effect masks most of the effects of non-uniform beam filling in NEXRAD correlation coefficient data quality.

Since reflectivity, correlation coefficient, and hydrometeor types are usually presented as separate products (NOAA 2017), someone wanting to discern regions of heavy snow versus mixed precipitation in a winter storm needs to toggle back and forth among different products or overlay them. Neural science studies show that switching between sources of information increases the cognitive load of a task (Sweller et al. 2011; Harrower 2007). Keeping track of changing shapes of moving objects is particularly challenging (Suchow and Alvarez 2011). Integrating related material and removing irrelevant material is essential for maximizing understanding and learning (Mayer and Moreno 2003; Sweller et al. 2011; Harrower 2007).

In order to reduce the cognitive load associated with analyzing precipitation structures in reflectivity, we propose a new visualization technique we refer to as "image muting". Image muting aids interpretation of sequences of radar data in movie loops. We plot the reflectivities

using a perceptually uniform, color-blind-friendly color scale and the subset of reflectivity values corresponding to mixed precipitation using a gray scale of matching perceptual lightness. This visualization does not remove areas of melting but rather "mutes" them, making the regions stand out less than the snow-only or rain-only portions of the storm. Work by Calvo et al. (2021) demonstrates how making small changes in climate visualizations can reduce the cognitive load and support analysis and potential decision making.

Our image muting technique is described in detail in Sect. 3.2, and applications of our technique are presented in Sect. 3.4.

3.2 Methods

To demonstrate the methodology, we used Level-II data from several National Weather Service (NWS) Next-Generation Radar (NEXRAD) network radars in the northeast United States (US) that were obtained from the NOAA Archive on Amazon Web Services (Ansari et al. 2018). Complete volume scans are available from each radar approximately every 5 to 10 minutes. This technique can be applied to any radar data set that has both reflectivity and correlation coefficient fields.

3.2.1 Regional Mapping

We combine data from several radars to create regional radar maps utilizing functions in the open source Python Atmospheric Radiation Measurement (ARM) Radar Toolkit developed by the Department of Energy ARM Climate Research Facility (Py-ART; Helmus and Collis 2016). We first extract the first 0.5° elevation angle plan-position indicator (PPI) from each volume scan. We do not interpolate to a constant altitude in order to preserve as much fine-scale detail in the reflectivity and correlation coefficient structures as possible. We include only data within 200 km range from a radar as this is sufficient for combining data from multiple radars in much of the continental US without substantial gaps and constrains the beam center to be below 4 km altitude above radar level. The polar coordinate data from each individual radar are interpolated using Cressman weighting (Cressman 1959) to a Cartesian grid covering our geographic region of interest. Before interpolating, we convert the reflectivity from units of dBZ to units of $mm^6\ m^{-3}$ because interpolating in linear reflectivity units provides a more accurate representation of the polar data (Warren and Protat 2019). We interpolate each polar radar object used in the regional map to the same Cartesian grid with 2 km grid spacing. For the northeast US regional maps shown in this paper, the regional grid is 1201 km x 1201 km. We convert the reflectivity back to dBZ after the interpolation step. Finally, to combine data from

all the radars into a single object, we designate a "central radar" to stitch all the other radars to. For storms in the northeast US, we use the Long Island, NY (KOKX) radar as the central radar. For each volume scan at KOKX, we find the closest time from the other radars (within 8 minutes). For grid points where coverage from adjacent radars overlaps, we use data from the radar with the maximum reflectivity value and its corresponding correlation coefficient value. Use of the maximum reflectivity value means adjacent points can be from 0.5° elevation angles from different radars yielding discontinuities in altitude of up to 4 km. Since our main research application is identifying snow bands and lighter versus heavier regions of snow, having adjacent points not continuous in altitude was an acceptable trade off. Before plotting the fields, we despeckle the data to remove areas of echo that are less than 20 km^2.

3.2.2 Identification of mixed precipitation

In effect, we are implementing a hydrometeor identification for only mixed precipitation. We simplify the radar data visualization by choosing this one hydrometeor category to *deemphasize* in the reflectivity field. We identify grid points where the hydrometeors are partially melted and/or mixed rain and snow, where the ρ_{HV} is below a threshold of 0.97, and where the reflectivity values is greater than or equal to 20 dBZ. We used 0.97 following Giangrande et al. (2008) who found that the correlation coefficient for dry snow exceeded this value. Adding the criterion of reflectivity $\geq$ 20 dBZ was essential in distinguishing regions of melting or mixed precipitation that could be confused with heavy snow from regions of light precipitation with noisy, unreliable ρ_{HV} values. The 0.97 ρ_{HV} and 20 dBZ thresholds are consistent with Griffin et al. (2020) who used ρ_{HV} to detect melting layers in radar data. We note that not all clutter points are removed in our regional maps which can have low values of ρ_{HV} and may show up as stationary features in animations of image muted maps.

The inputs and outputs for image muting from a coastal winter precipitation event on 07 February 2020 are shown in Fig. 3.1. Information from regional maps of the radar reflectivity field (Fig. 3.1a) and the correlation coefficient field (Fig. 3.1b) are combined. We show an intermediate stage (Fig. 3.1c) illustrating the pragmatic importance of the using both the correlation coefficient and reflectivity criteria. ρ_{HV} values $\leq$ 0.97 often occur toward the edges of the individual radar echo domains where the beam is $> \sim 3$ km altitude and in winter storms very likely to be only snow (green region in Fig. 3.1c). We infer that the reflectivity $<$ 20 dBZ is too low to reliably indicate mixed precipitation that can be mistaken for heavy snow. The areas in gray represent regions where the $\rho_{HV} \leq 0.97$ and the reflectivity is $\geq$ 20 dBZ, where melting is likely to be present and where we mute the reflectivity. Dark blue colors in Fig. 3.1c are where the correlation coefficient is $>$ 0.97, indicative of uniform precipitation types. The final image

muted reflectivity product (Fig. 3.1d) uses a gray scale to deemphasize the subset of reflectivity values where it is likely to be mixed precipitation. This example shows two linear features in central New York that could be misinterpreted as snowbands when analyzing the reflectivity alone (green ovals in 3.1a). The animation of this figure (Video Supplement Animation-Figure-3.1) for the time period 12:00:00 to 15:00:00 UTC shows how the mixed precipitation region covers portions of the high reflectivity bands in Fig. 3.1a as the bands move eastward. The image muted reflectivity helps users focus on regions of the storm that are not affected by mixed precipitation. We experimented with trying to distinguish the rain-only from the snow-only regions but found that there was insufficient information in the dual-polarization radar variables to do this reliably without data on air temperature. Air mass and frontal boundaries can cause freezing level heights to vary sharply within winter storms unlike warm-season precipitation.

3.3 Evaluation with independent data

Vertical cross-sections from airborne radar data provide an opportunity to evaluate the identification of melting regions in ground-based scanning radar data in fine detail. Figure 3.2 shows an image muted regional map corresponding to a science flight during the NASA Investigation of Microphysics and Precipitation for Atlantic Coast-Threatening Snowstorms (IMPACTS) 2020 field project (McMurdie et al. 2022). Reflectivity from the nadir-pointing ER-2 X-band Doppler Radar (EXRAD; Heymsfield et al. 1996) along the flight track (green line) in Fig. 3.2a is shown in Fig. 3.2b. The gray region in the image muted regional map indicates a quasi-linear region of mixed precipitation extending though eastern New York up to Vermont and New Hampshire (Fig. 3.2a) between areas of primarily snow (to the northwest in upstate New York) and primarily rain (to the southeast over southern New England). Eastward of 175 km along the flight transect in Fig. 3.2b, there is a clear melting layer signature in the NASA EXRAD data starting near the surface and rising to about 2 km above surface level (ASL) (represented by the enhanced region of higher reflectivity). The melting layer can also be observed with other variables from the same transect presented in Fig. 3.3. In particular, the linear depolarization ratio from the ER-2 cloud radar shows the structure of the melting layer very well (Fig. 3.3d). Under the melting layer, the values of downward pointing Doppler velocity > -4 m s^{-1} indicate the rain layer. The position of the transition between snow and rain in the vertical cross-section is consistent with the edge of the gray area in Fig. 3.2a. An animated version of this figure shows the timing as the ER-2 aircraft transects through the image muted portion of the regional map (Video Supplement Animation-Figure-3.2). As the airplane reaches around 175 km in the transect, one can see that the height of the NEXRAD radar beam used to create the regional

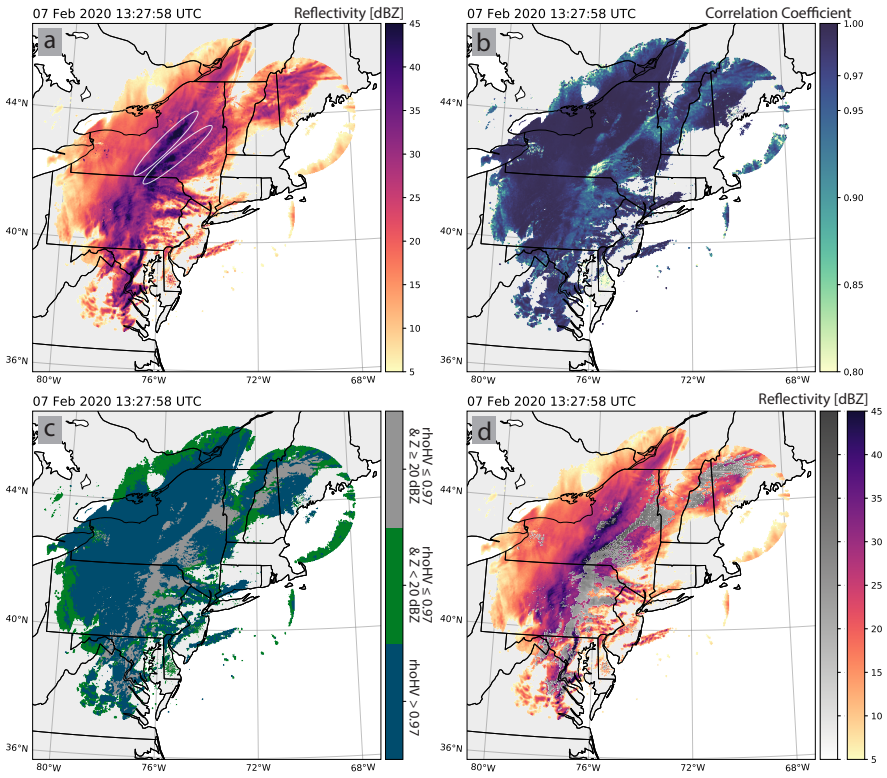

Figure 3.1: Image muting processing components for a radar regional map from 07 February 2020 at 13:27:58 UTC. (a) Radar reflectivity (dBZ) field. (b) Correlation coefficient field. (c) Categories indicating regions that meet the following conditions: correlation coefficient > 0.97 (dark blue), correlation coefficient ≤ 0.97 and reflectivity < 20 dBZ (green), and correlation coefficient ≤ 0.97 and reflectivity ≥ 20 dBZ (gray). (d) Final image muted product combining color scale for reflectivities in snow and rain regions with gray scale to mute reflectivities in mixed precipitation regions. Green ovals in (a) indicate banded features discussed in text. An animated version of this figure is in Video Supplement Animation-Figure-3.1.

map (black X in Fig. 3.2b) begins to intersect the melting layer.

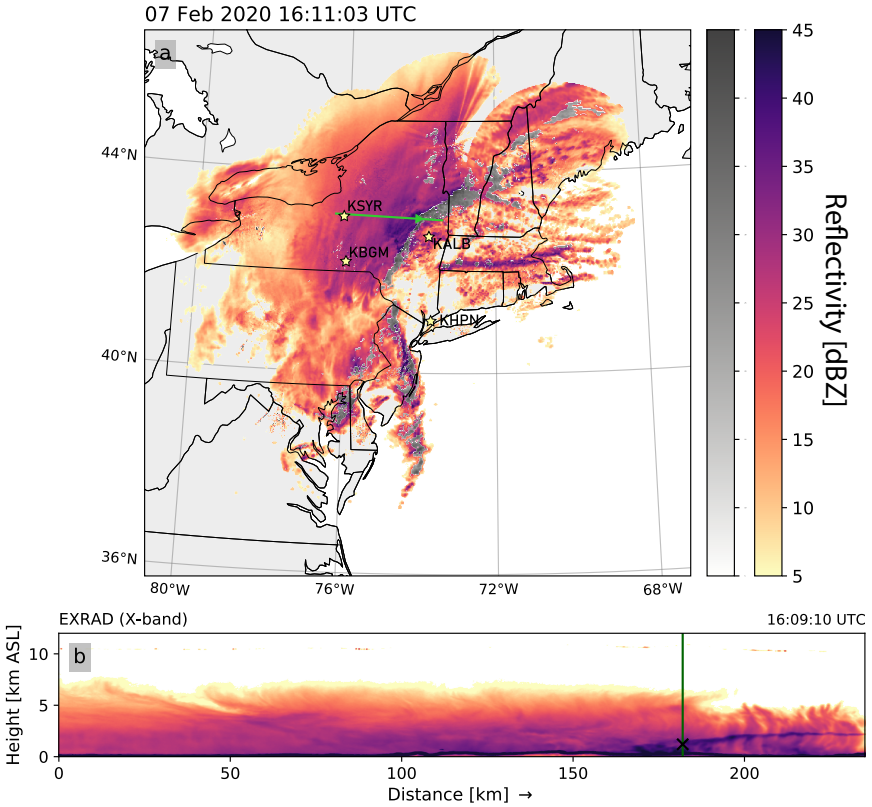

Figure 3.2: Comparison of image muted regional map with detailed vertical cross-section from NASA ER-2 X-band Doppler radar during a NASA IMPACTS science mission on 07 February 2020. At 16:09:10 UTC, the aircraft is located at the transition between snow and melting precipitation in the radar regional map. (a) Image muted reflectivity valid at 16:11:03 UTC with the ER-2 flight leg (green line), aircraft location corresponding to time shown in bottom panel is at the arrow head along the leg. Locations of ASOS observations in Fig. 3.4 are annotated with stars and black labels. (b) Vertical cross-section of reflectivity from NASA EXRAD radar with current aircraft location near the top of the vertical green line. Time at right corresponds to aircraft position. The black X indicates the height of the point in panel a that varies along the 0.5° elevation angle scans used to construct the regional maps. An animated version of this figure is in Video Supplement Animation-Figure-3.2.

Information to further evaluate the timing and location of the melting and mixed precipitation is available from time series of precipitation from surface sensors. Figure 3.4 shows hourly time series of precipitation types at several NWS Automated Surface Observing Systems (ASOS) weather stations (letters in Fig. 3.2a). The surface observations and timing of precipitation transitions align well with the evolution and movement of the storm (Fig. 3.2 and 3.3). For

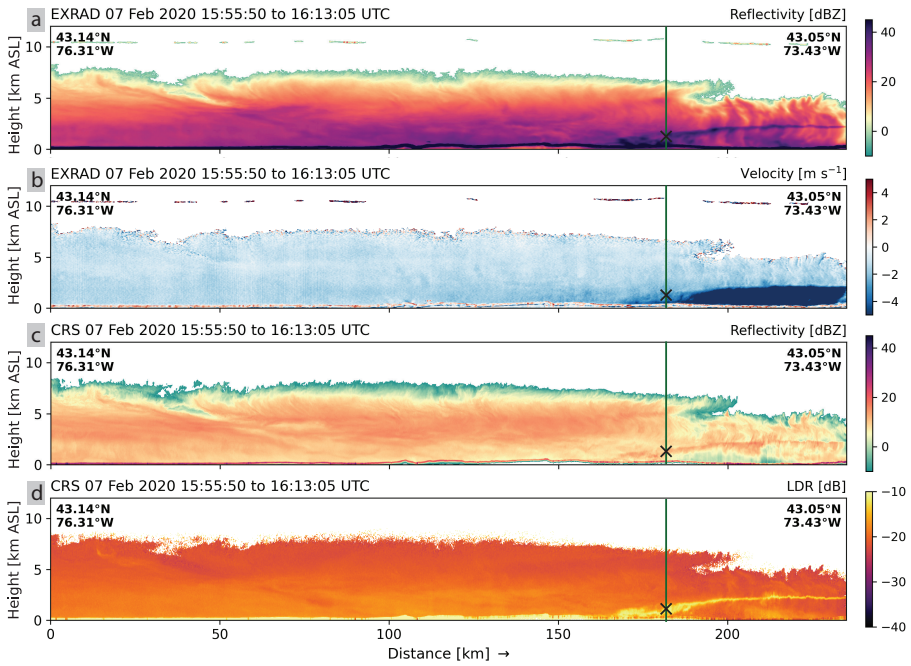

Figure 3.3: Vertical cross-sections of (a) reflectivity and (b) vertical velocity from NASA ER-2 EXRAD radar and (c) reflectivity and (d) linear depolarization ratio (LDR) from NASA ER-2 CRS radar coincident with vertical cross section in 3.2. Green line indicates current aircraft location and black X indicates the height of the point in 3.2a that varies along the 0.5° elevation angle scans used to construct the regional maps.

the hour of 16:00:00 UTC, Syracuse Hancock International Airport (KSYR) is reporting snow, Albany International Airport (KALB) is reporting rain, Greater Binghamton, NY (KBGM) is reporting snow, and Westchester County Airport (KHPN) is reporting rain. The ASOS time series for KBGM also indicates the hour when rain transitioned to mixed (11:00:00 UTC) and mixed transitioned to snow (15:00:00 UTC) (Fig. 3.4c). These surface data are consistent with the locations of the muted precipitation (Video Supplement Animation-Figure-3.2).

3.4 Application to RHIs

Information on the 3D geometry of melting regions can be obtained by applying the image muting technique to range-height indicator (RHI) scans constructed from a full volume scan from ground-based scanning radars. These examples illustrate the often complex layering within coastal winter storms where portions of the warmer air masses (> 0° C) slide over colder air masses (< 0° C). Figure 3.5 is from the KOKX radar during a winter storm on 08 February 2013. The green line in the PPIs corresponds to the azimuth used to create the RHIs (Fig. 3.5a,b). Rather than a simple flat or tilted melting layer, this storm had a 3D "arc-like" mixed precipitation structure (Fig. 3.5c,d). The temperature field along the RHI from the ERA5 reanalysis data shows the associated vertical temperature structure and the 0°C isotherm (Fig. 3.5e; Hersbach et al. 2020). Below 2 km ASL, the temperature is mostly above freezing, which corresponds well to the top of the melting in the RHI panels (Fig. 3.5c,d,e). There appears to be an intrusion of colder air around 0.5 km ASL (0–30 km horizontal) that is likely contributing to the arc-like feature seen in the RHI panels (Fig. 3.5c,d,e). Animations of panels a through d of Fig. 3.5 show the complex horizontal pattern as the features evolve and move (Video Supplement Animation-Figure-3.5). The structure of the melting layer in this example is also discussed in Griffin et al. (2014).

An example from the Philadelphia, PA (KDIX) radar during a winter storm on 01 December 2019 is presented in Fig. 3.6. This storm exhibited an interesting "collapsing" signature in the correlation coefficient and image muted reflectivity PPI fields in northern New Jersey (Fig. 3.6a,b). The RHI panels intersect the feature and show a sharp drop in melting layer altitude around the 80 km range from the radar (Fig. 3.6c,d). The temperature field from the ERA5 reanalysis shows an elongated layer of above freezing temperatures around 2 km ASL and another area of above freezing temperatures below 1 km ASL between 0 and 50 km away from the radar (Fig. 3.6e). It is likely that the ERA5 data are too coarse to fully represent the complex temperature structure as suggested by the radar RHIs. Animations of panels a through d of Fig. 3.6 show the initiation of this feature and how it evolves (Video Supplement Animation-Figure-3.6).

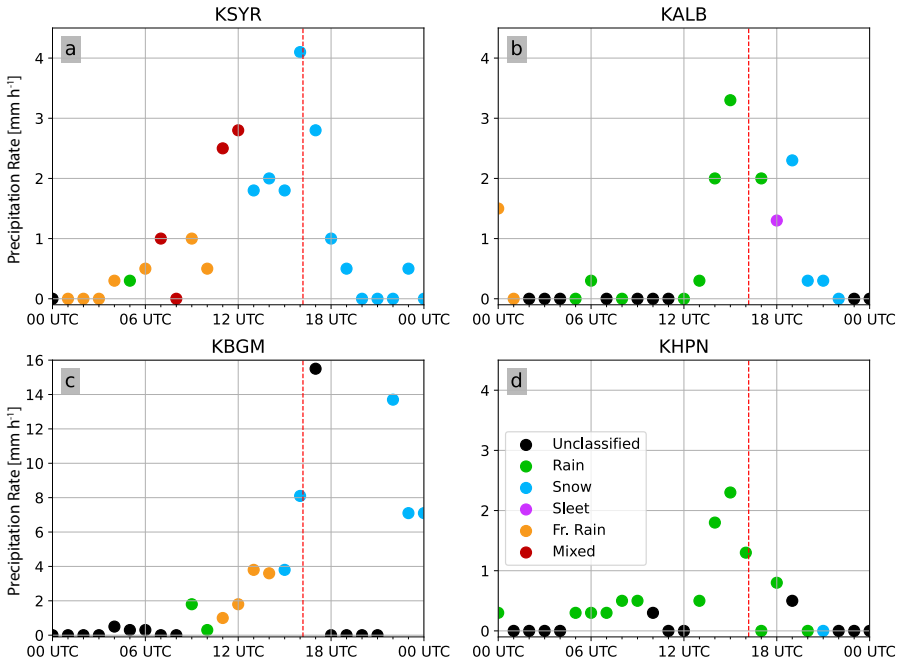

Figure 3.4: Hourly ASOS precipitation rate and type [mm h^{-1}] reports for 07 February 2020 from (a) KSYR, (b) KALB, (c) KBGM and (d) KHPN. Colors indicate precipitation type as in legend in panel d. Red dashed line indicates 16:09:11 UTC, highlighted in Fig. 3.2. The y-axis range is larger in panel c compared to other panels.

3.5 Summary

The proliferation of weather radar web interfaces and mobile apps has made operational radar data easily accessible to a wide range of users with varying levels of radar data interpretation expertise. People who are well versed in the subtle nuances of interpreting weather radar data represent only a subset of research meteorologists and an even smaller subset of the broader set of radar data users which includes emergency managers, TV weathercasters, and airport operators.

Users of weather radar data associate areas of higher reflectivities with heavier precipitation. In winter storms, linear features of localized enhanced reflectivity are associated with heavy snow bands and contribute to snow accumulation forecast uncertainties (e.g. Novak et al. 2008; Ganetis et al. 2018). But regions of mixed precipitation can exhibit higher reflectivities often without the higher precipitation rates or equivalent liquid water content. For winter storm analysis, it is important to distinguish between locally enhanced reflectivity associated with increases in ice mass and reflectivity from melting. Fortunately, mixed precipitation often has a low correlation coefficient (< 0.97) which in combination with reflectivities ≥ 20 dBZ can be used to distinguish higher reflectivity regions that are and are not heavy snow (Giangrande

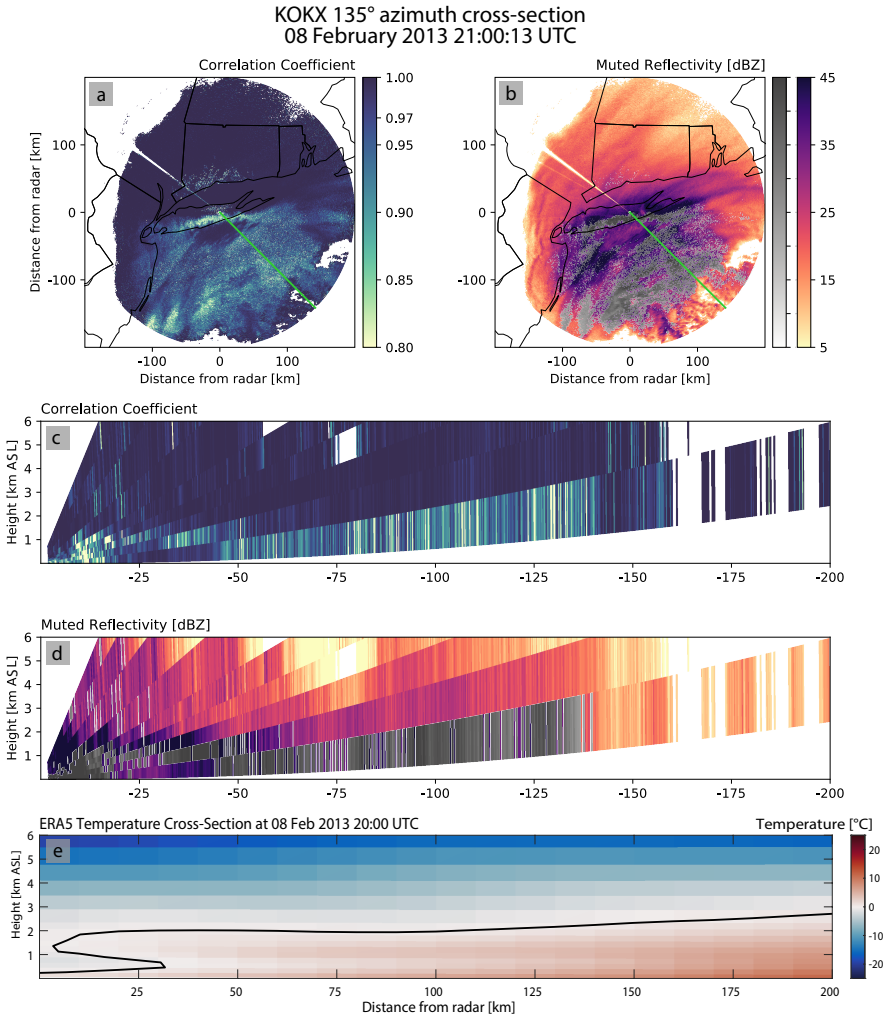

Figure 3.5: Comparison of image muted regional map with reconstructed RHIs and reanalysis temperature vertical cross-section from KOKX radar on 08 February 2013. (a) Correlation coefficient and (b) image muted reflectivity (dBZ) 0.5° elevation angle PPI plots for KOKX radar valid 08 February 2013 21:00:13 UTC. Green line in (a) and (b) indicates location of reconstructed RHI cross-sections from (c) correlation coefficient and (d) image muted reflectivity. (e) ERA5 reanalysis temperature cross-section interpolated to the plane of the RHI. Black line in panel e indicates 0°C isotherm. An animated version of this figure is in Video Supplement Animation-Figure-3.5.

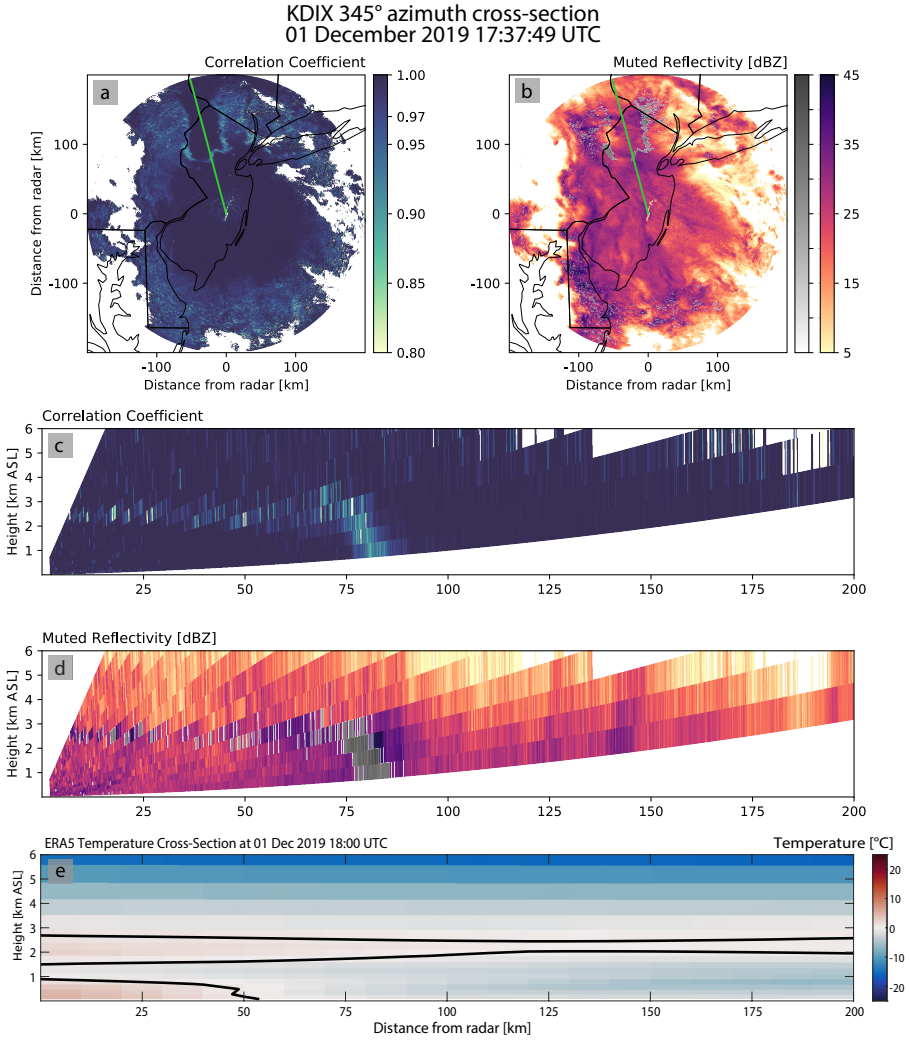

Figure 3.6: Comparison of image muted regional map with reconstructed RHIs and reanalysis temperature vertical cross-section from KDIX radar on 01 December 2019. (a) Correlation coefficient and (b) image muted reflectivity (dBZ) 0.5° elevation angle PPI plots for KDIX radar valid 01 December 2019 17:37:49 UTC. Green line in (a) and (b) indicates location of reconstructed RHI cross-sections from (c) correlation coefficient and (d) image muted reflectivity. (e) ERA5 reanalysis temperature cross-section interpolated to the plane of the RHI. Black line in panel e indicates 0°C isotherm. An animated version of this figure is in Video Supplement Animation-Figure-3.6.

et al. 2008).

Typically, radar reflectivity and hydrometeor identification are presented as separate products (Rauber and Nesbitt 2018; Bringi and Chandrasekar 2001; NOAA 2017). When these products are separate, a user examining an evolving winter storm needs to simultaneously examine synced sequences of maps and mentally keep track of the moving positions of higher reflectivity features relative to the hydrometeor type signatures.

We developed image muting, which reduces the visual prominence of the reflectivities within the mixed precipitation features in winter storms that can be mis-identified as heavy snow. Reflectivities corresponding to the mixed precipitation features are deemphasized using a gray scale and the regions with just snow and just rain are depicted in a corresponding full-color scale. We tuned the thresholds used for identification of mixed precipitation areas using a combination of detailed vertical cross-sections from research aircraft radar, reconstructed RHIs from ground-based scanning radars, and surface weather stations observed precipitation types. Users could apply this visualization technique using operational hydrometeor classification as an input and mute other specific regions depending on the application.

Image muted maps and movie loops will help reduce the error associated with misinterpreting radar reflectivity products during winter storms. Users examining an image muted map movie loop can easily distinguish the locations of heavy snow and mixed precipitation as compared to having to consult separate map movie loops. Monitoring where transitions from rain to mixed precipitation and mixed precipitation to snow are present and where they are likely to move to can aid in assessing expected impacts of winter weather.

The image muting visualization technique can be applied to a wide variety of applications. Any data display that suffers from potential misinterpretation could benefit from image muting portions of the data to de-emphasize subregions in the plot.

Video Supplement All animations can be viewed at: `https://av.tib.eu/series/1228`. Individual animations can be viewed by following the DOI URL.

Animation-Figure-3.1: Animated plot of image muting processing components for a radar regional map from 12:00:00 to 15:00:00 UTC on 07 February 2020. (a) Radar reflectivity (dBZ) field. (b) Correlation coefficient field. (c) Categories indicating regions that meet the following conditions: correlation coefficient > 0.97 (dark blue), correlation coefficient ≤ 0.97 and reflectivity < 20 dBZ (green), and correlation coefficient ≤ 0.97 and reflectivity ≥ 20 dBZ (gray). (d) Final image muted product combining color scale for reflectivities in snow and rain regions with gray scale to mute reflectivities in mixed precipitation regions. (goes with Fig. 3.1). Title: 07 February 2020 image muting example DOI: `https://doi.org/10.5446/57311`

Animation-Figure-3.2: Animated plot of image muted regional map with detailed vertical

cross-section from NASA ER-2 X-band Doppler radar during a NASA IMPACTS science mission on 07 February 2020. At 16:09:10 UTC, the aircraft is located at the transition between snow and melting precipitation in the radar regional map. (a) Image muted reflectivity valid at 16:11:03 UTC with the ER-2 flight leg (green line), aircraft location corresponding to time shown in bottom panel is at the arrow head along the leg. Locations of ASOS observations in Fig. 3.4 are annotated with stars and black labels. (b) Vertical cross-section of reflectivity from NASA EXRAD radar with current aircraft location near the top of the vertical green line. Time at right corresponds to aircraft position. The black X indicates the height of the point in panel a that varies along the 0.5° elevation angle scans used to construct the regional maps. (goes with Fig. 3.2). Title: 07 February 2020 NASA IMPACTS transect comparison DOI: `https://doi.org/10.5446/57312`

Animation-Figure-3.5: Animated plot of image muted regional map with reconstructed RHIs and reanalysis temperature vertical cross-section from KOKX radar on 08 February 2013. (a) Correlation coefficient and (b) image muted reflectivity (dBZ) 0.5° elevation angle PPI plots for KOKX radar valid valid 21:00:00 UTC 08 February to 00:00:00 UTC 09 February 2013. Green line in (a) and (b) indicates location of reconstructed RHI cross-sections from (c) correlation coefficient and (d) image muted reflectivity. (e) ERA5 reanalysis temperature cross-section interpolated to the plane of the RHI. Black line in panel e indicates 0°C isotherm. (goes with Fig. 3.5). Title: 08 February 2013 KOKX RHI comparison DOI: `https://doi.org/10.5446/57313`

Animation-Figure-3.6: Animated plot of image muted regional map with reconstructed RHIs and reanalysis temperature vertical cross-section from KDIX radar on 01 December 2019. (a) Correlation coefficient and (b) image muted reflectivity (dBZ) 0.5° elevation angle PPI plots for KDIX radar valid 15:00:00 to 20:00:00 UTC on 01 December 2019. Green line in (a) and (b) indicates location of reconstructed RHI cross-sections from (c) correlation coefficient and (d) image muted reflectivity. (e) ERA5 reanalysis temperature cross-section interpolated to the plane of the RHI. Black line in panel e indicates 0°C isotherm. (goes with Fig. 3.6). Title: 01 December 2019 KDIX RHI comparison DOI: `https://doi.org/10.5446/57314`

Chapter 4

Dual adaptive differential threshold method for automated detection of faint and strong echo features in radar observations of winter storms

Submitted to Atmospheric Measurement Techniques in December 2023.

Citation Tomkins, L. M., S. E. Yuter, M. A. Miller, 2023: Dual adaptive differential threshold method for automated detection of faint and strong echo features in radar observations of winter storms. *In review.*

Authors Laura M. Tomkins[1], Sandra E. Yuter[1,2], and Matthew A. Miller[2]

[1]Center for Geospatial Analytics, North Carolina State University, Raleigh, NC, 27695, USA

[2]Department of Marine, Earth and Atmospheric Science, North Carolina State University, Raleigh, NC, 27695, USA

Acknowledgements Our testing methodology and iterative algorithm refinement benefited from discussions with Brian Colle, Phillip Yeh, Luke Allen, and Kevin Burris. This research has been supported by the National Science Foundation (AGS-1905736), the National Aeronautics and Space Administration (80NSSC19K0354), and the Center for Geospatial Analytics at North Carolina State University.

Abstract Radar observations of winter storms often exhibit locally-enhanced linear features in reflectivity, sometimes labeled as snow bands. We have developed a new, objective method for detecting locally-enhanced echo features in radar data from winter storms. In comparison

to convective cells in warm season precipitation, these features are usually less distinct from the background echo and often have more fuzzy or feathered edges. This technique identifies both prominent, strong features and more subtle, faint features. A key difference from previous radar reflectivity feature detection algorithms is the combined use of two adaptive differential thresholds, one that decreases with increasing background values and one that increases with increasing background values. The algorithm detects features within a snow rate field that is rescaled from reflectivity and incorporates an under and over estimate to account for uncertainties in the detection. We demonstrate the technique on several examples from the US National Weather Service operational radar network. The feature detection algorithm is highly customizable and can be tuned for a variety of datasets and applications.

4.1 Introduction

Linear features of enhanced reflectivity, labeled as snow bands, are often observed in winter storms and are an active topic of research (Baxter and Schumacher 2017; Ganetis et al. 2018; Lackmann and Thompson 2019; Kenyon et al. 2020; Picca et al. 2014; Novak et al. 2004; McMurdie et al. 2022; Colle et al. 2023). Snow bands that are $\geq$ 250 km in length are described as primary or single bands and sets of roughly parallel smaller bands each less than 250 km long are described as multi-bands (Ganetis et al. 2018). Primary bands are typically associated with frontogenesis (Novak et al. 2004), but the forcing mechanism for multi-bands is still unclear (Ganetis et al. 2018). Unlike convective cells in rain which usually have a sharp reflectivity gradient between the cell itself and the background reflectivity, snow bands stand out less from the background and the edges of snow bands can gradually feather out. Hence, objective methods to identify convective and stratiform precipitation in radar data of deep convection do not work well for winter storms.

Much of the previous work to detect snow bands in radar reflectivity data focused on identification of primary bands and either ignored multi-bands or only addressed the stronger subset of multi-bands. Novak et al. (2004) and Baxter and Schumacher (2017) used dBZ thresholds (30 and 25 dBZ, respectively) to identify primary band objects in National Weather Service (NWS) Next Generation Radar (NEXRAD) Level-III reflectivity regional maps. Kenyon et al. (2020) identified primary snow bands for five winter seasons using Level-III reflectivity data. Kenyon et al. (2020) used a 20 dBZ threshold, with the caveat that there must be an embedded region > 25 dBZ along at least half the axis that is at least 10 dB greater than the background reflectivity. Level-III reflectivity data has a precision of 5-dB and will inherently not be able to identify features that are < 5 dB different from the background. In general, methods that use fixed thresholds are sensitive to the radar calibration as well as to the grid spacing of the input

data since reflectivity values are not scale invariant (Rinehart 2004).

Several authors have used methods that adapt to changing background reflectivity values in the wider storm and hence better detect localized enhancements than fixed threshold methods. Ganetis et al. (2018) identified both primary and multi-band features by identifying echo regions in NEXRAD Level-II regional reflectivity maps that were greater than the upper-sextile of reflectivity values for a given precipitation region. Ganetis et al. (2018) classified primary bands as objects that were $\geq$ 200 km and had an aspect ratio (width/length) of $\leq$ 0.5 and multi-bands as objects that were $<$ 200 km and had as aspect ratio $\leq$ 0.5. Objects that had an aspect ratio $>$ 0.5 and a length $\geq$ 10 and $\leq$ 100 km were labelled as cells. Radford et al. (2019) used NEXRAD base reflectivity mosaics for three winter seasons and only considered objects that were 1.25 standard deviations above the mean reflectivity, as well as $\geq$ 250 km in length and with a minimum aspect ratio of 0.33 following the methods of Baxter and Schumacher (2017).

The Method for Object-Based Diagnostic Evaluation (MODE), included in the Model Evaluation Tools (MET) verification software package, is a popular tool for detecting objects in meteorological datasets (Bullock et al. 2016). Originally developed to compare forecast fields to observed fields, MODE applies a convolution to a field and then uses user-defined thresholds to find objects in the original field. For example, the user can change the size of the convolution radius used to smooth the input field and the single threshold that determines whether an object is defined relative to the smoothed background.

For some applications, detecting only the stronger subset of objects is sufficient. For our research, which aims to understand the environments in which snow bands form and the physical processes that create them, a fuller picture of their life cycle is needed. Visual inspection of sequences of radar data demonstrates that advecting snow bands often undergo transitions from faint to strong to faint before dissipating. In order to study these structures, we needed a automated snow band detection method that would detect a range of echo features from faint to strong.

Our method, described in detail in Section 4.2, rescales the reflectivity field to an estimated snow rate to better discern weak echo features and combines two differential adaptive thresholds to determine if a feature stands out from the background. We use the generic term *locally enhanced feature* to describe objects that one would pick out by eye as distinct from lower background values. We define two varieties of locally enhanced features, those that are have smaller differences from the background, *faint* features, and those that have larger differences, *strong* features. The algorithm we developed for detecting locally-enhanced features in winter storms is described in Section 4.2, examples of our technique are shown in Section 4.3, and a summary is provided in Section 4.4. We contributed the software to the open-source python package, Py-ART (Helmus and Collis 2016) where it is available for general use.Within this

paper, we will be using the terms *object* which is commonly used in the image processing literature, and *feature* which refers here to the meteorological application interchangeably. We also define winter season storms of interest as those that contain a substantial area of surface snow fall.

4.2 Methods

4.2.1 Data

To demonstrate our method, we use NEXRAD Level-II radar reflectivity regional reflectivity maps composed from several radars in the Northeast US (Tomkins et al. 2022, 2023a,b). The regional maps use 2D Cartesian Cressman interpolation to a 2 km grid based on the 0.5° elevation angle from several different radars. Where there is overlap between adjacent radars, we use the point with the highest reflectivity value. Given the coarse vertical spatial resolution of NWS operational radar volume coverage patterns, 3D Cartesian interpolation often smooths and obscures the fine-scale horizontal features we need to discern faint objects. For our application, the varying altitudes along the 0.5° elevation angle scans that constitute the regional maps are preferable to a constant altitude map that smooths key features we need for our analysis. While we demonstrate our technique with a specific set of NEXRAD radars in the northeast US, the technique can be applied to any gridded radar data.

4.2.2 Feature detection algorithm

The feature detection method described in this paper to identify locally enhanced reflectivity features in cool-season precipitation systems is built upon the implementation of adaptive thresholds for objective convective-stratiform precipitation classification developed for warm-season storms in a series of papers by Churchill and Houze (1984), Steiner et al. (1995), Yuter and Houze (1997), and Yuter et al. (2005). The underlying idea, identifying the cores of features that exceed the background value by an amount that varies with the background value, is well established (Steiner et al. 1995). These types of algorithms are highly customizable and can be tuned to a wide variety of datasets. So as to be more general purpose, the software we contributed to the open-source python package, Py-ART, can be configured to run either as a variant of established convective-stratiform precipitation algorithm for warm-season storms or for the application described in this paper for winter storms.

A data flow diagram of the winter storm algorithm using the Yourdon symbol conventions (Woodman 1988) shows the key steps in the data processing (Fig. 4.1). The top-level data flow

(Fig. 4.1a) is shown with two levels of nested data processing (Fig. 4.1b and c). The steps in Fig. 4.1c follow the data flow steps from Steiner et al. (1995) algorithm to identify convective and stratiform precipitation from reflectivity in rain layers. Input parameter names and recommended settings for detecting locally enhanced reflectivity features in snow are provided in Table 4.1.

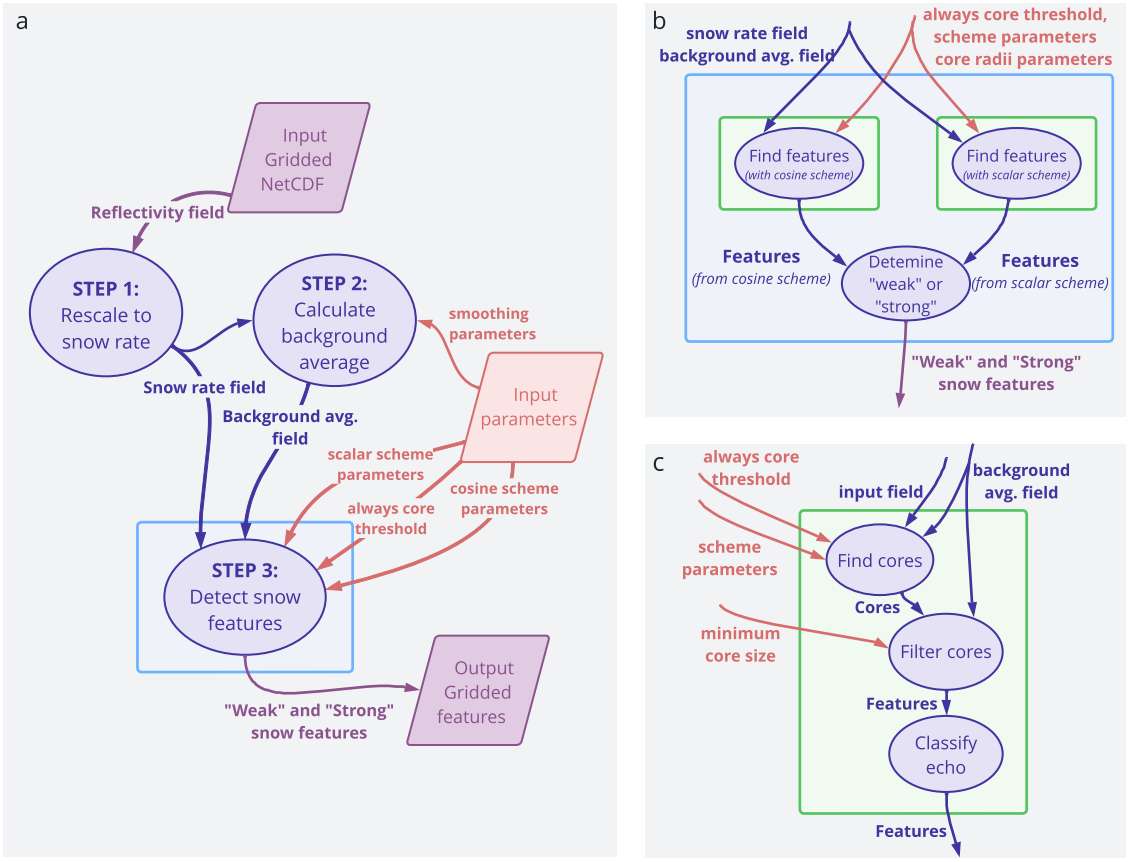

Figure 4.1: Data flow diagram of the winter storm feature detection algorithm. Dark blue ovals indicate processes, purple polygons indicate input and output data, and orange elements indicate adjustable setting parameters used in the functions. Each arrow represents an input or output to the associated functions. The reflectivity field and background average field are 2D arrays. The strong and faint snow features are represented by distinct values in a 2D array. a) Top level data flows. b) The detailed steps within "Step 3: Detect snow features" (blue) box in panel a). c) shows the detailed steps within the "Find features" (green) boxes in panel b).

The feature detection algorithm outputs 2D arrays that in effect simplify the input reflectivity field into faint feature, strong feature, and background categories. Additional image processing

Table 4.1: Parameters used to detect locally enhanced echo features in winter storms. All input parameters to the algorithm as run for this paper are provided including those that are in effect turned off.

Parameter		**Value**
	Always core threshold	5 mm hr^{-1}
	Min. core size	10 km^2
Smoothing parameters	Background radius	40 km
	Min. fraction for footprint	0.75
Cosine scheme parameters	Max. difference (i.e. a in Eqn. 4.1)	1.5 mm hr^{-1}
	Zero difference cosine value (i.e. b in Eqn. 4.1)	5 mm hr^{-1}
Scalar scheme parameters	Scalar difference (i.e. c in Eqn. 4.2)	1.5
Core radii parameters	Max. core radius	2 km
(turned off)	Value for max. core radius	10 mm hr^{-1}
Background echo classification parameters	Min. value used	0 mm hr^{-1}
(turned off)	Weak echo threshold	0 mm hr^{-1}

of this output based on the shape characteristics of individual features such as aspect ratio, length, width, and area can be used to further classify the features into different types of banded and cellular features (e.g. Ganetis et al. 2018; Yeh 2024).

Estimation of snow rate

A key difference from previous methods described in Section 4.1, is the use of an estimated snow rate field as the input for the feature detection instead of a radar reflectivity field. In snow, radar reflectivity dBZ is roughly proportional to $log_{10}(\text{mass}^3)$, where mass is the mass per unit volume of precipitation-sized ice. Any one relationship between reflectivity and snow rate has high uncertainty as observational studies have shown that for given dBZ, the associated snow rate can vary by two orders of magnitude (Fujiyoshi et al. 1990). This first step in the data processing rescales reflectivity to a value that is more linear in liquid equivalent snow rate. We do not use the derived snow rates for quantitative estimates of precipitation, just as an alternative scaling factor to reflectivity in dB.

Empirical Z-S relations encompass ones for dry snow, which have smaller changes of equivalent liquid per ΔZ to ones for wet snow which have larger changes per ΔZ (Fig. 4.2 Rasmussen et al. 2003). In order to obtain higher contrast between locally enhanced Z in terms of snow rates, we use the wet snow Z-S relationship from Rasmussen et al. (2003); $Z_e = 57.3S^{1.67}$ where Z_e is equivalent radar reflectivity with units of mm^6 m^{-3} and S is snow rate with units of mm hr^{-1}. Our results are not sensitive to the absolute values of snow rate, only to the relative anomaly from the background average. Examples of re-scaling the reflectivity field to a snow rate field are shown in Fig. 4.3.

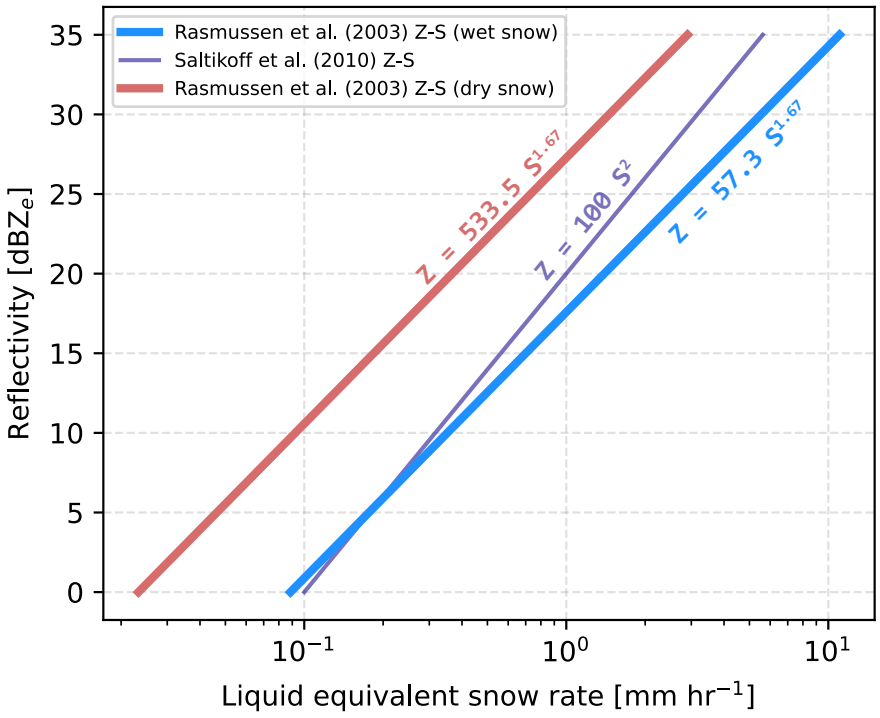

Figure 4.2: Reflectivity to snow rate (Z-S) relationships with log-scale x-axis. The bold blue line indicates the relationship from Rasmussen et al. (2003) for wet snow used in this study. The bold red line shows the relationship for dry snow from Rasmussen et al. (2003) and the purple line shows the relationship from Saltikoff et al. (2010).

Calculation of smoothed background field

A locally smoothed background average snow rate field is computed from the snow rate field (Fig. 4.3). The background radius smoothing parameter is used to define a circular footprint surrounding each pixel (Fig. 4.1a). We found that use of circular footprints produced fewer artifacts than rectangular footprints. The surrounding points are then averaged to find the background value for that point. Feature detection is sensitive to the size of the area used to calculate the background value (not shown). We found a background radius of 40 km was the most suitable for detecting snow band features in the NWS NEXRAD data. A larger background radius will yield a smoother background average field used to compare to the input field to find features. A smaller background radius is likely more suitable for warm-season precipitation systems which usually have stronger reflectivity gradients than cool-season precipitation systems. An example of the locally-smoothed background average snow rate field is shown in Fig. 4.3.

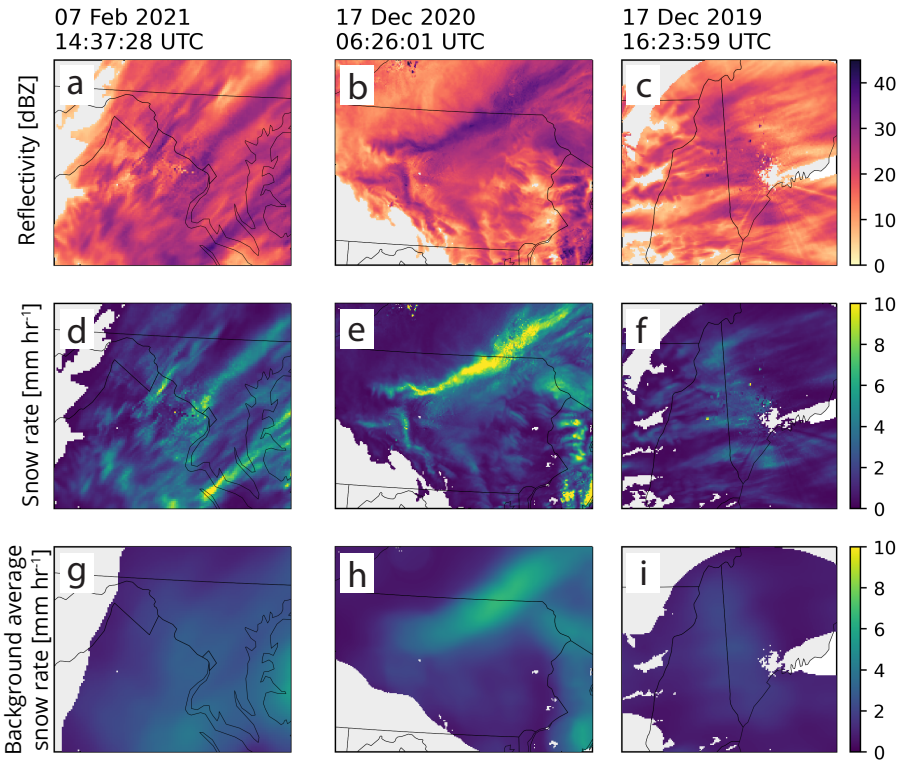

Figure 4.3: Close-up examples of (a)-(c) Reflectivity [dBZ] rescaled to (d)-(f) snow rate [mm hr^{-1}] and smoothing of the snow rate fields to a (g)-(i) background average using a 40 km radius footprint. (a), (d), (g) from 7 February 2021 14:37:28 UTC, (b), (e), (h) from 17 December 2020 16:26:01 UTC, and (c), (f), (i) from 17 December 2019 16:23:59 UTC.

When calculating the background average, a minimum fraction of valid points within the footprint can be set so only pixels with a sufficient amount of surrounding echo are used in the analysis. We use a minimum fraction of 0.75 (i.e. the footprint must contain at least 75% echo coverage to be used in the analysis). This is done to minimize artifacts on the edge of the echo. The effects of the 0.75 minimum fraction can be seen in the background average field in Fig. 4.3 where there are discrepancies between the echo edges in the snow rate field (panels d-f) and the echo edges in the background field (panels g-i). Changing this value only acts to change how much echo must be present in the footprint to be considered in the algorithm. Smaller values will mean that less features will be detected along the edge of the echo, while larger values closer to 1 will include all regions of the echo.

Two adaptive differential thresholds for finding feature cores

The background average field and the original snow rate field are compared using two "difference threshold schemes". Pixels where the difference between the snow rate field and the background average field are greater than or equal to the adaptive difference threshold constitute a feature's "core".

There are two individual pixel versus background difference relationships built into the algorithm, a "cosine scheme" and a "scalar multiplier scheme" that are used on combination. A pixel is identified as feature core if the value of the pixel exceeds the background by either adaptive threshold. If the pixel is only identified as a core with the scalar multiplier scheme, it is labeled as a faint feature. If it is identified as a core with the cosine scheme it is labeled as a strong feature. The cosine relationship has a decreasing threshold with increasing background value (Fig. 4.4a). One of the original methods created by Steiner et al. (1995) defined a curve relationship between the background reflectivity and reflectivity difference based on manual iterative adjustments. Yuter and Houze (1997) used a cosine function as it was a simple way to define a curve with more intuitive parameters. The cosine scheme is meant to identify objects that are generally more distinct from the background. We developed the scalar multiplier scheme to have an increasing threshold with increasing background value which acts to identify objects that are not very distinct from the background value (Fig. 4.4b). After extensive testing on many idealized and real examples from winter storms, we found that a combination of both types of adaptive thresholds was needed in order to detect the full range of reflectivity features from faint to strong. The cosine scheme only identifies objects that are very distinct from the background, while the scalar multiplier scheme identifies objects that are both very distinct and not very distinct. We chose the particular equations described here as they were both intuitive and easy to tune.

The cosine scheme's decreasing difference threshold with increasing background value is

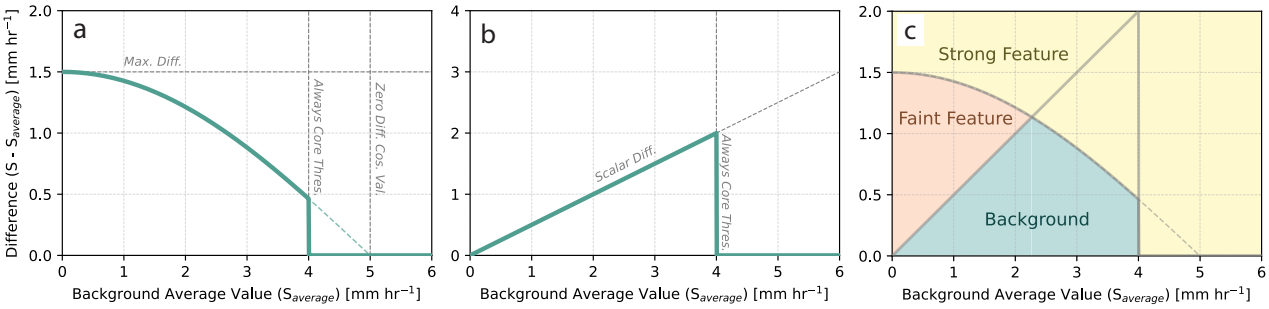

Figure 4.4: Adaptive difference relationships used to determine the threshold between a pixel and its background value to designate the pixel as a feature core. (a) cosine scheme and (b) scalar multiplier scheme. Panel (c) shows the difference relationships in (a) and (b) and is shaded based on the where each feature type is found. Note y-axis range in (b) extends further than in (a) and (c). Input parameters used for tuning are annotated with gray dashed lines, see text for full details.

described in Equation 4.1 where S represents the snow rate at a pixel, $S_{average}$ represents the background average snow rate, a represents a maximum possible difference value corresponding when the background average value is 0 mm hr^{-1} and b represents the background average value where the corresponding difference threshold is zero.

$$\mathrm{S} - \mathrm{S}_{average} \geq a \cos\left(\frac{\pi \mathrm{S}_{average}}{2b}\right) \tag{4.1}$$

Other similar equations with a decreasing threshold with increasing background value would also likely be suitable. The cosine scheme (Fig. 4.4a) is adapted from methods used to identify convective and stratiform precipitation structures in rain (e.g. Steiner et al. 1995; Yuter and Houze 1997; Yuter et al. 2005; Powell et al. 2016). The choice of this specific equation is purposeful as it permits the same Python code to be used with an input field of radar reflectivity from a rain layer and appropriate parameter settings to exactly reproduce the data processing of the original C++ code used in Yuter et al. (2005).

Figure 4.4a shows how changing the maximum difference (a in Eqn. 4.1; horizontal dashed line) and zero difference cosine value (b in Eqn. 4.1; vertical dashed line where the function would cross the x-axis) changes the overall shape of the difference function and thus the thresholds used to identify pixels that are cores. Having a lower maximum difference or zero difference cosine value will increase the number of cores since it relaxes the difference threshold needed for a point to be considered a core. The final tuning parameter in the difference relationship is the "always core threshold" which is the value above which all background points are considered cores (vertical dashed line in Fig. 4.4). Having an absolute threshold like the "always core threshold" is necessary for identifying large cores that would not be picked up distinguished

from the background field. In our method, the value corresponding to a pixel that is always part of a snow band is set at an equivalent liquid precipitation rate of 5 mm hr^{-1} (which corresponds to a reflectivity value of 30 dBZ). For reflectivity fields in rain, usually this value is set at or above 40 dBZ (rain rate of about 13 mm hr^{-1}).

The scalar multiplier scheme uses a linear function with a difference threshold that increases with increasing background value up to the "always core threshold" (Fig. 4.4b). The equation for the scalar multiplier scheme is described by Eqn. 4.2 where S represents the snow rate at a pixel, $S_{average}$ represents the background average snow rate, c represents the scalar difference.

$$\mathrm{S} - \mathrm{S}_{average} \geq (c * \mathrm{S}_{average}) - \mathrm{S}_{average} \tag{4.2}$$

The scalar difference value (c in Eqn. 4.2) changes the slope of the difference threshold in Fig. 4.4b). A larger scalar difference value will yield a steeper slope and a greater difference threshold needed for a given background average value.

Figure 4.4c shows both difference equations and is colored coded by classification (strong feature, faint feature, background) based on the two different schemes.

A detection threshold that increases with increasing background value helps to distinguish both the feathered edges of stronger features as well as features that differ only slightly from the background. Figure 4.5 shows three examples of the output from both the cosine scheme and the scalar scheme. Both the cosine scheme and the scalar scheme pick up the strong features from the snow rate (e.g. band of 10+ mm hr^{-1} in Fig. 4.5b), but only the scalar scheme can identify the weaker features including the fuzzy, feathered edges.

Converting cores to contiguous features

To address isolated pixels within detected features, we perform a binary closing on the 2D array of cores to mitigate these artifacts (Fig. 4.6a). A binary closing is an image dilation followed by an image erosion which acts to fill in the holes within a feature but keeps the feature at roughly the original size (Jamil et al. 2008). We use a quasi-circular 5x5 kernel (Fig. 4.6b) for the binary closing to yield a more physically realistic output as opposed to use of a square kernel.

After we perform the binary closing step, we then remove objects that are less than 120 km^2 in area. We found that this value was suitable for our applications. No object capable of meeting the band criteria of Ganetis et al. (2018) is less than 120 km^2 in area. An example of the binary closing and small object removal on the cosine scheme cores from the examples presented in Fig. 4.5 is shown in Fig. 4.7 to yield the filtered, spatially contiguous features of interest.

There were two steps from the established convective-stratiform algorithm that we turned

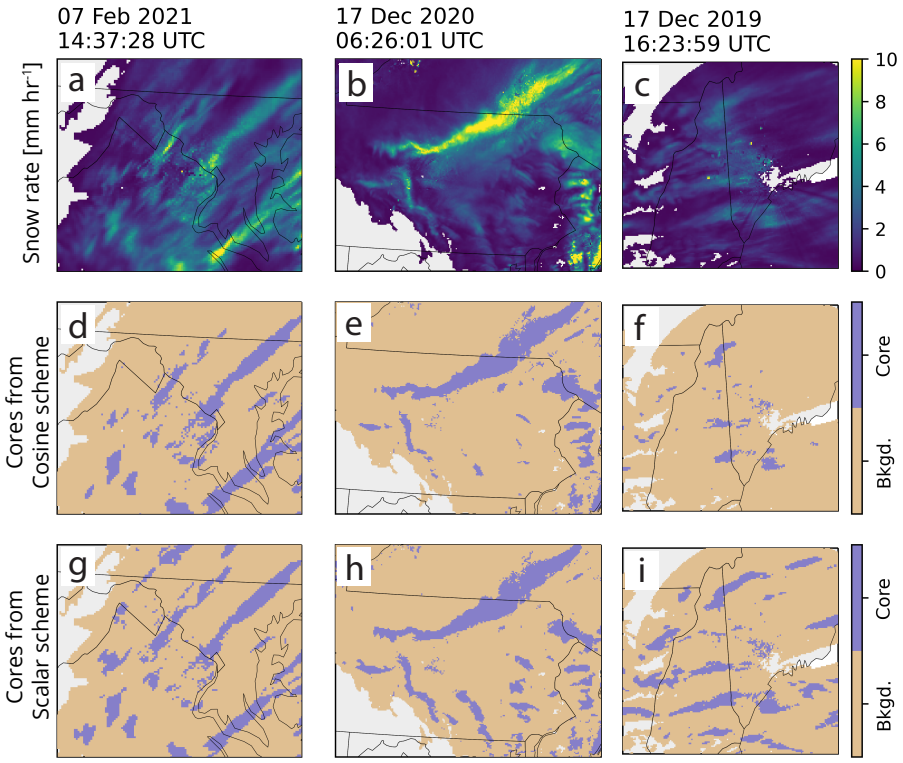

Figure 4.5: Close-up examples of (a)-(c) snow rate [mm hr^{-1}], (d)-(f) feature cores detected with the cosine scheme, and (g)-(i) feature cores detected with the scalar scheme. Same example dates and times as in Fig. 4.3.

a) Binary closing operation

b) Kernel used for operation

0	0	1	0	0
0	1	1	1	0
1	1	1	1	1
0	1	1	1	0
0	0	1	0	0

Figure 4.6: (a) Example of binary closing operation (image morphology dilation then erosion) from `https://docs.opencv.org/4.x/d9/d61/tutorial_py_morphological_ops.html` and (b) kernel used in binary closing operations.

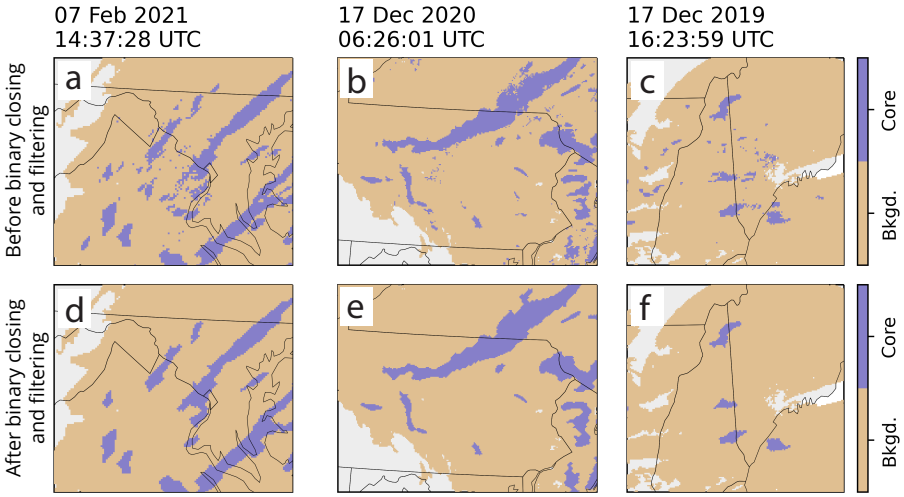

Figure 4.7: Close-up examples of feature cores from cosine scheme before (a)-(c) and after (d)-(f) binary closing and removal of small objects. The bottom row represents the filtered cores. Same example dates and times as in Fig. 4.3.

off for our feature detection application to winter storms. An additional step can be applied to delineate a weaker echo subset of the background echo. We do not use this for our application and set both the weak echo and minimum value to 0 mm hr^{-1} (Table 4.1). Alternate values of these settings can be useful for tabulating statistics of different magnitudes of background radar echo.

For the radar data set we were using, we found that the additional step of use a radius of influence around each core pixel as part of the feature was not needed. To turn this off, we set the maximum core radius to 2 km, the same as the input grid pixel size (Table 4.1). For some applications, the radius of influence step may be needed, especially for finer grids.

Snow storm faint and strong feature identification method

Objects that are identified by the cosine scheme we define as "strong" objects, while objects that are only identified by the scalar multiplier and not by the cosine scheme are defined as "faint" objects (Fig. 4.8). The separation into strong and faint objects allows for analysis that addresses the relative intensity of the observed reflectivity compared to independent data sets such as surface weather station snow rates. The output of the algorithm can yield strong and faint portions of the same contiguous feature as well as objects that are solely of one type (Figure 4.8ghi).

An important component of running the algorithm in practice is to account for uncertainties in the observed data and that no one method for feature detection will work perfectly in all

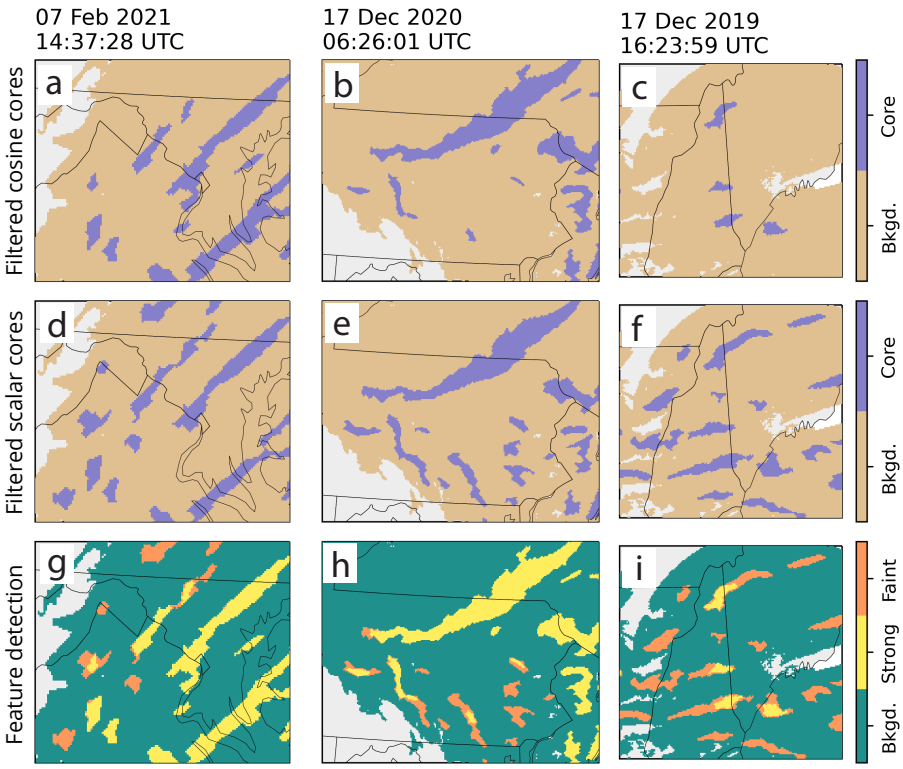

Figure 4.8: Close-up examples of (a)-(c) filtered features from cosine scheme, (d)-(f) filtered features from scalar scheme, and (g)-(i) feature detection output wherein portions of objects labeled as strong were detected in the cosine scheme and those labeled faint are only detected in the scalar scheme. Same example dates and times as Fig. 4.3.

situations. Similar to Yuter et al. (2005), we bound our feature identification by running the algorithm on the estimated snow rate field and two offsets of that field with slightly higher and lower values to yield purposeful over and under estimates of the feature detection. Increasing the radar reflectivity by 2 dB, converting to snow rate, and then running the algorithm yields an overestimate in feature area, while decreasing by 2 dB yields an underestimate. For the underestimate, echo where the original reflectivity field $\leq$ 2 dB gets removed, so the underestimate feature detection field will have less total echo area than the best and overestimate feature detection fields. Bounding the best estimate feature detection field can be accomplished by varying the input field slightly as we have done here, or by varying the difference equation. Both accomplish the same goal of making minor adjustments to yield an under and over estimate in the field. We recommend adjusting the field by at least $\pm$ 2 dB as this value is close to the minimum uncertainty in the US NWS operational radar reflectivity calibrations. As compared to the "best estimate", the underestimate version usually reduces the size of strong features and amplifies the detection of faint features compared to the best estimate. The overestimate version the snow field usually yields larger feature sizes for the strong features and damps the detection of the faint features compared to the best estimate.

4.3 Examples

We illustrate our algorithm on regional composites of Level-II data from National Weather Service (NWS) Next-Generation Radar (NEXRAD) network radars that were obtained from the NOAA Archive on Amazon Web Services (Ansari et al. 2018). Full details on how the composites are created can be found in Section 2.1 of Tomkins et al. (2022).

After we run the algorithm to detect features, we apply image muting (Tomkins et al. 2022) to identify regions of mixed precipitation in the winter storms. This step de-emphasizes portions of the echo that pass through the 0°C level. The sharp temperature gradients in winter storms can yield mixed precipitation echo regions that resemble bands (e.g. Picca et al. (2014) their Fig. 2 and Colle et al. (2023) their Fig. 7) and it is important to remove these mixed phase echoes before interpreting the detected features as snow.

Our examples span a range of cases and snow band intensities including storms with and without primary bands and multi-bands. The example from 7 February 2021 (left panel in Fig. 4.3, 4.5, 4.7, and 4.8) shows several strong bands over Maryland and Virginia and a few faint objects as well. The one from 17 December 2020 (middle panel in Fig. 4.3, 4.5, 4.7, and 4.8) includes a strong primary band over northern Pennsylvania and southern New York and several faint bands over southern Pennsylvania. The data from 17 December 2019 (right panel in Fig. 4.3, 4.5, 4.7, and 4.8) contains mostly faint bands over New Hampshire and Maine. All the

cases shown also include portions of echo that contain mixed precipitation which commonly occurs in east coast US winter storms. In each of the example regional cases, video supplements illustrate the time continuity of the detection method as features evolve and move through the domain.

4.3.1 Application in snow layers to identify faint and strong reflectivity features

The spatial and temporal coherence of the bands is illustrated in the sequences of images ± 1 hour for each of Fig. 4.9, 4.10, 4.11, 4.12 in the Video Supplement. Individual bands form and dissipate as the storm moves and evolves. A key goal of the algorithm development was to minimize *flashing* on and off of individual features in consecutive times.

The winter storm from 7 February 2021 at 14:37 UTC exhibited a primary band extending from northern Virginia to Connecticut and faint multi-bands across Pennsylvania and New York (Fig. 4.9). The underestimate field (Fig. 4.9c) also has a strong primary band similar to the best estimate although smaller and narrower. The few, small strong features in the best estimate are detected as faint features in the underestimate (Fig. 4.9c). The overestimate field (Fig. 4.9d) has a wider strong band compared to the best estimate and has more strong objects in general compared to the best estimate. The strong, primary band traverses along the east coast while the faint multi-bands dissipate and form in the weaker region in Pennsylvania and New York. (Video Supplement Animation-Figure-4.9).

The winter storm from 17 December 2020 over the Northeast US (Fig. 4.10) contained primary and multi-bands. There are several large bands that extend over New York and Massachusetts that are associated with high values in the snow rate field and are identified as strong features (Fig. 4.10). Over southern Pennsylvania there are other features that do not stand out as much that are identified as faint features (Fig. 4.10). As the storm evolves, the large band remains roughly in the same location but changes shape while the other, smaller features undergo more dramatic changes (e.g. dissipate, break apart, strengthen) (Video Supplement Animation-Figure-4.10). The faint bands over Pennsylvania also evolve in time and space, some transitioning to strong bands and some weakening and dissipating (Video Supplement Animation-Figure-4.10). Similar to the previous example, the under estimate has a narrower primary band and has a lot more "faint" features compared to the best and over estimates. The over estimate shows very few faint features and mostly amplifies the main strong features (Fig. 4.10d).

The winter storm on 17 December 2019 was generally weaker and had a lot of faint bands compared to the example from 17 December 2020 (Fig. 4.11). Areas of the southern part of the

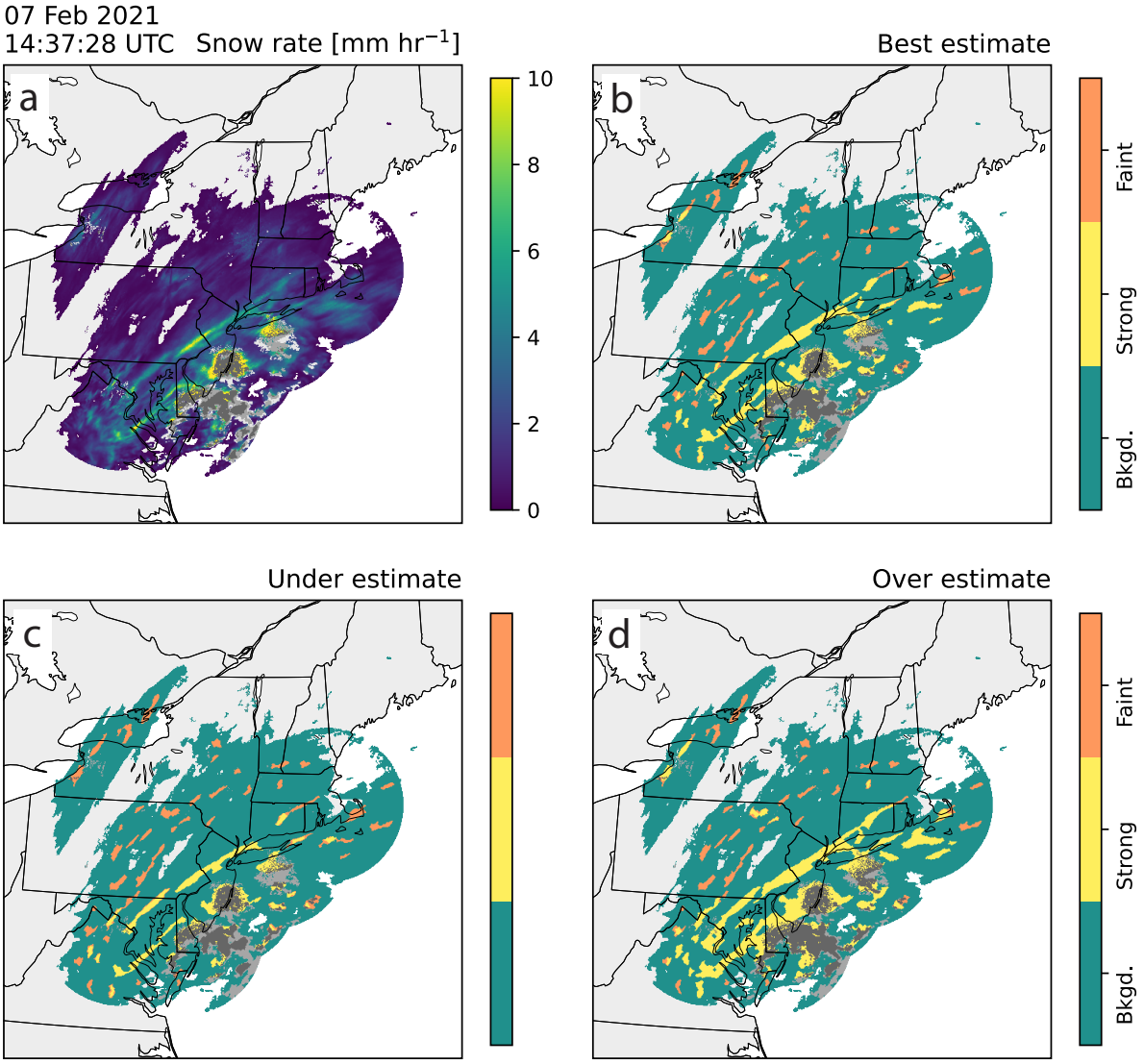

Figure 4.9: Demonstration of bounding the best estimate feature detection with purposeful overestimates and underestimates using an example from 7 February 2021 14:37:28 UTC which features a primary snow band and a few multi-bands. Locally enhanced features that include mixed precipitation are image muted in gray (Tomkins et al. 2022). (a) Re-scaled snow rate field (mm hr^{-1} units), Feature detection (b) best estimate, (c) underestimate, (d) overestimate. Feature detection fields show background regions in teal, strong features in yellow, and faint features in orange. An animated version of this figure is available in the Video Supplement Animation-Figure-4.9.

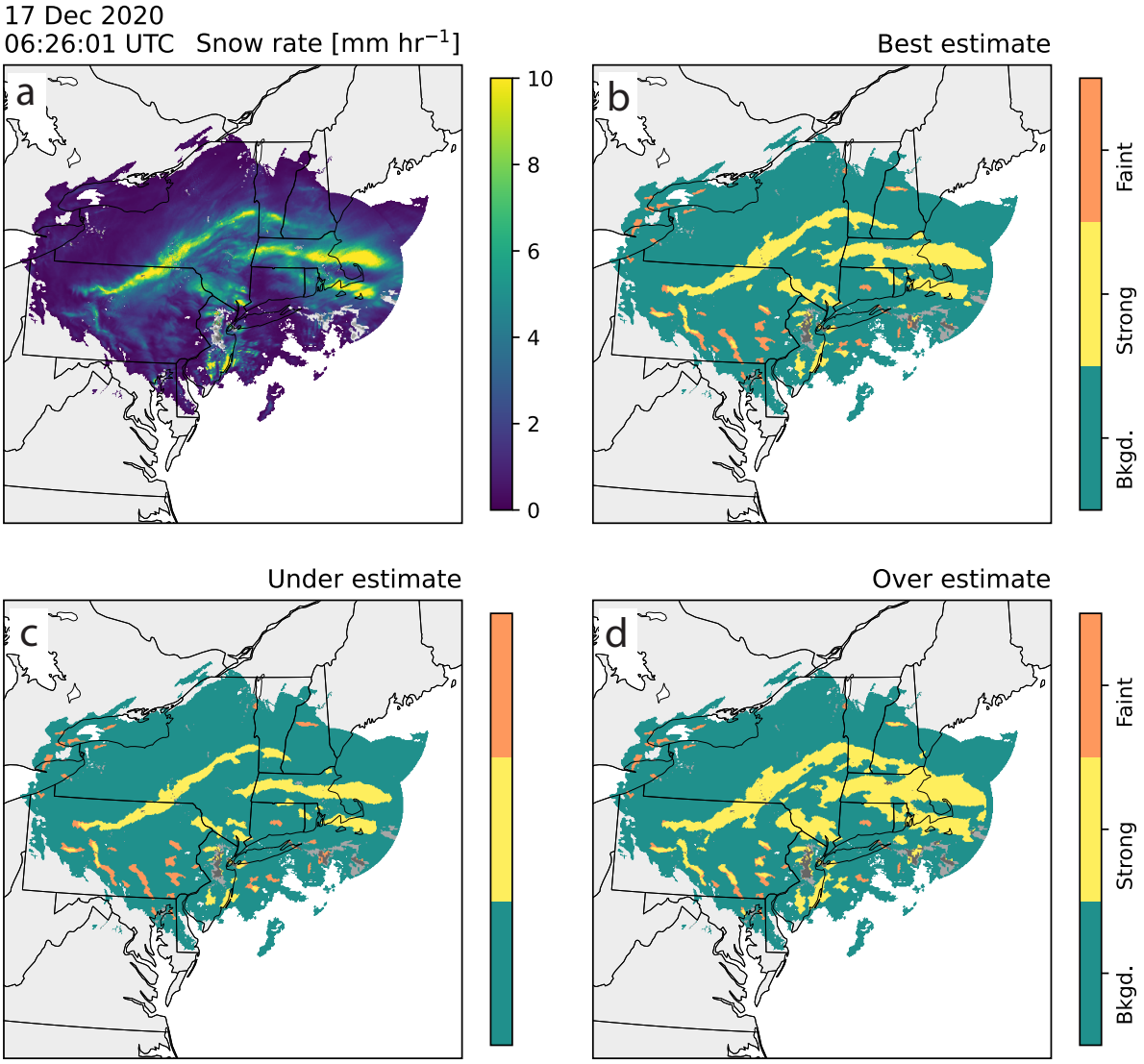

Figure 4.10: Demonstration of bounding the best estimate feature detection with purposeful overestimates and underestimates using an example from 17 December 2020 06:26:01 UTC which features several strong primary bands and a few faint multi-bands. Locally enhanced features that include mixed precipitation are image muted in gray. (a) Re-scaled snow rate field (mm hr^{-1} units), Feature detection (b) best estimate, (c) underestimate, (d) overestimate. Feature detection fields show background regions in teal, strong features in yellow, and faint features in orange. An animated version of this figure is available in the Video Supplement Animation-Figure-4.10.

storm are image muted, indicating melting and mixed precipitation and a transition to rain. The northern part of the storm has numerous faint features over northern New York, Vermont, New Hampshire, and Maine (Fig. 4.11a,b). In this example, the faint bands are more coherent in time and space than the other examples and some of these faint bands evolve into strong bands and some strong bands evolve into faint bands (Video Supplement Animation-Figure-4.11).

The winter storm from 7 February 2020 over the northeast US that is characterized by large regions of melting (grey muted regions in Fig. 4.12). This example has a large, strong object extending from Pennsylvania through New York but does not have any faint bands or sets of multi-banded structures as discussed in Colle et al. (2023) (Fig. 4.12). This large, long, strong feature spans the transition from snow to rain and is persistent in time for several hours (Video Supplement Animation-Figure-4.12). It is very likely that the portion of the strong band to the east of the SW-NW mixed precipitation area is rain rather than snow. Further feature filtering by surface air temperature fields would be useful in cases like this to isolate surface snow.

4.4 Summary

We present a novel method for identifying locally-enhanced features in radar observations of winter storms that uses a combination of increasing and decreasing adaptive thresholds as a function of average background values. Our method identifies features from a snow rate field that is rescaled from radar reflectivity in order to better automatically identify human eye discernable features in radar data of snow. Previous methods to automatically detect snow bands in radar observations either used inflexible thresholds and less precise reflectivity data or used adaptive thresholds that were not able to detect objects that are not very distinct from the background.This new method facilitates both the detection of stronger objects and fainter objects that are less distinct from the background average in snow storms. The wider range of characteristics of detected features provides a more comprehensive basis for examining hypotheses relating radar-observed features to surface snowfall and intra-storm environments.

The output of the algorithm described in this paper yields 2D arrays with categorical values for different strengths of detected radar echo features and background echo. These output arrays can be input into image processing software to yield statistics of feature characteristics such as area, aspect ratio, orientation, convex hull, centroid location, etc. (Yeh 2024). Object attributes can be used to further subset objects and for comparison to other independent data sources. Additionally, this algorithm can be applied to snow rate fields from numerical forecast model output to yield feature objects for use in nowcasting and for model evaluation.

Differential adaptive threshold methods for image segmentation that distinguish locally enhanced features from a varying background have applications to several areas in geosciences. In

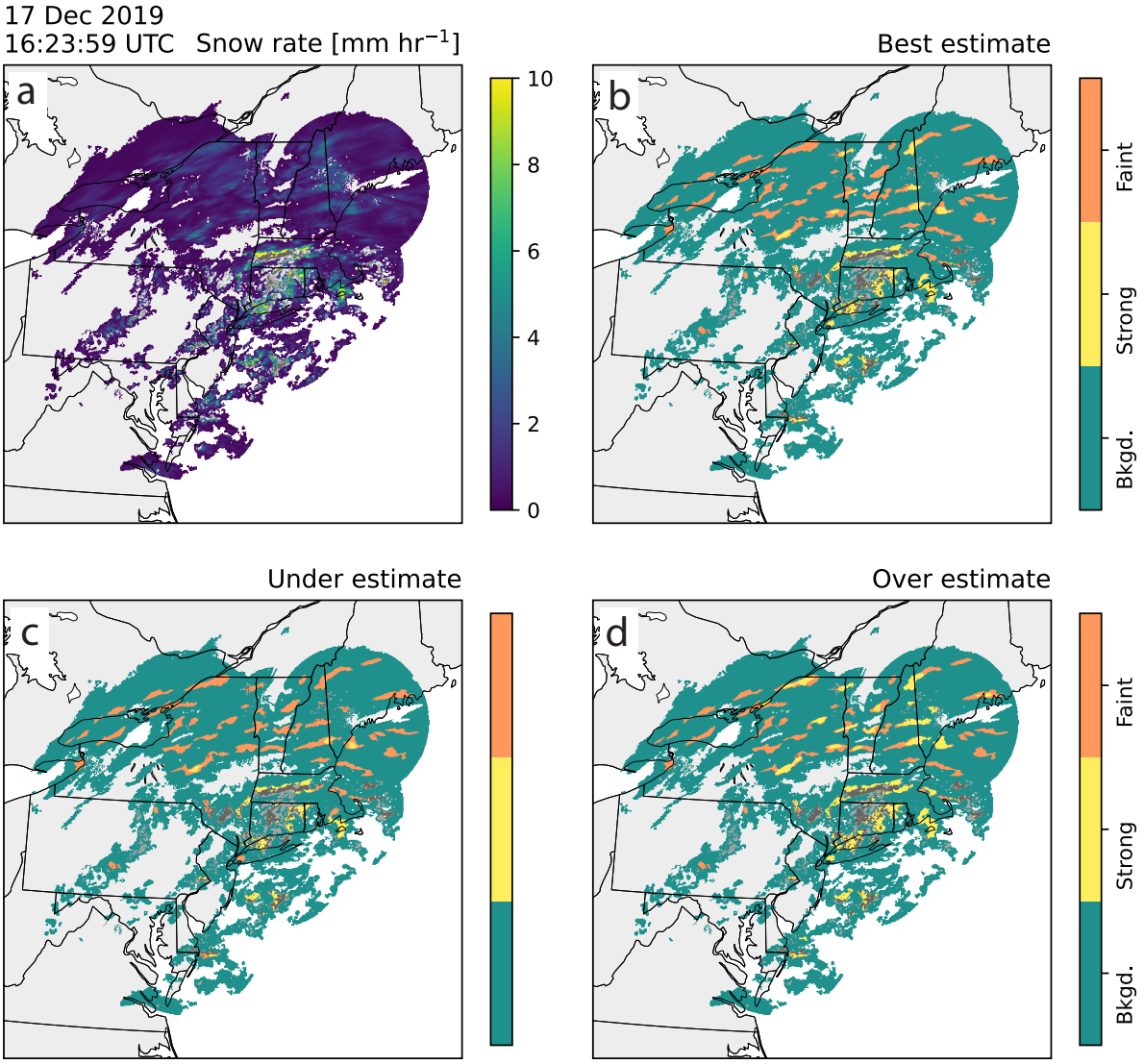

Figure 4.11: Demonstration of bounding the best estimate feature detection with purposeful overestimates and underestimates using radar example from 17 December 2019 16:23:59 UTC which features many faint multi-bands. Locally enhanced features that include mixed precipitation are image muted in gray. (a) Re-scaled snow rate field (mm hr^{-1} units), Feature detection (b) best estimate, (c) underestimate, (d) overestimate. Feature detection fields show background regions in teal, strong features in yellow, and faint features in orange. An animated version of this figure is available in the Video Supplement Animation-Figure-4.11.

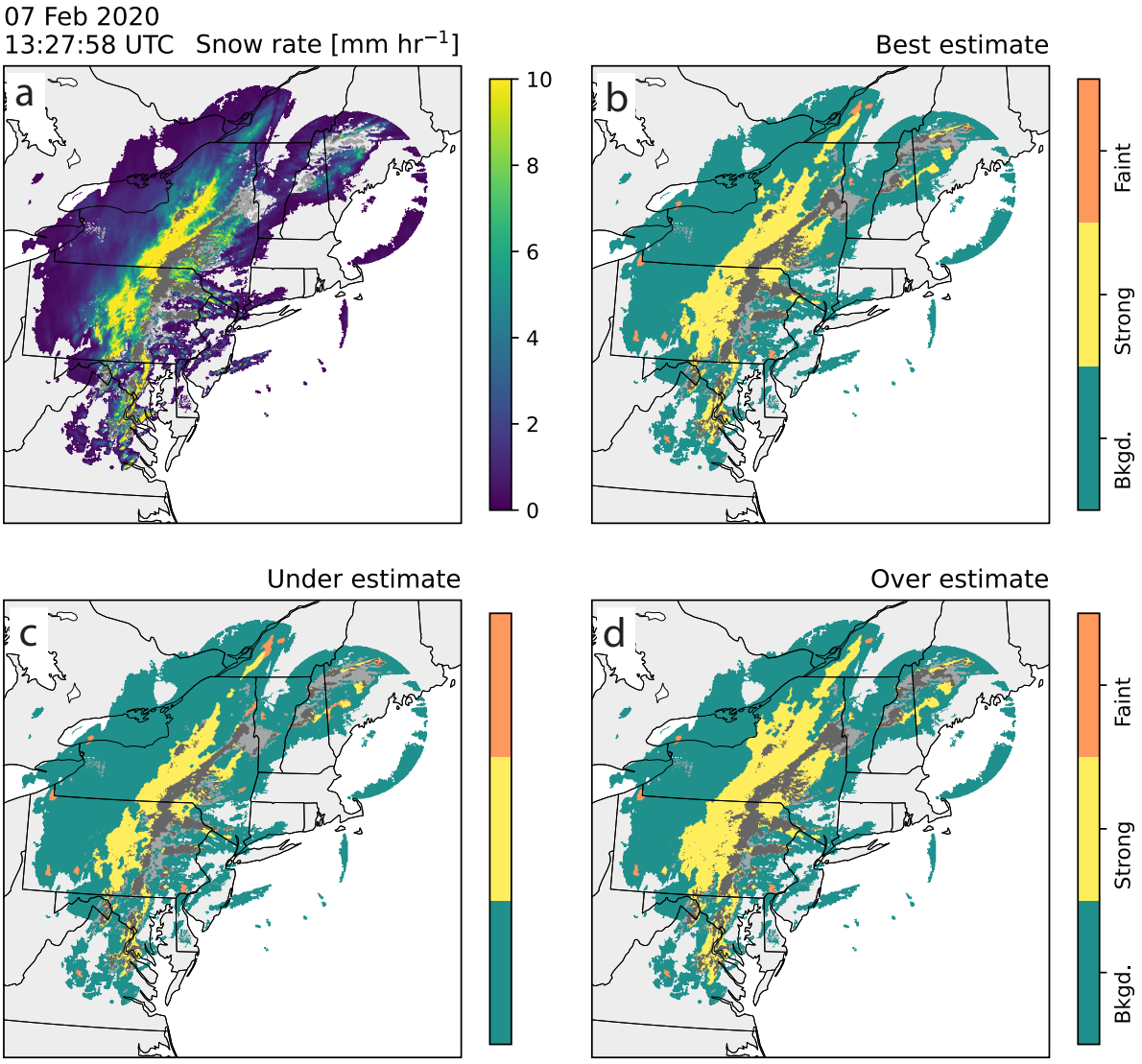

Figure 4.12: Demonstration of bounding the best estimate feature detection with purposeful overestimates and underestimates using radar example from 7 February 2020 13:27:58 UTC 17 which features a large primary band, portions of which are mixed precipitation and image muted in gray. (a) Re-scaled snow rate field (mm hr^{-1} units), Feature detection (b) best estimate, (c) underestimate, (d) overestimate. Feature detection fields show background regions in teal, strong features in yellow, and faint features in orange. An animated version of this figure is available in the Video Supplement Animation-Figure-4.12.

satellite data analysis, detection of cold cloud tops associated with deep convective storm anvils is often defined based on absolute IR brightness thresholds (Schiffer and Rossow 1983; Arkin and Meisner 1987; Machado and Rossow 1993) but tropopause heights can vary latitudinally, regionally, and seasonally. Additionally, satellite passive microwave brightness temperature signatures associated with local enhancements in scattering and emission by precipitation are harder to discern over the the more spatially varying thermal characteristics of land as compared to ocean (Ferraro et al. 2013).

Video Supplement All animations can be viewed at: `https://av.tib.eu/series/1524/`. Individual animations can be viewed by following the DOI URL.

Animation-Figure-4.9: Animated plot of Fig. 4.9 demonstrating bounding the best estimate feature detection with purposeful overestimates and underestimates using an example from 7 February 2021 13:30-15:30 UTC which features a primary snow band and a few multi-bands. Locally enhanced features that include mixed precipitation are image muted in gray (Tomkins et al. 2022). (a) Re-scaled snow rate field (mm hr^{-1} units), Feature detection (b) best estimate, (c) underestimate, (d) overestimate. Feature detection fields show background regions in teal, strong features in yellow, and faint features in orange.

Title: 07 February 2021 feature detection example DOI: `http://doi.org/10.5446/63170`

Animation-Figure-4.10: Animated plot of Fig. 4.10 demonstrating bounding the best estimate feature detection with purposeful overestimates and underestimates using an example from 17 December 2020 05:30-07:30 UTC which features several strong primary bands and a few faint multi-bands. Locally enhanced features that include mixed precipitation are image muted in gray. (a) Re-scaled snow rate field (mm hr^{-1} units), Feature detection (b) best estimate, (c) underestimate, (d) overestimate. Feature detection fields show background regions in teal, strong features in yellow, and faint features in orange.

Title: 17 December 2020 feature detection example DOI: `http://doi.org/10.5446/63171`

Animation-Figure-4.11: Animated plot of Fig. 4.11 demonstrating bounding the best estimate feature detection with purposeful overestimates and underestimates using an example from 17 December 2019 15:30-17:30 UTC which features many faint multi-bands. Locally enhanced features that include mixed precipitation are image muted in gray. (a) Re-scaled snow rate field (mm hr^{-1} units), Feature detection (b) best estimate, (c) underestimate, (d) overestimate. Feature detection fields show background regions in teal, strong features in yellow, and faint features in orange.

Title: 17 December 2019 feature detection example DOI: `http://doi.org/10.5446/63`

172

Animation-Figure-4.12: Animated plot of Fig. 4.12 demonstrating bounding the best estimate feature detection with purposeful overestimates and underestimates using an example from 7 February 2020 12:30-14:30 UTC which features a large primary band, portions of which are mixed precipitation and image muted in gray. (a) Re-scaled snow rate field (mm hr^{-1} units), Feature detection (b) best estimate, (c) underestimate, (d) overestimate. Feature detection fields show background regions in teal, strong features in yellow, and faint features in orange.

Title: 7 February 2020 feature detection example DOI: `http://doi.org/10.5446/63168`

Chapter 5

Radar-observed characteristics and surface snow rates

In this chapter we examine the role that radar-observed characteristics in winter storms have on the surface snowfall rates. Section 5.1 uses the features identified in Sec. 2.2.3/Chap. 4 to understand the impact of locally-enhanced reflectivity on surface snow rates. Section 5.2 uses the Doppler velocity waves classified in Sec. 2.2.5 to discern their relationship to surface snow rates.

5.1 Enhanced reflectivity features

5.1.1 Scanning radar enhanced reflectivity features and hourly snow rates

To examine the relationship between enhanced reflectivity features and surface snow rates, we compare the distributions of feature area × time fraction within 25 km of an ASOS station and the liquid equivalent precipitation rate reported at the ASOS station. The area × time fraction is calculated over the same hour that the precipitation accumulates. 2D distributions for both faint and strong features are shown in Fig. 5.1. Faint features (Fig. 5.1a) are most often associated with low and moderate snow rates (> 99%) and very rarely have heavy snow rates (< 1%). The area × time fraction for faint features also rarely exceeds 0.5 (0.7% of observations) which indicates that faint features occur over a small region for a short amount of time (Fig. 5.1). Strong features are also most often associated with low snow rates (Fig. 5.1b).

For the remainder of the analysis we will consider both faint and strong features together. Figure 5.2 shows a 2D distribution of all features (faint + strong) and Fig. 5.3 shows the information from Fig. 5.2 summarized in a bar chart. Considering the previous literature focused on snow banding in winter storms (Chap. 1), we were expecting to see a trend in the joint distribu-

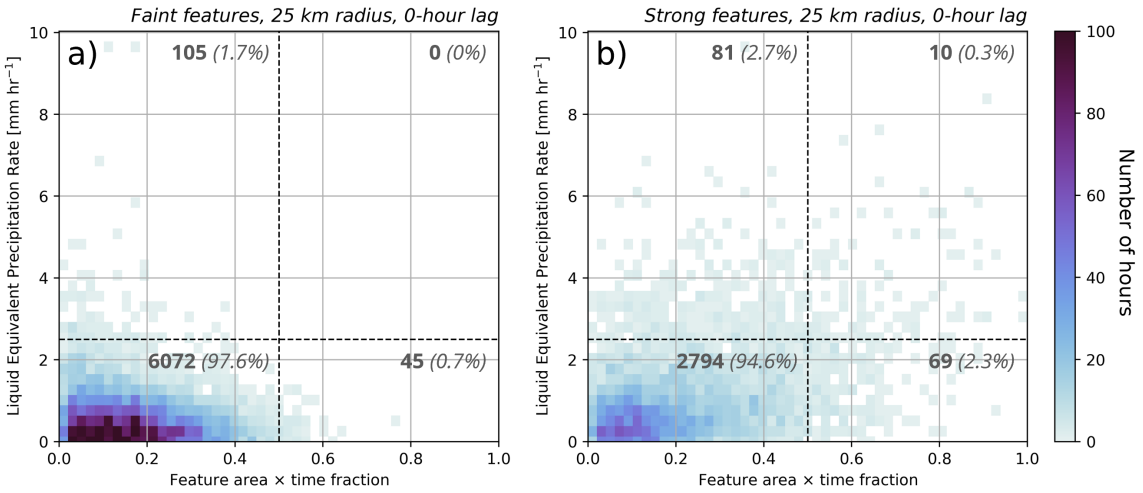

Figure 5.1: 2D distributions of (a) faint and (b) strong feature area × time fraction versus liquid equivalent precipitation rate [mm hr^{-1}] for snow observations. Area × time fraction calculated with a 25 km radius and observations are paired with a 0-hour lag. Zero feature area × time fraction observations are removed. 0.5 area × time fraction is annotated with a vertical black dashed line and 2.5 mm hr^{-1} is annotated with a horizontal black dashed line. Bold annotated numbers indicate number of hours in each quadrant and italicized numbers indicate percent of total observations in each quadrant.

tion indicating a relationship between increasing feature area × time fraction and increasing precipitation rate, however this is not the case for the large sample size examined in this study. Most points (89.1%) are clustered in the lower left box where both area × time fraction and precipitation rate are low. There are some observations where the area × time fraction and precipitation rate are high, however they only account for ∼1.5% of the observations when the feature area × time fraction is > 0. When the feature area × time fraction is > 0.5, 3 out of 4 times the surface snow rates will be < 2.5 mm hr^{-1}. The relationship between area × time fraction and precipitation rate is examined for several lag times (0, 1, and 2 hours) and several radii around the ASOS station (12.5, 25 and 50 km) in Sec. 5.1.4. While the details such as percentages in a given quadrant of the plot change a bit, the overall lack of relationship between area × time fraction and precipitation rate is unchanged.

We present representative examples of each category in Figs. 5.2 and 5.3. The first is an example when high feature area × time fraction and heavy snowfall are observed over an hour (Fig. 5.4). Panel a in Fig. 5.4 illustrates a large, strong feature over the Albany, NY ASOS station which contributes to a feature area × time fraction of 0.62 over the hour and coincides with an hourly liquid equivalent snowfall rate of 3.6 mm hr^{-1}. Later in this event, there are several hours at this station that were not included in our analysis because the wind speed was too high (blue plus signs in Fig. 5.4c). While we expected to see more examples of this scenario

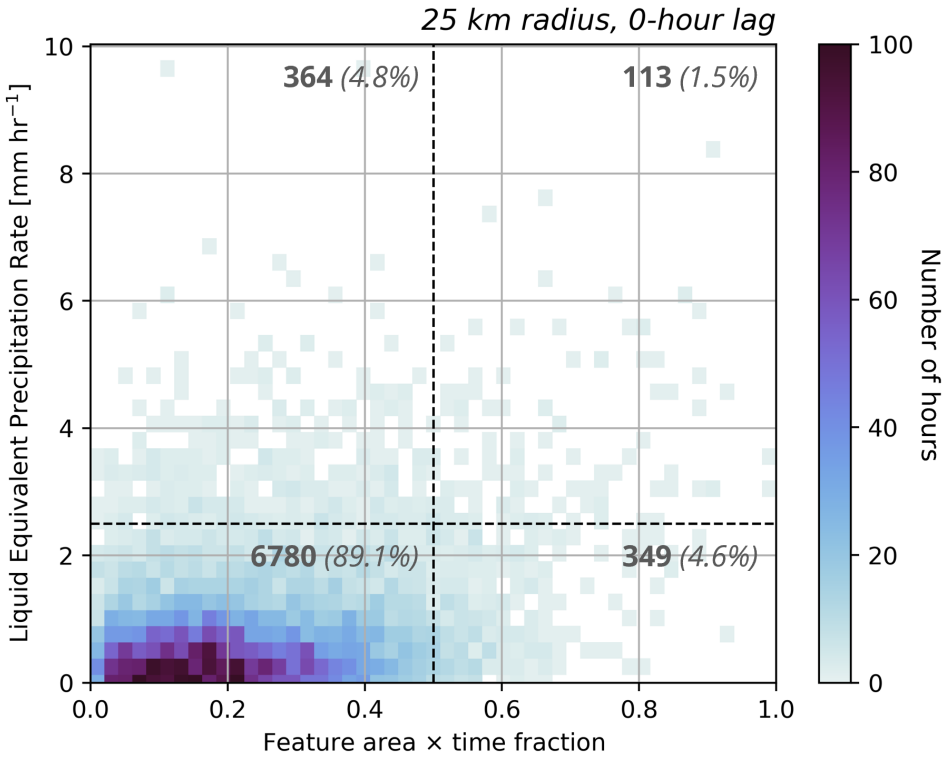

Figure 5.2: 2D distribution of all feature (faint + strong) area × time fraction versus liquid equivalent precipitation rate [mm hr^{-1}] for snow observations. Area × time fraction calculated with a 25 km radius and observations are paired with a 0-hour lag. Zero feature area × time fraction observations are removed. 0.5 area × time fraction is annotated with a vertical black dashed line and 2.5 mm hr^{-1} is annotated with a horizontal black dashed line. Bold annotated numbers indicate number of hours in each quadrant and italicized numbers indicate percent of total observations in each quadrant.

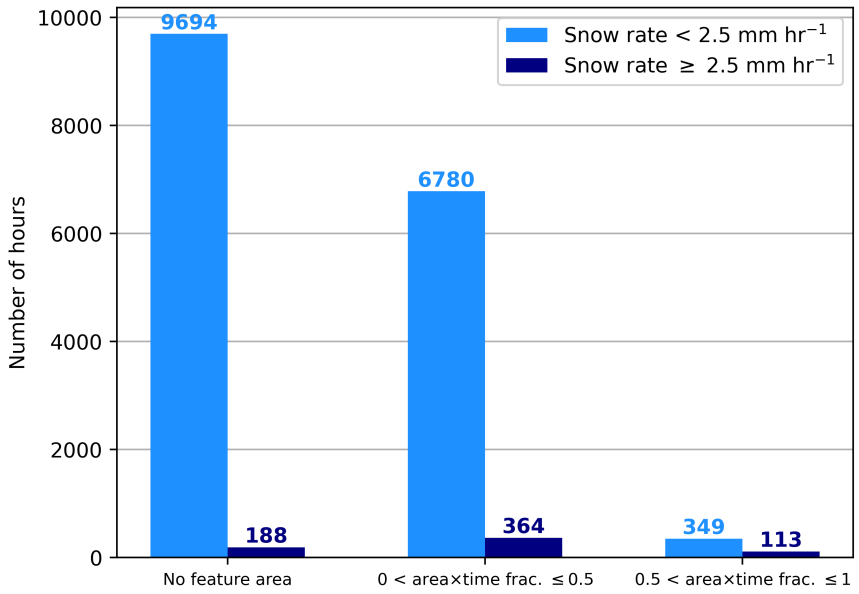

Figure 5.3: Bar plot of the four categories shown in Fig. 5.2. In addition, the far left category, no locally enhanced feature area (i.e. just background echo), is not shown in Fig. 5.2. Light blue bars represent light and moderate snow rates (< 2.5 mm hr^{-1}) and dark blue bars represent heavy snow rates (≥ 2.5 mm hr^{-1}).

(high feature area, heavy snowfall), it is representative of only 1.5% of hours in our dataset. Additionally, the feature resembles a primary band and is likely forced by frontogenesis which we would expect to fall into this category.

The second example is from an event on 26 January 2021 where several strong and faint features are moving through the region (Fig. 5.5a). In the snapshot in Fig. 5.5a, there is a strong feature over the Providence, RI ASOS station which contributes to a feature area × time of 0.58 over the hour (Fig. 5.5). While the feature area × time fraction is high (> 0.5) in this example, the snow rate is 2 mm hr^{-1} (Fig. 5.5c). This scenario when there is a high feature area × time fraction but only a low/moderate snow rate represents 4.6% of hours in our dataset.

The next scenario is the most common occurrence in our dataset where a low feature area × time fraction and a low/moderate snow rate is observed over the hour. This example from Lebanon, NH shows only a small faint object in the vicinity of the ASOS station and has a feature area × time fraction of 0.2 over the hour and a snow rate of 1.3 mm hr^{-1} (Fig. 5.6). For the remainder of the event there are no features in the vicinity of the ASOS station and the snow rate remains low/moderate (Fig. 5.6c). Scenarios similar to this when the feature area × time fraction is low and the snow rate is low account for 89% of observations.

Lastly, we have an example when the feature area × time fraction is low but the snow rate is heavy which occurs in 4.8% of our observations. This example from Worcester, MA shows an hour where the liquid equivalent precipitation rate was 9.7 mm hr^{-1} but the feature area × time

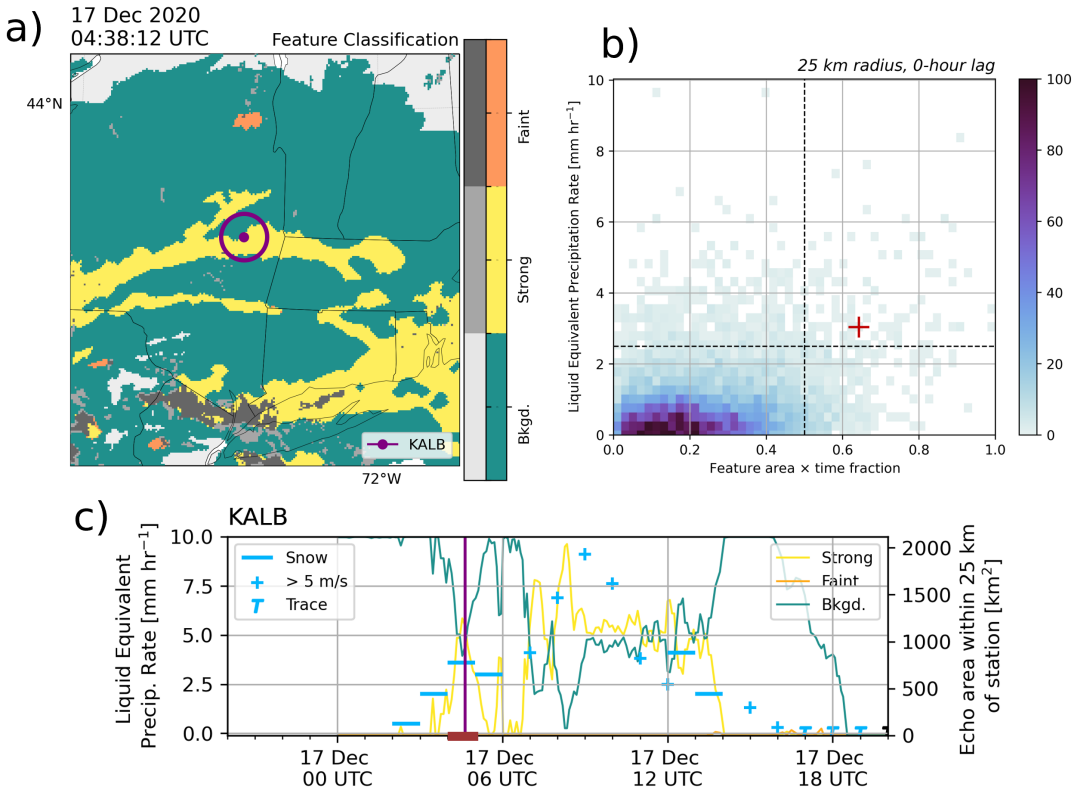

Figure 5.4: An example when a heavy snow rate (≥ 2.5 mm hr^{-1}) and high feature area × time fraction ($>$ 0.5) are observed over an hour. (a) Feature detection field from NEXRAD regional mosaic at 17 December 2020 04:38:12 UTC with Albany, NY ASOS station (KALB) and 25 km radius annotated in purple, (b) 2D distribution from Fig. 5.2 with specific hourly observation (04:00-05:00 UTC) annotated with red plus sign, and (c) time series of hourly precipitation rate over the entire event (16 December 20:00 UTC to 17 December 20:00 UTC) from KALB (blue annotations) and area of each feature category within 25 km of KALB (yellow: strong area, orange: faint area, and teal: background area). In (c), purple vertical line indicates time of specific NEXRAD regional mosaic in (a) and red bar on x-axis indicates the hour of observation at the red plus sign in (b).

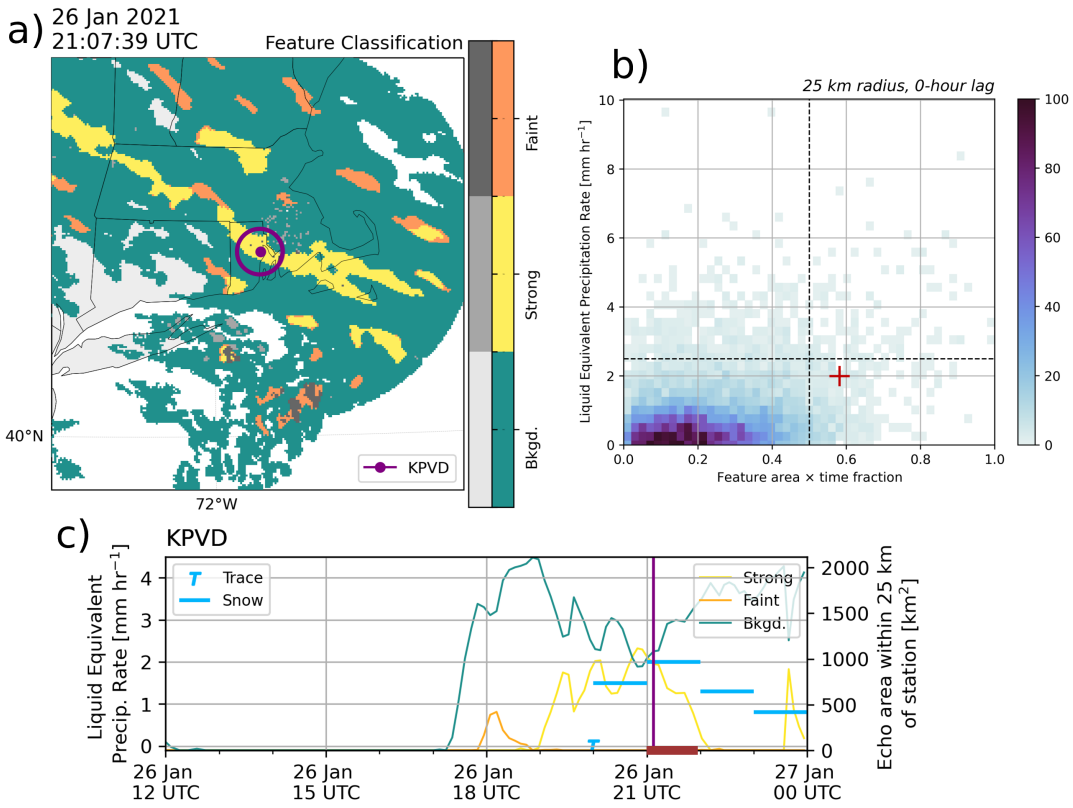

Figure 5.5: An example when a low/moderate snow rate (< 2.5 mm hr^{-1}) and high feature area × time fraction (> 0.5) are observed over an hour. (a) Feature detection field from NEXRAD regional mosaic at 26 January 2021 21:07:39 UTC with Providence, RI ASOS station (KPVD) and 25 km radius annotated in purple, (b) 2D distribution from Fig. 5.2 with specific hourly observation (21:00-22:00 UTC) annotated with red plus sign, and (c) time series of hourly precipitation rate over the entire event (26 January 12:00 UTC to 27 January 00:00 UTC) from KPVD (blue annotations) and area of each feature category within 25 km of KPVD (yellow: strong area, orange: faint area, and teal: background area). In (c), purple vertical line indicates time of specific NEXRAD regional mosaic in (a) and red bar on x-axis indicates the hour of observation at the red plus sign in (b).

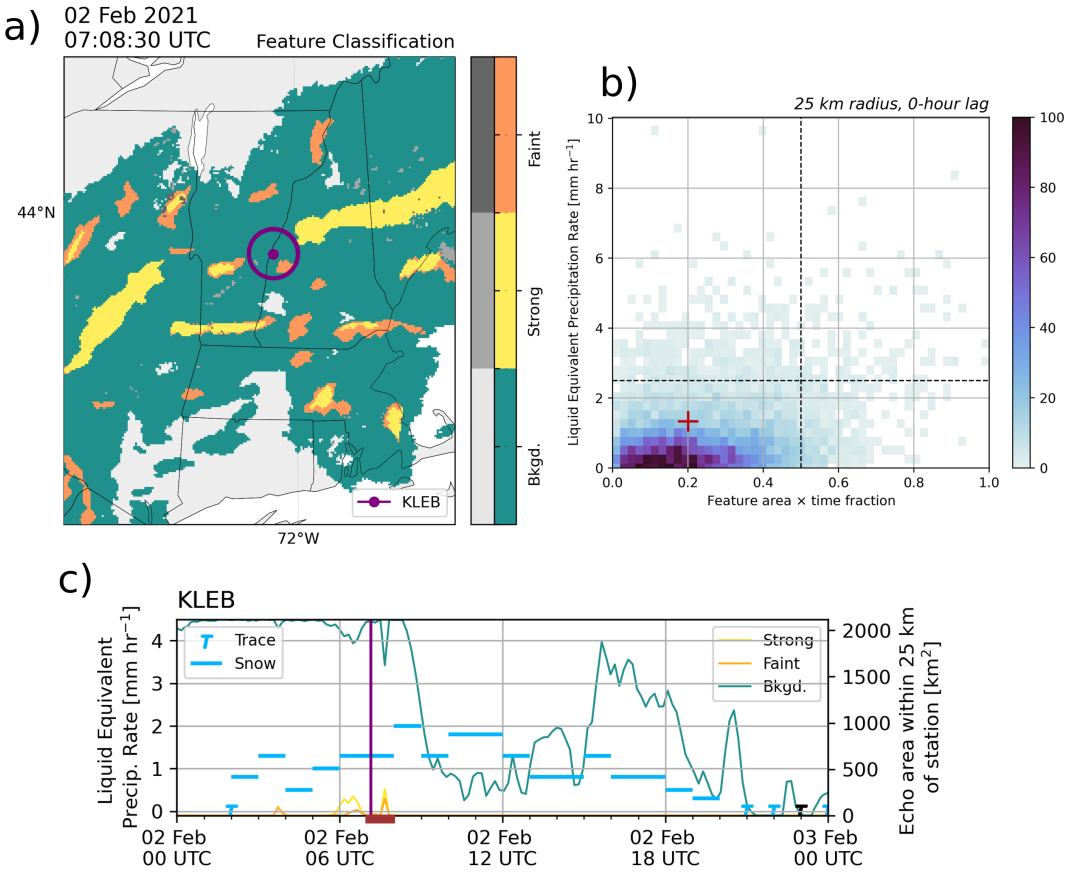

Figure 5.6: An example when a low/moderate snow rate (< 2.5 mm hr^{-1}) and low feature area × time fraction (≤ 0.5) are observed over an hour. (a) Feature detection field from NEXRAD regional mosaic at 02 February 2021 07:08:30 UTC with Lebanon, NH ASOS station (KLEB) and 25 km radius annotated in purple, (b) 2D distribution from Fig. 5.2 with specific hourly observation (07:00-08:00 UTC) annotated with red plus sign, and (c) time series of hourly precipitation rate over the entire event (02 February 00:00 UTC to 03 February 00:00 UTC) from KLEB (blue annotations) and area of each feature category within 25 km of KLEB (yellow: strong area, orange: faint area, and teal: background area). In (c), purple vertical line indicates time of specific NEXRAD regional mosaic in (a) and red bar on x-axis indicates the hour of observation at the red plus sign in (b).

fraction was only 0.12 (Fig. 5.7). There are a few faint features in the area, but overall the echo is patchy and not reminiscent of echo producing heavy snow. The time series shows that there are several times in this event where the snow rate was heavy but there were little or no features present over the station. These scenarios are commonly situations where there is long duration of background or all types of echo rather than mostly locally-enhanced reflectivity features. Additionally, because the height of the radar beam varies over the radar mosaics, it is possible that the storm is shallow and the radar beam does not detect any locally-enhanced features.

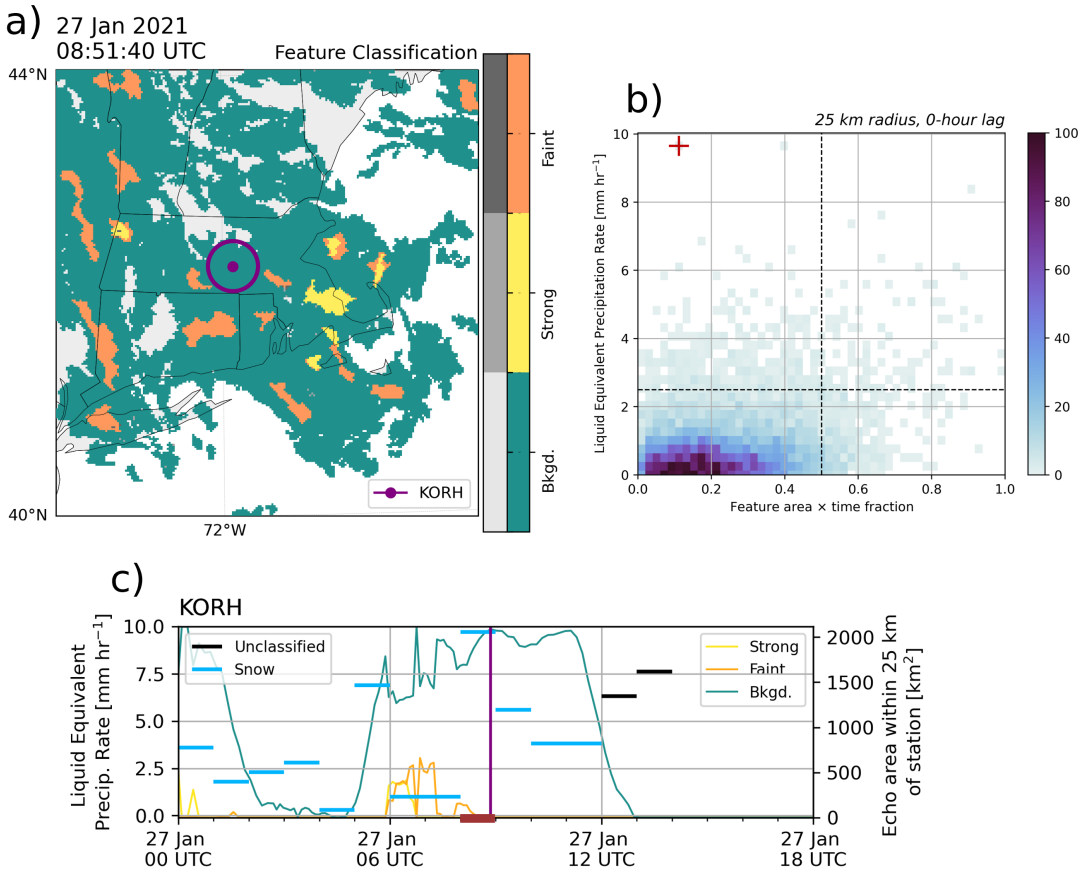

Figure 5.7: An example when a heavy snow rate (≥ 2.5 mm hr^{-1}) and low feature area × time fraction (≤ 0.5) are observed over an hour. (a) Feature detection field from NEXRAD regional mosaic at 27 January 2021 08:51:40 UTC with Worcester, MA ASOS station (KORH) and 25 km radius annotated in purple, (b) 2D distribution from Fig. 5.2 with specific hourly observation (08:00-09:00 UTC) annotated with red plus sign, and (c) time series of hourly precipitation rate over the entire event (27 January 00:00 UTC to 27 January 18:00 UTC) from KORH (blue annotations) and area of each feature category within 25 km of KORH (yellow: strong area, orange: faint area, and teal: background area). In (c), purple vertical line indicates time of specific NEXRAD regional mosaic in (a) and red bar on x-axis indicates the hour of observation at the red plus sign in (b).

5.1.2 Normalized distributions

The distribution in Fig. 5.2 is skewed towards lower snow rates. To remove this skewness, we normalize the distribution by the precipitation rate and by the area × time fraction (Fig. 5.8). The 2D distribution is normalized by precipitation rate by dividing each bin by the sum of observations in the given precipitation bin. Instead of a histogram normalized by all the observations, here, we interpret each point as the likelihood of an outcome given the precipitation rate or area × time fraction bin it has been normalized by. When we normalize the distribution in Fig. 5.2 by precipitation rate, the distribution's skewness to lower snow rates is visually removed (Fig. 5.8). Given that there are ∼15 times more observations where the snow rate is < 2.5 mm hr^{-1} as compared for ≥ 2.5 mm hr^{-1}, we can be more confident in distributions for the low snow rate subset. No strong relations between liquid equivalent snow rate and area × time fraction are evident in these normalized plots. For liquid equivalent precipitation ≥ 5 mm hr^{-1} and area × time fractions > 0.6, the sample size are very small even with this 264 storm day data set.

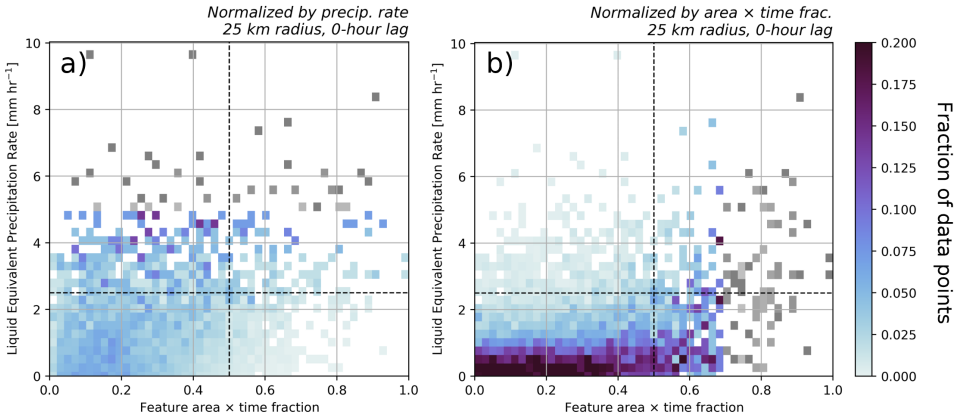

Figure 5.8: Normalized 2D distributions of all feature (faint + strong) area × time fraction versus liquid equivalent precipitation rate [mm hr^{-1}] for snow observations. (a) Normalized by liquid equivalent precipitation rate and (b) normalized by feature area × time fraction. Bins are color coded by the fraction of observations within each (a) precipitation and (b) area × time fraction bin. Bins in a grey scale indicate bins with less than 10 observations. Area × time fraction calculated with a 25 km radius and observations are paired with a 0-hour lag. Zero feature area × time fraction observations are removed. 0.5 area × time fraction is annotated with a vertical black dashed line and 2.5 mm hr^{-1} is annotated with a horizontal black dashed line.

5.1.3 Only background echo present

We also consider the subset of observations when there is only background echo present and the feature area × time fraction is 0 (i.e. when there are no enhanced reflectivity features surrounding the ASOS station). This subset corresponds to the left most category in Fig. 5.3. The 2D distribution of background area × time fraction (i.e. fraction is calculated with the background echo area only) and associated liquid equivalent precipitation rate indicates that the snowfall rates tend to be light but heavier rates can be present associated with larger background area × time fraction (Fig. 5.9). Hence, longer persistence of even just background echo over the site can occasionally yield snow rates ≥ 2.5 mm hr^{-1} .

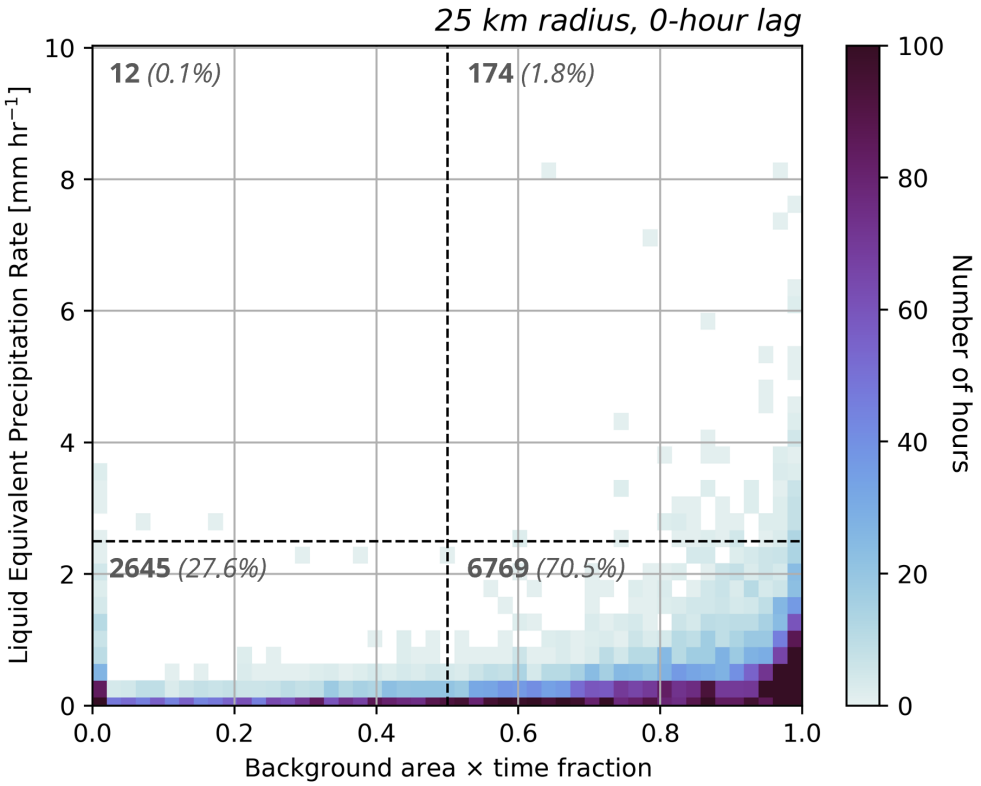

Figure 5.9: 2D distribution of background echo area × time fraction versus liquid equivalent precipitation rate [mm hr^{-1}] for snow observations when there are no locally enhanced features present (all echo area minus the area of faint and strong features). Area × time fraction is calculated with a 25 km radius and observations are paired with a 0-hour lag. 0.5 area × time fraction is annotated with a vertical black dashed line and 2.5 mm hr^{-1} is annotated with a horizontal black dashed line. Bold annotated numbers indicate number of hours in each quadrant and italicized numbers indicate percent of total observations in each quadrant.

5.1.4 Sensitivity of results

In this section we test the sensitivity of our results to the radius around the ASOS station, time lag, beam altitude over the ASOS station, the percent of mixed precipitation echo removed, and accumulation over a multi-hour time period.

Radius surrounding ASOS station

Since snow falls slowly ($\sim$1 m s^{-1}), it is easily advected by the wind and can be transported many kilometers horizontally from where it initially forms aloft. To account for this horizontal advection of snow, we test the sensitivity of the 25 km radius we chose in section 5.1. Figure 5.10 shows 2D distributions of feature area × time and precipitation rate for 3 different radii (12.5, 25, 50 km) around the ASOS stations. All 3 distributions are similar in that most of the observations are clustered in the bottom left quadrant (low feature area × time fraction and low precipitation rate; Fig. 5.10). As expected, the 12.5 km radius has slightly more points with high feature area × time fraction compared to the other two radii, while the 50 km radius has slightly fewer points with high feature area × time fraction.

The region that the area × time is calculated over is 4 times bigger for a 25 km radius than a 12.5 km radius and 16 times bigger for a 50 km radius than a 12.5 km radius. Hence, increasing the radius that the area × time fraction is calculated over results in increasing the skewness of the distribution so that it shifts further into the bottom left corner of the 2D distribution plots (i.e. lower feature area × time fraction, low precipitation rate). Changing the radius over which the area × time is calculated does not yield a relationship between increasing feature area × time fraction and increasing surface snow rates.

Time lag

Our results using a 0-hour lag (i.e. hour when feature area × time fraction is computed is compared to the same hour that the precipitation accumulates over) are compared to a 1-hour and 2-hour time lag (Fig. 5.11). Since the radar observations are 0-4 km above the surface and snow falls slowly ($\sim$1 m s^{-1}) we wanted to see if there was a lag between the area × time calculated from the radar data (above the surface) and the precipitation rate measured at the surface. A 1-hour time lag pairs observations with a 1-hour offset. That is, the feature area × time fraction is paired with the precipitation rate observations for the next hour. Similarly, a 2-hour time lag pairs observations with a 2-hour offset. Figure 5.11 shows the 2D distributions of feature area × time fraction and precipitation rate calculated with the 3 different time lags (0-, 1-, and 2-hour). Each distribution again has most of the observations clustered in the bottom left quadrant (Fig. 5.11). The 2-hour lag has less observations in the upper right quadrant, but

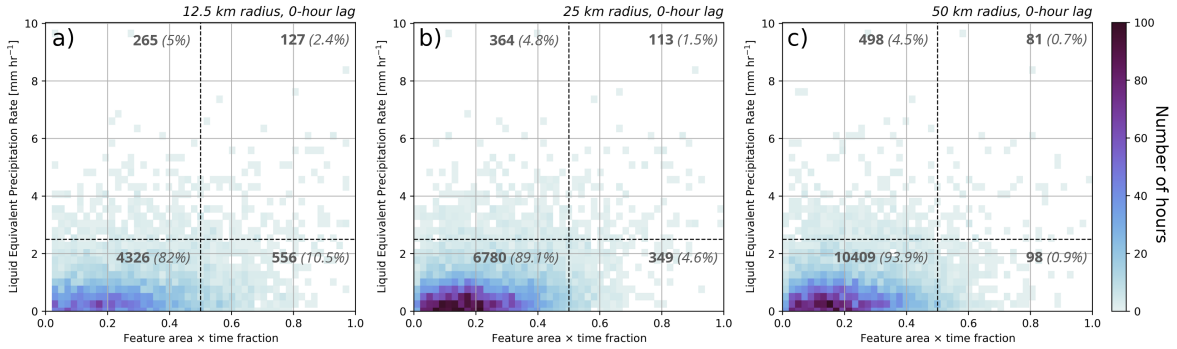

Figure 5.10: Sensitivity of results to radius over which area × time fraction is calculated. 2D distribution of feature area × time fraction versus liquid equivalent precipitation rate [mm hr^{-1}] for snow observations using (a) 12.5 km radius, (b) 25 km radius and (c) 50 km radius. Observations are paired with a 0-hour lag. Zero feature area × time fraction observations are removed. 0.5 area × time fraction is annotated with a vertical black dashed line and 2.5 mm hr^{-1} is annotated with a horizontal black dashed line. Bold annotated numbers indicate number of hours in each quadrant and italicized numbers indicate percent of total observations in each quadrant.

otherwise there are no strong differences between the distributions. The lack of substantial differences between the distributions indicates that our results are not sensitive to the time lag used to pair the ASOS and radar observations.

Beam height

Because our regional radar composites are created using the 0.5° elevation angle, the altitude of the points in the regional composites varies. It is possible that the variable altitude of the radar data and thus area × time fraction could impact our results. To understand the impact that the beam height has on the distributions, we calculate the average beam height within the area and over the hour that the area × time fraction is calculated (i.e. 25 km) and use that to threshold our distributions. Figure 5.12 shows the feature area × time fraction vs. precipitation rate 2D distributions for observations when the beam height is ≤ 1000 m, 2000 m, and 3000 m. Overall, there is very little differences between the distributions which indicates that the average beam height does not have a large impact on our results.

Mixed Precipitation Area Removed

Since we calculate the area × time fraction *after* removing areas that are image muted (regions that are likely melted or mixed precipitation), we test the sensitivity of our results to the percent of area removed from the echo area calculation. If the area surrounding a station has lots of muted regions over the hour, it could be underestimating the feature area × time

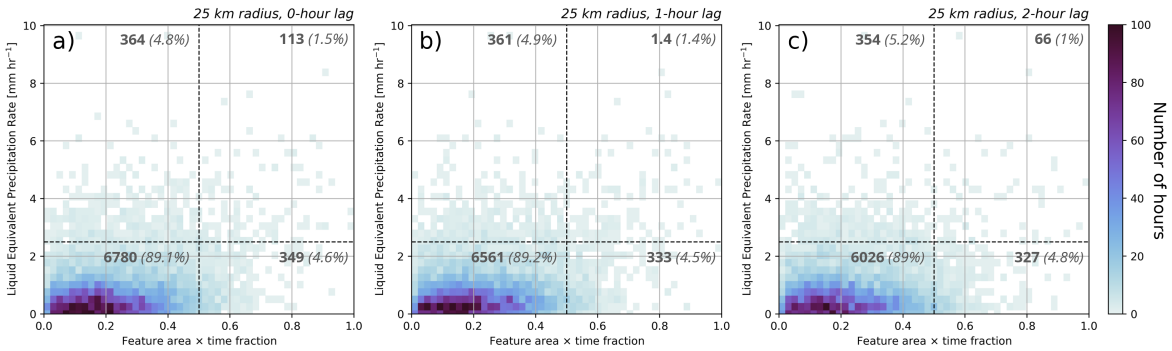

Figure 5.11: Sensitivity of results to time-lag between radar-observed area × time fraction and hourly surface snowfall rate. Area × time fraction calculated with a 25 km radius paired with (a) 0-hour lag, (b) 1-hour lag, (c) 2-hour lag surface snow rates. Zero feature area × time fraction observations are removed. 0.5 area × time fraction is annotated with a vertical black dashed line and 2.5 mm hr^{-1} is annotated with a horizontal black dashed line. Bold annotated numbers indicate number of hours in each quadrant and italicized numbers indicate percent of total observations in each quadrant.

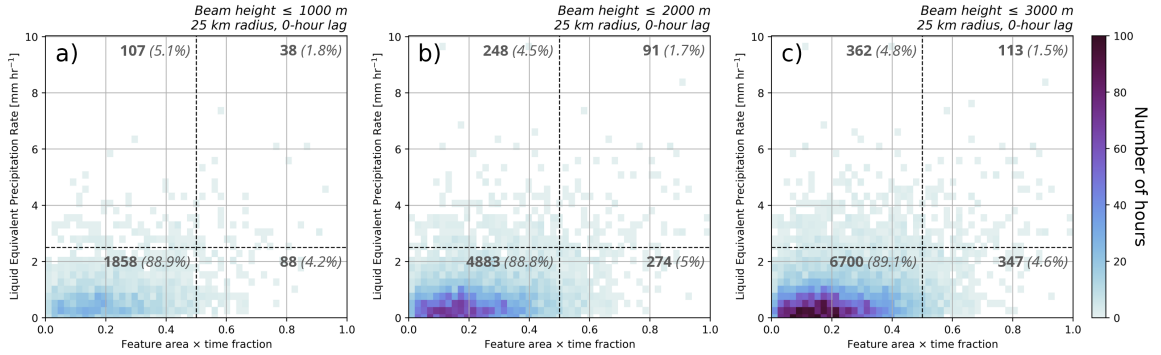

Figure 5.12: Sensitivity of results to beam height above ASOS station. 2D distribution of feature area × time fraction versus liquid equivalent precipitation rate [mm hr^{-1}] for snow observations. Area × time fraction calculated with a 25 km radius and and observations are paired with a 0-hour lag. Observations where the average beam height is greater than (a) 1000 m, (b) 2000 m, and (c) 3000 m are removed. Zero feature area × time fraction observations are removed. 0.5 area × time fraction is annotated with a vertical black dashed line and 2.5 mm hr^{-1} is annotated with a horizontal black dashed line. Bold annotated numbers indicate number of hours in each quadrant and italicized numbers indicate percent of total observations in each quadrant.

fraction. We threshold our distributions based on the percent of area muted averaged over the hour (Fig. 5.13). A percent muted threshold of 50% means that on average, the area surrounding the ASOS station was 50% muted over the hour. The threshold of 25% muted is the most strict in that is allows for the least amount of muting to be present. In fig. 5.13, panel c ($\leq$ 25%) is a subset of panel b and panel a, panel b ($\leq$ 50%) is a subset of panel a, and panel a ($\leq$ 100%) includes the entire dataset. Overall, there is not a lot of area muted – the 25% threshold only excludes 386 hours of data (5%). This is likely because we are only considering observations where it has been snowing for at least 4 hours so we wouldn't expect to see a lot of mixed precipitation regions. The distributions are very similar and do not change much with the change in percent muted which indicates that our results are also not strongly sensitive to this factor.

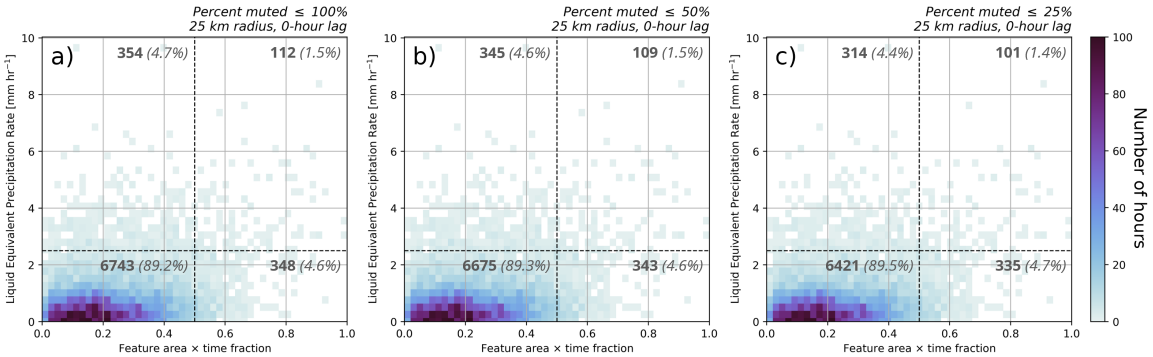

Figure 5.13: Sensitivity of results to average percent of echo area that is mixed precipitation over the hour. Area × time fraction in snow is calculated with a 25 km radius and and observations are paired with a 0-hour lag. Area × time fraction where the average area muted over the hour within 25 km is (a) $\leq$ 100$ (i.e. all observations, repeats Fig. 5.2), $\leq$ 50%, and (c) $\leq$ 25% are removed. 0.5 area × time fraction is annotated with a vertical black dashed line and 2.5 mm hr^{-1} is annotated with a horizontal black dashed line. Bold annotated numbers indicate number of hours in each quadrant and italicized numbers indicate percent of total observations in each quadrant.

Multi-hour accumulation

Lastly, we test the sensitivity of our results to the time the observations are accumulated over. Similar to testing the sensitivity of the time lag, we wanted to examine if accumulating over several hours changed the relationship between feature area × time fraction and precipitation rate. Up until this point, we have integrated the area × time fraction over an hour to correspond to the hourly precipitation accumulation reported by the ASOS stations. Figure 5.14 shows

distributions of the area × time fraction when accumulating both observations over a 2- and 3-hour period. The scale on the y-axis is larger than the previous plots since the observations have been summed over a longer period. In general, the patterns are similar to Fig. 5.2 and do not indicate that accumulating over multiple hours substantially changes the findings.

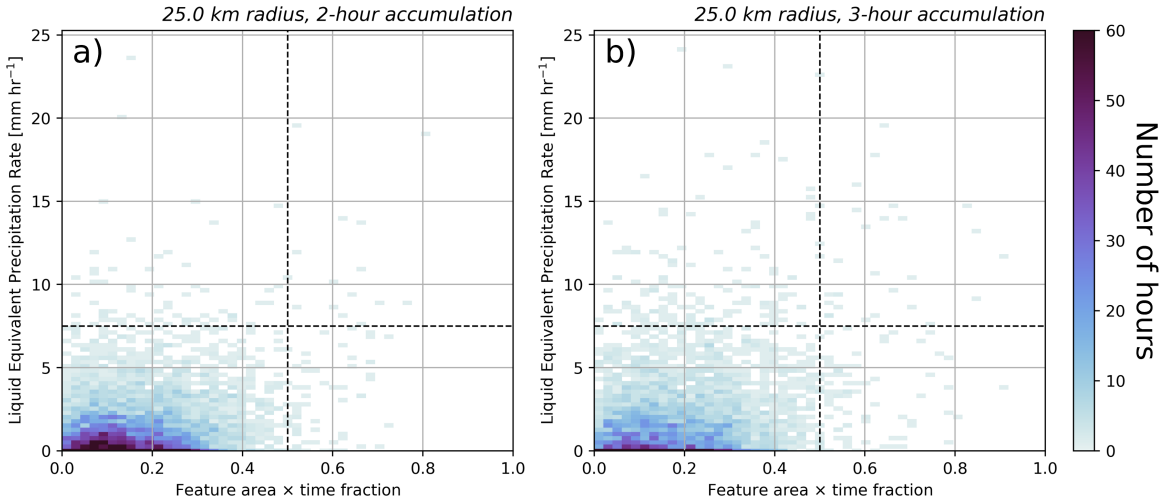

Figure 5.14: Sensitivity of results to number of hours of accumulation. 2D distribution of feature area × time fraction versus liquid equivalent precipitation rate [mm hr^{-1}] for snow observations accumulated over (a) 2 hours and (b) 3 hours. Area × time fraction calculated with a 25 km radius and and observations are paired with a 0-hour lag. Zero feature area × time fraction observations are removed. 0.5 area × time fraction is annotated with a vertical black dashed line and 7.5 mm hr^{-1} is annotated with a horizontal black dashed line.

5.1.5 Pragmatic considerations in nowcasting heavy snow using radar reflectivity observations

Heavy hourly snow rates in northeast US winter storms are rare. Over all the hourly observations presented here, heavy snow rates (> 2.5 mm hr^{-1}) occurred < 4% of the time. This analysis indicates that anecdotal evidence from case studies in the literature showing a strong relation between heavier snow and enhanced reflectivity features is not representative for a large sample size of 7606 hours, 264 storms, and 11 years. *Equating snow bands with heavy snow will usually lead to over prediction of hourly snowfall rates.* Our large sample size shows that 3 out of 4 times situations with feature area × time fractions > 0.5 have liquid equivalent snow rates < 2.5 mm hr^{-1}. More hours with heavy snow occurred associated with smaller feature areas (364 hours) as compared to larger feature areas (113 hours).

Since locally-enhanced reflectivity features are not particularly helpful at identifying regions of heavy snow rates, we calculate the area × time fraction for *all echo areas* to see if there are patterns present (Fig. 5.15). The patterns in this 2D distribution indicate that heavy snow (> 2.5 mm hr^{-1}) are more common when there is a large echo area × time fraction (i.e. there is a lot of echo surrounding the station for a longer duration). This suggests that it is more useful to focus on the duration of all echo over a location rather than the size, duration, and location of just the locally-enhanced reflectivity features for predicting where higher snowfall accumulations may occur. The distribution of snowfall rates has a strong skewness to low values, 75% of the time it is snowing at a rate no more than 1 mm hr^{-1}. So even if there is enhanced reflectivity feature area it is more likely associated with a low snow rate than a heavy snow rate.

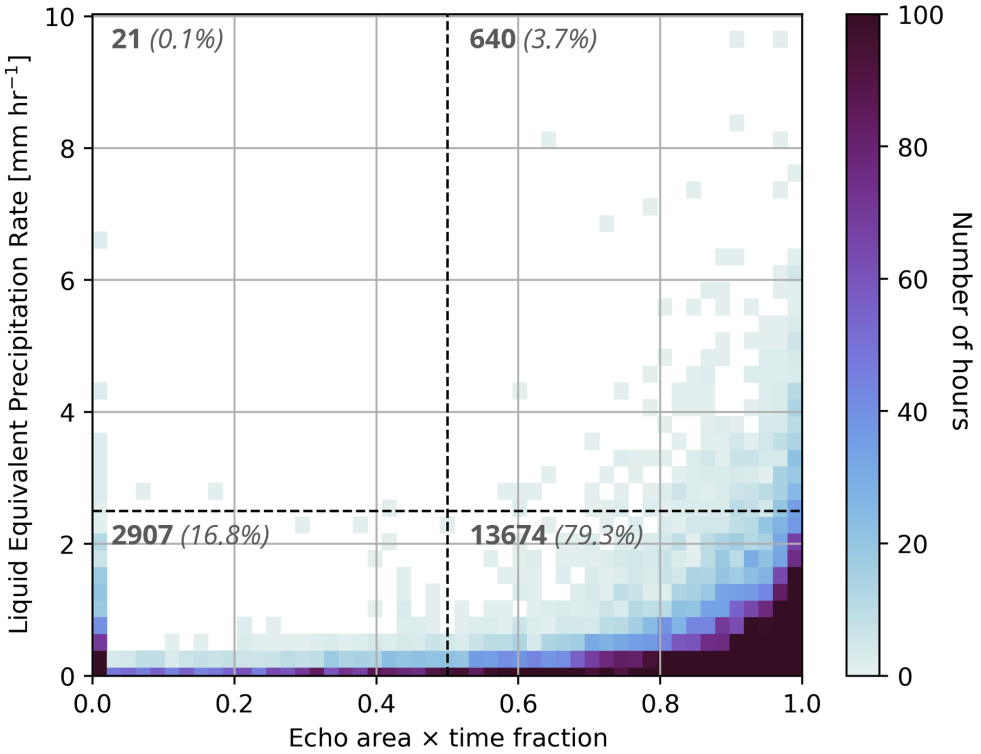

Figure 5.15: 2D distribution of all echo (background + faint features + strong features) area × time fraction versus liquid equivalent precipitation rate [mm hr^{-1}] for snow observations. Area × time fraction is calculated with a 25 km radius and observations are paired with a 0-hour lag. 0.5 area × time fraction is annotated with a vertical black dashed line and 2.5 mm hr^{-1} is annotated with a horizontal black dashed line. Bold annotated numbers indicate number of hours in each quadrant and italicized numbers indicate percent of total observations in each quadrant.

5.1.6 Complicating factors in relating observed radar reflectivity to surface snow rates

The lack of relationship between observed locally-enhanced reflectivity features and snow rates indicates that the radar observations above the surface are not necessarily consistent with snow rates observed at the surface. There are several factors that complicate the relationship between reflectivity and snowfall rate that are not present in the relationship between reflectivity and rain rate.

Changes in radar reflectivity do not necessarily translate to changes in ice mass. As is discussed in Chap. 1, processes such as aggregation can increase the reflectivity without increasing the mass per unit volume (Table 1.1). In addition, whereas the typical fall speeds of raindrops (2-8 m s^{-1}, depending on raindrop size) yield vertical column continuity of enhanced reflectivity features in rain, the slower fall speeds of snow (1 ± 0.5 m s^{-1}) do not. High spatial resolution aircraft radar data from winter storms indicates that snow rarely falls straight down to the surface. Falling snow particles can be blown sideways more than 50 km horizontally from the locations where they first achieve precipitation size near the top of the storm. Locally enhanced reflectivity features tend to be tilted and smeared by the wind shear (changes in the wind speed and direction with height) between echo top and the surface.

Vertical cross sections collected from radars aboard the ER-2 aircraft deployed during the NASA IMPACTS field campaign (McMurdie et al. 2022) illustrate typical vertical structures and horizontal wind profiles observed in winter storms (Figs. 5.16–5.21). There were 3 radars (4 frequencies total) that sampled storms during the campaign; EXRAD, HIWRAP (2 wavelengths), and CRS (see Table 5.1 for details). The examples we present here have a reflectivity panel from the radar with the longest wavelength that was available (usually EXRAD, and HIWRAP Ku-band if EXRAD not available) and velocity and spectrum width from the shortest wavelength that was available (usually CRS, and HIWRAP Ka-band if CRS not available). When available, VAD horizontal winds derived from the EXRAD scanning beam (Helms et al. 2020) are shown on the reflectivity cross sections and summarized with Contoured Frequency by Altitude Diagrams (CFADs; Yuter and Houze 1995).

Doppler spectrum width is a proxy for turbulence. To correct the spectrum width field to yield high quality data, we use equation 7 in Heymsfield et al. (1996) to isolate the spectrum width of the hydrometeors and remove the spectrum width broadening caused by the aircraft speed. In some cases, this correction causes the spectrum width numeric value to become ≤ 0 m s^{-1} (i.e. a nonphysical value; see Fig. 5.18c) which is ignored in the plotting as it represents signal below the noise floor.

The first example from 5 February 2020 in the Midwest illustrates several types of variations

Table 5.1: Band, frequency [GHz], sensitivity [dBZ] at 10 km (ER-2 radars)/1 km (KASPR), spatial resolution [m] at 10 km below the aircraft (ER-2 radars)/above the radar (KASPR), and citation for radars deployed on the ER-2 aircraft and at Stonybrook University deployed during NASA IMPACTS.

Radars	Band	Frequency	Sensitivity	Spatial Resolution	Reference
EXRAD *(precip. radar)*	X	9.6 GHz	-12 dBZ	679 m	Heymsfield et al. (1996)
HIWRAP *(precip. radar)*	Ku Ka	13.5 GHz 35.5 GHz	-10 dBZ -12 dBZ	672 m 288 m	Li et al. (2016)
CRS *(cloud radar)*	W	96 GHz	-30 dBZ	137 m	McLinden et al. (2021)
KASPR *(precip. radar)*	Ka	35.3 GHz	-40 dBZ	56 m	Oue et al. (2024)

in the reflectivity field in the vertical (Fig. 5.16). At the beginning of the transect, when the aircraft is travelling from the edge of the echo in the regional map (Northern Illinois; Fig. 5.16d) the vertical cross sections indicate that the echo aloft is not reaching the surface (0-40 km, 0-1 km altitude in Fig. 5.16a). At ∼90 km along flight track, there are regions where there is echo reaching the surface but "holes" in the echo aloft. Other regions along the cross section show consistent echo through the vertical column and indicate lots of wind shear illustrated by the wind barbs and bends in the local variations of the reflectivity field itself (i.e. 125-175 km in Fig. 5.16a). It is important to note that the cross sections are plotted in a 3:1 aspect ratio so vertical features that are tilted are even more tilted in reality (see triangle icons next to Fig. 5.16c for visualization). CFADs of the wind speed (Fig. 5.16e) and wind direction (Fig. 5.16f) along the track indicate considerable vertical wind shear. Horizontal wind speeds reach around 30 m s^{-1} at 5 km altitude near the top of the echo. The wind direction at 5 km altitude is roughly perpendicular to the direction the aircraft is travelling indicating that snow particles forming aloft will be transported out of the page by the wind as they descend to the surface (Fig. 5.16b, c).

The next example from 7 February 2020 shows a transect over New York (Fig. 5.17). In this example, the reflectivity is more uniform compared to the previous example (Fig. 5.17a). The aircraft is travelling westward from a region of higher reflectivity in central New York to a region of weaker reflectivity in western New York (Fig. 5.17a, d). This case was examined in Colle et al. (2023) for the lack of snow banding despite considerable frontogenesis present (values > 10 K $(100\ km)^{-1}$ $(3\ hr)^{-1}$). The CFADs of the wind speed and direction from the transect indicate speed shear and some directional shear (Fig. 5.17e,f). Similar to Fig. 5.16, the wind direction is roughly perpendicular to the direction the aircraft is flying, indicating that the particles forming aloft are advected away from the flight path – and hence the vertical plane of the cross-section

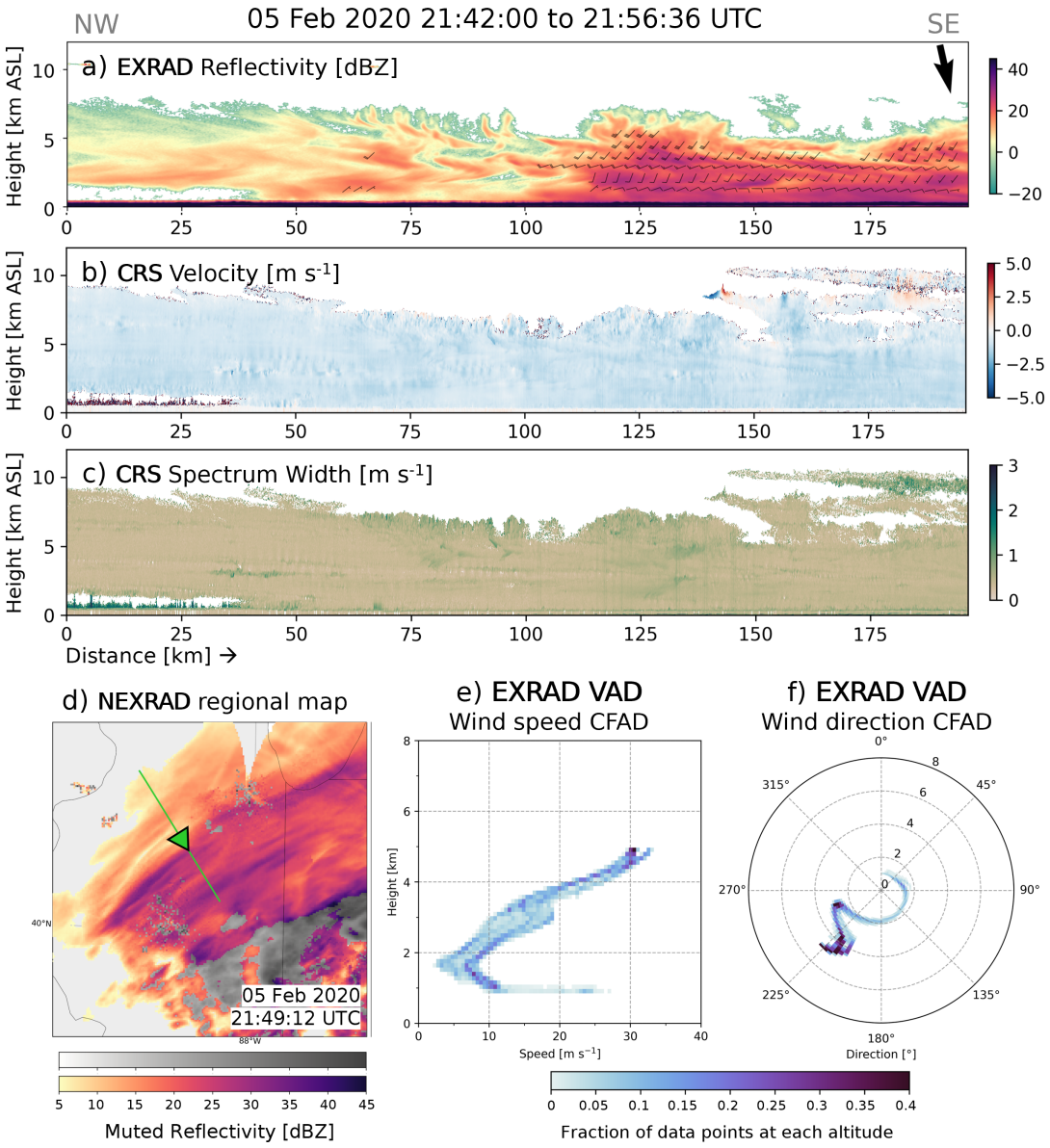

Figure 5.16: Vertical cross-section from 5 February 2020 21:42:04 to 21:56:44 UTC of (a) reflectivity [dBZ] from NASA EXRAD radar (nadir beam) and VAD winds derived from EXRAD radar (scanning beam), (b) velocity [m s^{-1}], and (c) spectrum width [m s^{-1}] from NASA CRS cloud radar. All vertical cross-sections are plotted with a 3:1 aspect ratio. Triangle icons next to (c) illustrate a 45° angle in a 1:1 and 3:1 aspect ratio. (d) Corresponding NEXRAD regional map of image muted reflectivity [dBZ] with ER-2 flight path in green, arrowhead denotes direction and location of aircraft at time of region map. CFADs of (e) wind speed and (f) wind direction of VAD winds in (a). Wind direction CFAD is plotted in polar coordinates where the angle represents the direction and each radius represents the altitude (0 km at the center). Black arrow in panel a indicates the compass direction of the aircraft during the transect.

– as they fall (Fig. 5.17).

The remaining examples do not have VAD horizontal wind data available. We include a panel of the feature detection field instead for context. An example from 23 January 2023 shows a case where the aircraft flew parallel to strong, banded features in Maine and New Hampshire (Fig. 5.18e). The reflectivity cross section shows features, known as ice streamers that are tilted as they approach the surface. The top of the ice streamers are likely generating cells formed from overturning circulations at cloud top (Fig. 5.18a). The velocity and spectrum width cross sections indicate some overturning circulations near echo top between 150-200 km along the flight track (Fig. 5.18b,c). Additionally, there are local enhancements (tilted blue lines in b and corresponding higher spectral width in c) within the tilted ice streamers as particles originating in the generating cells descend to the surface.

Figure 5.19 shows an example from a 300 km long flight track that flew over some faint enhanced reflectivity features in the Gulf of Maine. The regional radar reflectivity indicates that this storm had weaker and more patchy echo compared to the previous examples (Fig. 5.19d). The radar cross sections show shallower echo tops (∼5 km altitude) compared to the previous examples. Between 125 km and 175 km along flight track, enhanced reflectivity features tilt to the right and then to the left. There are weak echo holes throughout the cross-section.

Figure 5.20 shows an example from 17 February 2022 when the aircraft sampled a faint, banded feature over Lake Michigan (200-215 km along flight track). The flight track began over central Indiana (southeast) over surface rainfall which transitioned to surface snow at ∼48 km along the flight track. This surface rain portion of the flight track is depicted as an image muted area in gray in Fig. 5.20d and has a radar bright band, and high Doppler velocities and spectral width in the rain layer between 0-48 km (Fig. 5.20abc). Along the flight track within the snow layer between 6 and 2.5 km altitude, locally enhanced reflectivity features in snow tend to tilt to the right (towards northwest). At the northwest end of the flight track when the aircraft approaches the faint enhanced feature in the map (Fig. 5.20e) , there is a layer of locally-enhanced reflectivity at ∼2.5 km altitude between 150-250 km (Fig. 5.20a) with weaker to no echo below it. It is possible that the faint feature in the map manifests as the scanning radar intersects part of this elevated region of enhanced reflectivity.

Figure 5.21 shows an example from a 400+ km long flight over southern New York and New Jersey that travels parallel to several faint features. The reflectivity cross section shows fairly shallow echo (< 5 km) that has tilted ice streamers reaching from near echo top to near the surface (Fig. 5.21a). Following individual streamers along the plane of the cross-section there is a typical horizontal displacement of about 30-40 km between near echo top and the surface. Doppler velocity (Fig. 5.21b) indicates a layer at ∼2.5 km altitude between ∼160 to 275 km along flight track with an undulating pattern which may indicate Kelvin-Helmholtz waves. There is

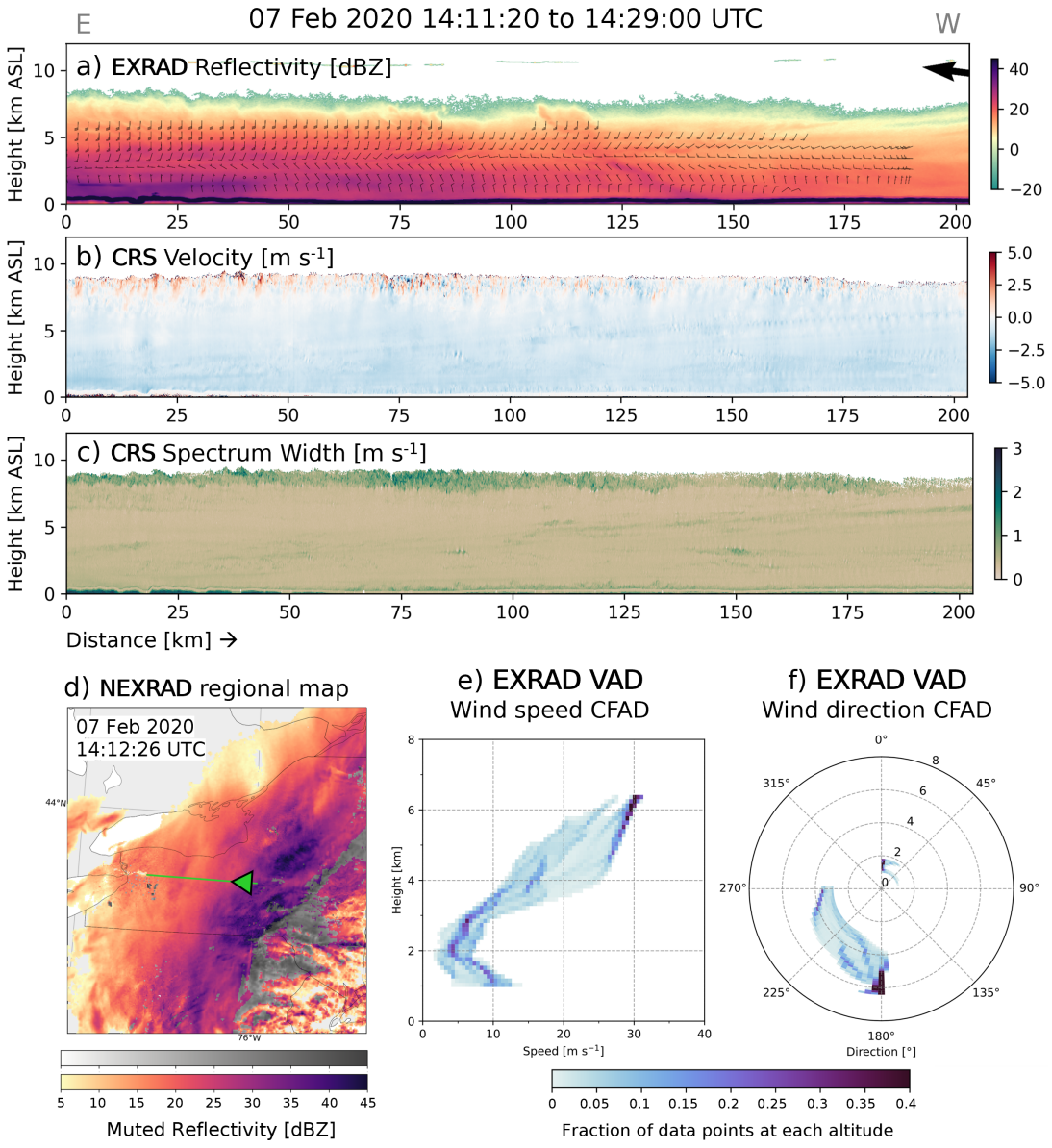

Figure 5.17: Vertical cross-section from 7 February 2020 14:11:20 to 14:29:00 UTC of (a) reflectivity [dBZ] from NASA EXRAD radar (nadir beam) and VAD winds derived from EXRAD radar (scanning beam), (b) velocity [m s^{-1}], and (c) spectrum width [m s^{-1}] from NASA CRS cloud radar. All vertical cross-sections are plotted with a 3:1 aspect ratio. Triangle icons next to (c) illustrate a 45° angle in a 1:1 and 3:1 aspect ratio. (d) Corresponding NEXRAD regional map of image muted reflectivity [dBZ] with ER-2 flight path in green, arrowhead denotes direction and location of aircraft at time of region map. CFADs of (e) wind speed and (f) wind direction of VAD winds in (a). Wind direction CFAD is plotted in polar coordinates where the angle represents the direction and each radius represents the altitude (0 km at the center). Black arrow in panel a indicates the compass direction of the aircraft during the transect.

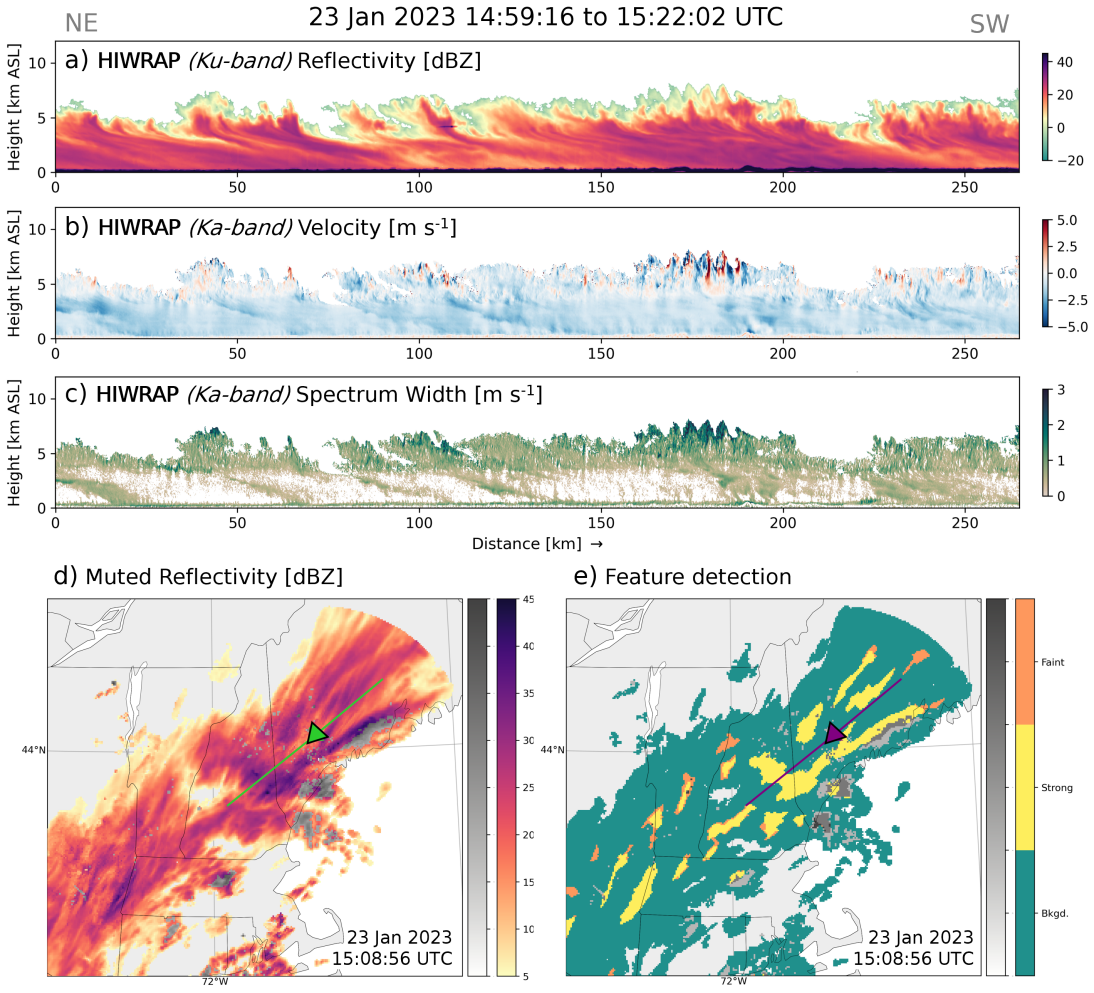

Figure 5.18: Vertical cross-section from 23 January 2023 14:59:16 to 15:22:02 UTC of (a) reflectivity [dBZ] from NASA HIWRAP (Ku-band) radar, (b) velocity [m s^{-1}], and (c) spectrum width [m s^{-1}] from NASA HIWRAP (Ka-band) radar. All vertical cross-sections are plotted with a 3:1 aspect ratio. Triangle icons next to (c) illustrate a 45° angle in a 1:1 and 3:1 aspect ratio. Corresponding NEXRAD regional map of (d) image muted reflectivity [dBZ] with ER-2 flight path in green and (e) feature detection classification with ER-2 flight path in purple, arrowhead denotes direction and location of aircraft at time of region map. Black arrow in panel a indicates the compass direction of the aircraft during the transect.

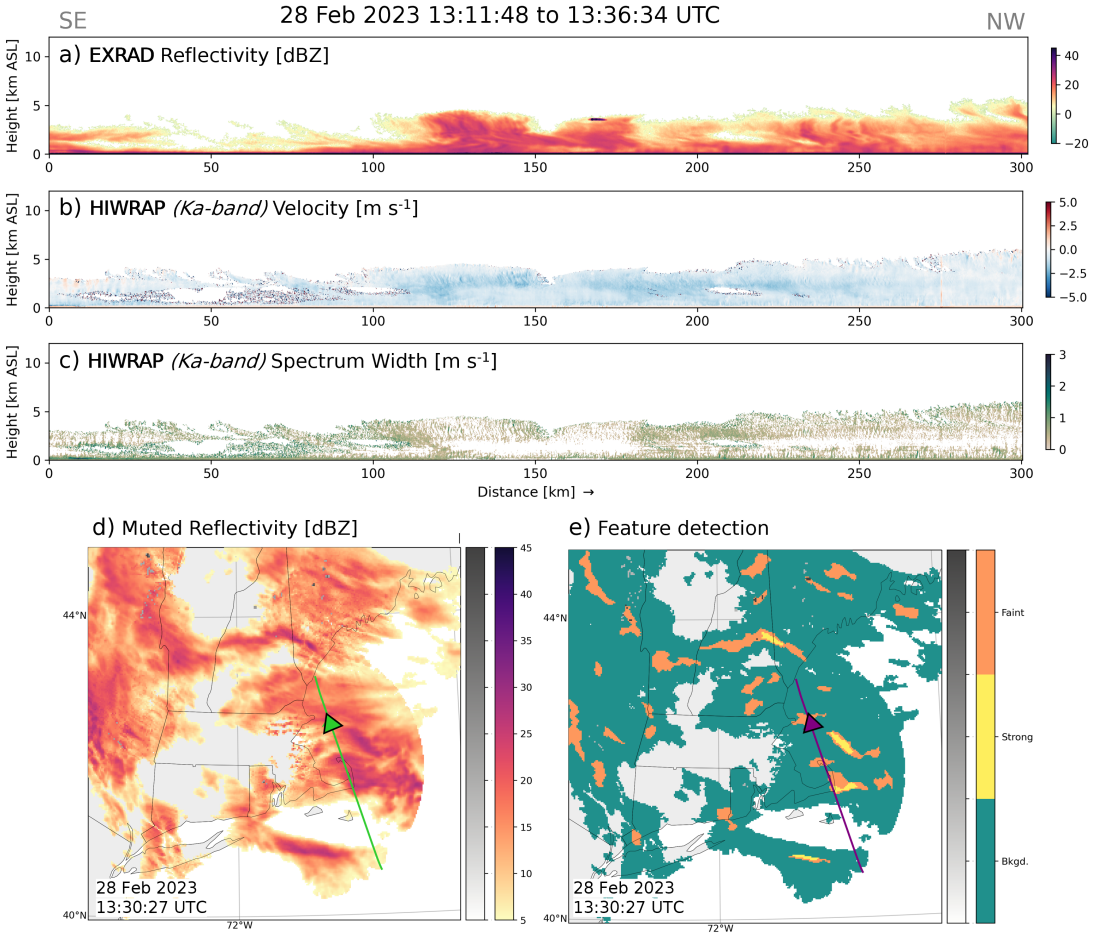

Figure 5.19: Vertical cross-section from 28 February 2023 13:11:48 to 13:36:34 UTC of (a) reflectivity [dBZ] from NASA EXRAD radar (nadir beam), (b) velocity [m s^{-1}], and (c) spectrum width [m s^{-1}] from NASA HIWRAP (Ka-band) radar. All vertical cross-sections are plotted with a 3:1 aspect ratio. Triangle icons next to (c) illustrate a 45° angle in a 1:1 and 3:1 aspect ratio. Corresponding NEXRAD regional map of (d) image muted reflectivity [dBZ] with ER-2 flight path in green and (e) feature detection classification with ER-2 flight path in purple, arrowhead denotes direction and location of aircraft at time of region map. Black arrow in panel a indicates the compass direction of the aircraft during the transect.

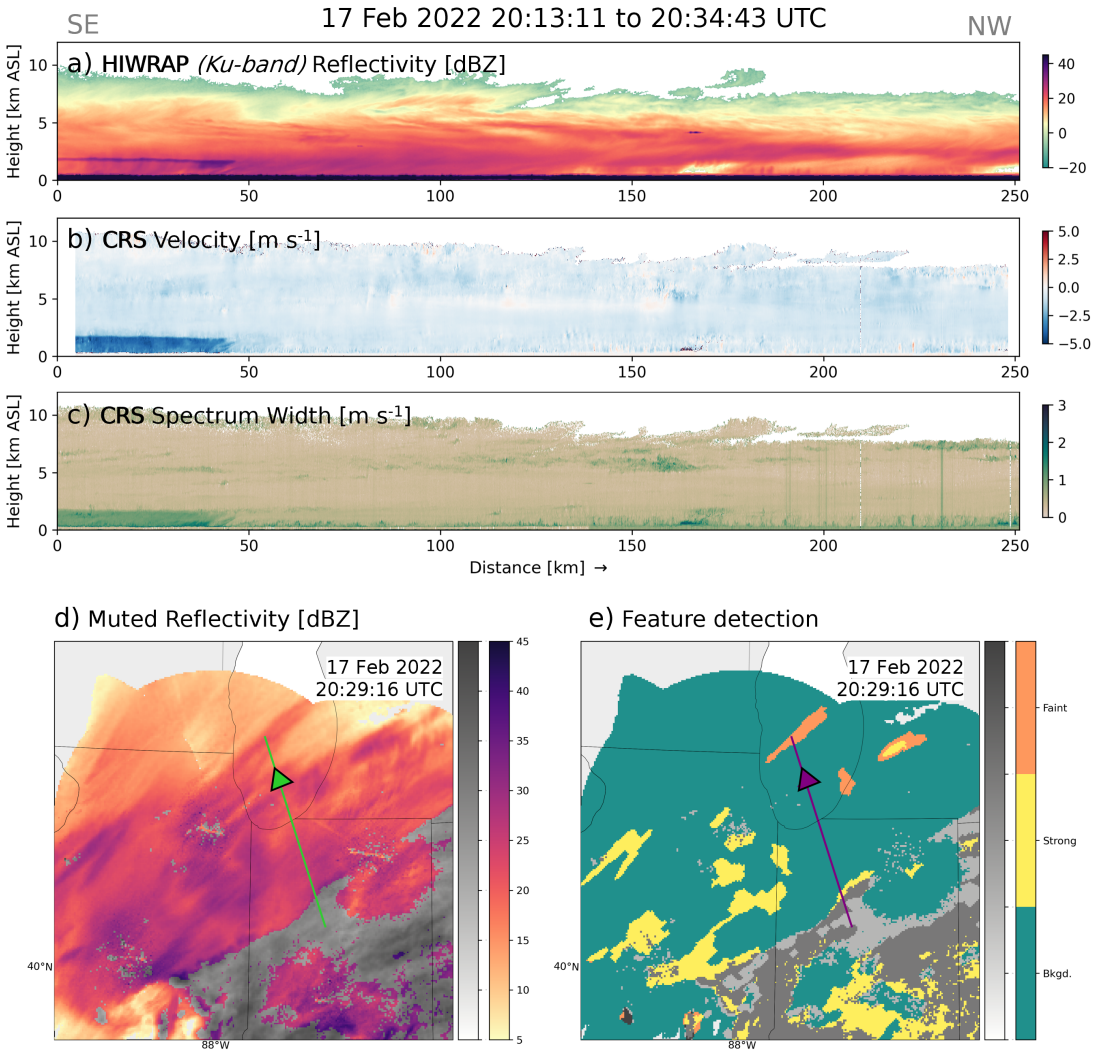

Figure 5.20: Vertical cross-section from 17 February 2022 20:13:11 to 20:34:43 UTC of (a) reflectivity [dBZ] from NASA HIWRAP (Ku-band) radar, (b) velocity [m s^{-1}], and (c) spectrum width [m s^{-1}] from NASA CRS cloud radar. All vertical cross-sections are plotted with a 3:1 aspect ratio. Triangle icons next to (c) illustrate a 45° angle in a 1:1 and 3:1 aspect ratio. Corresponding NEXRAD regional map of (d) image muted reflectivity [dBZ] with ER-2 flight path in green and (e) feature detection classification with ER-2 flight path in purple, arrowhead denotes direction and location of aircraft at time of region map. Black arrow in panel a indicates the compass direction of the aircraft during the transect.

no obvious wave-like signatures in the reflectivity field at the same location.

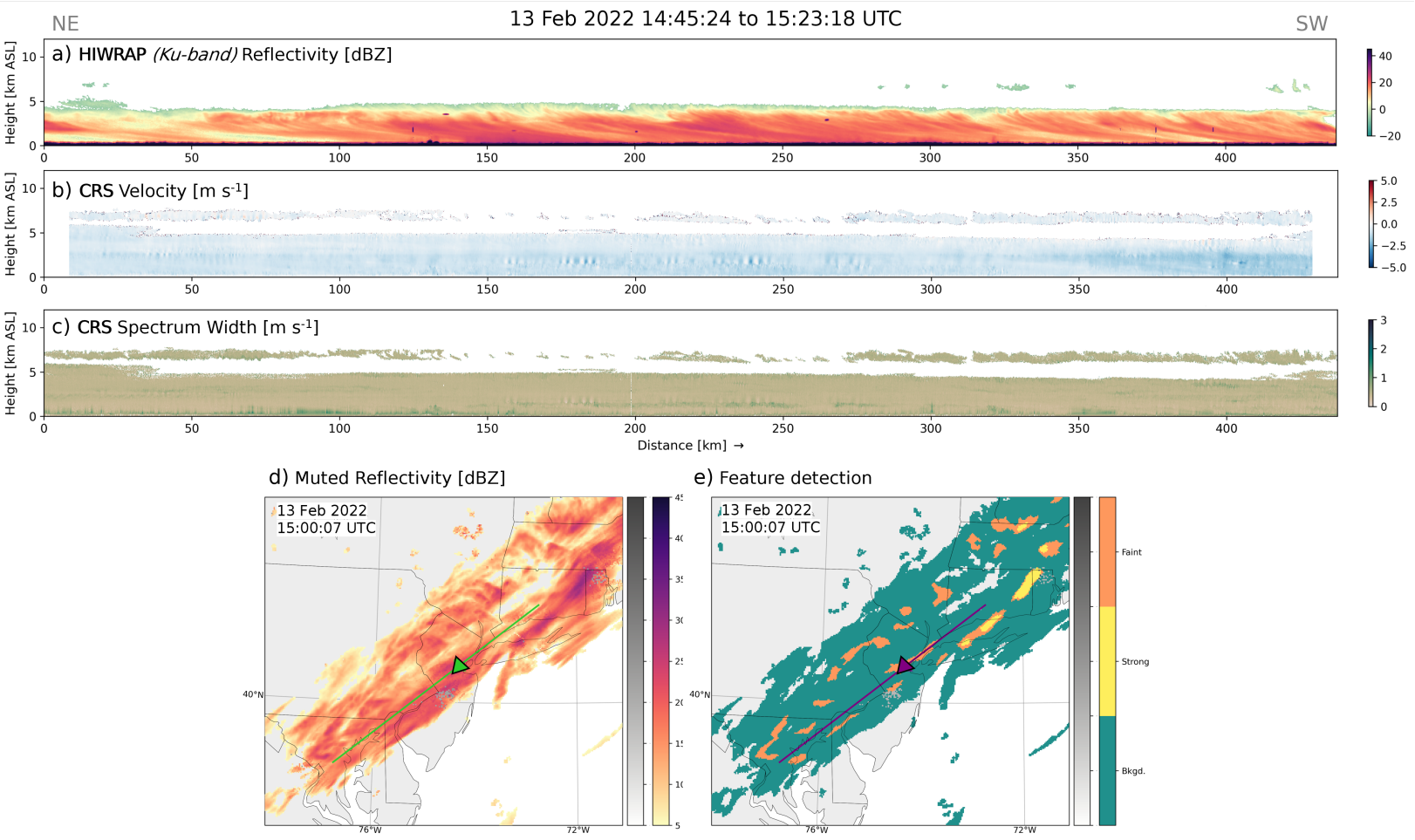
NE
13 Feb 2022 14:45:24 to 15:23:18 UTC
SW
a) HIWRAP (Ku-band) Reflectivity [dBZ]
b) CRS Velocity [m s-1]
c) CRS Spectrum Width [m s-1]
Height [km ASL]
Distance [km] →
d) Muted Reflectivity [dBZ]
e) Feature detection
13 Feb 2022
15:00:07 UTC
Faint
Strong
Bkgd.
40°N
76°W
72°W

Figure 5.21: Vertical cross-section from 13 February 2022 14:45:24 to 15:23:18 UTC of (a) reflectivity [dBZ] from NASA HIWRAP (Ku-band) radar, (b) velocity [m s^{-1}], and (c) spectrum width [m s^{-1}] from NASA CRS cloud radar. All vertical cross-sections are plotted with a 3:1 aspect ratio. Triangle icons next to (c) illustrate a 45° angle in a 1:1 and 3:1 aspect ratio. Corresponding NEXRAD regional map of (d) image muted reflectivity [dBZ] with ER-2 flight path in green and (e) feature detection classification with ER-2 flight path in purple, arrowhead denotes direction and location of aircraft at time of region map. Black arrow in panel a indicates the compass direction of the aircraft during the transect.

In addition to the vertical cross sections from NASA IMPACTS, we also use range-height indicator (RHI) scans from the Ka-band (35 GHz) scanning fully polarimetric radar (KASPR) located at Stonybrook University to illustrate vertical features in a winter storm (Figs. 5.22 and 5.23). The data from the ground-based KASPR radar has finer vertical and horizontal spatial resolution than the ER-2 airborne radar data (Table 5.1). Unlike the airborne radars, which are nadir pointing, the RHIs scan up and over the radar such that the azimuth angle of the radar beams within the RHI varies from 15° elevation angle up to vertically pointing right over the radar and then back down to 15° elevation angle at the other horizon. When the radar beam is vertical or nearly vertical, the measured values of Doppler velocity and spectral width combine vertical air motions with precipitation particle fall speeds. When the radar beam is closer to horizontal, the measured motions are more indicative of the horizontal wind.

The effect of the changing component of the wind that is sampled as the radar beam elevation angle changes is particularly noticeable in the RHIs of Doppler velocity data (Fig. 5.22b and 5.23b). Plotted velocity values in a given layer tend to be strongest at the left and right edges of the RHI where the beam is more horizontal and peter out as the beam becomes more vertical near the center of the RHI plot. Whereas in the ER-2 radar vertically pointing data the Doppler velocity values were plotted with a range from -5 to 5 m s^{-1}, in these RHI plots, which are dominated by strong horizontal winds, the range plotted is -45 to 45 m s^{-1}. In the RHI plots, layers with low values of Doppler velocity indicate that the horizontal wind direction is close to perpendicular to the beam (i.e. in or out of the plane of the cross-section). A similar but less dramatic impact of beam angle on the measurements is apparent in the RHI spectral width plots. Although turbulence is usually close to isotropic, the combination of the air motion velocity spread with the strong signal from the often narrower precipitation fall speed spread tends to reduce the net spectral width magnitudes when the beam is pointed nearly vertical.

We feature two examples from 1-2 February 2022 when KASPR scanned fast update RHIs through a winter storm over 40 hours. In the first example at 1 February 2022 1558 UTC, the spectrum width is enhanced at echo top associated with overturning circulations (Fig. 5.22a). Other narrow layers of enhanced spectrum width are present at several altitudes including close to the surface (Fig. 5.22a). The Doppler velocity field helps to illustrate the horizontal

winds and how they vary with height (Fig. 5.22b). Near cloud top the winds are left to right, corresponding to a wind with a South component (wind coming from the south). In the layer between 2.3 and 3 km AGL the magnitude of the velocity is near zero which indicates the wind direction is pointing perpendicular to the radar beam. Between the surface and 1 km altitude there is shift in the wind direction to a wind with a North component illustrated by the change in sign of the Doppler velocity. The reflectivity field shows a lot of detail, including ice streamers that manifest from the overturning circulations near echo top (Fig. 5.22c). The ice streamer features become tilted and smeared on the way to the surface, likely due to the distinct layers in the wind profile illustrated in the Doppler velocity field. In this example, the cross sections are plotted in a 1:1 aspect ratio so the tilt of the features is shown as it occurs in reality. As the snow particles within the enhanced reflectivity features descend in the storm they move much faster sideways than they do vertically. Unless the horizontal winds are very weak, snow cannot fall "straight" down in a column. It is also important to note that the precipitation particles are not all falling within the plane of the RHI. In particular, reflectivity values at altitudes with layers of near zero Doppler velocity are potentially either moving in or out perpendicular to the cross-section. Whenever the wind direction changes between layers, the trajectories of individual precipitation particles turn with the wind, yielding complex 3D trajectories between their origination near cloud top and the surface.

In the second example a few hours later at 1928 UTC, the echo is slightly shallower overall and the reflectivity field is more variable near cloud top varying from close to minimum detectable echo at -5 dBZ to close to 25 dBZ (Fig. 5.23c). There is some locally higher spectral width and likely turbulence close to 5 km altitude near echo top at the location of generating cells near -24 to -26 km and directly above the radar near 0 km (Fig. 5.23a). There is a discontinuity in the direction of tilt of ice streamers within the reflectivity field at about 3 km altitude from toward the right (North) to toward the left (South) corresponding to the wind shift observed in the Doppler velocity field (Fig. 5.23b). Similar to at 1558 UTC, the wind also sharply shifts direction to a North wind at about 1 km altitude above the surface.

The aircraft radar cross sections from the NASA IMPACTS campaign and RHI scans from KASPR radar illustrate how features in the reflectivity field are often tilted and smeared in winter storms. For winter storms with snow, there is a general lack of vertical column continuity of enhanced reflectivity features. The lack of vertical column continuity of enhanced reflectivity aloft to the surface complicates the interpretation of reflectivity from scanning radar and provides a likely explanation for why we are not seeing a strong relationship between enhanced reflectivity aloft and snow rates at the surface.

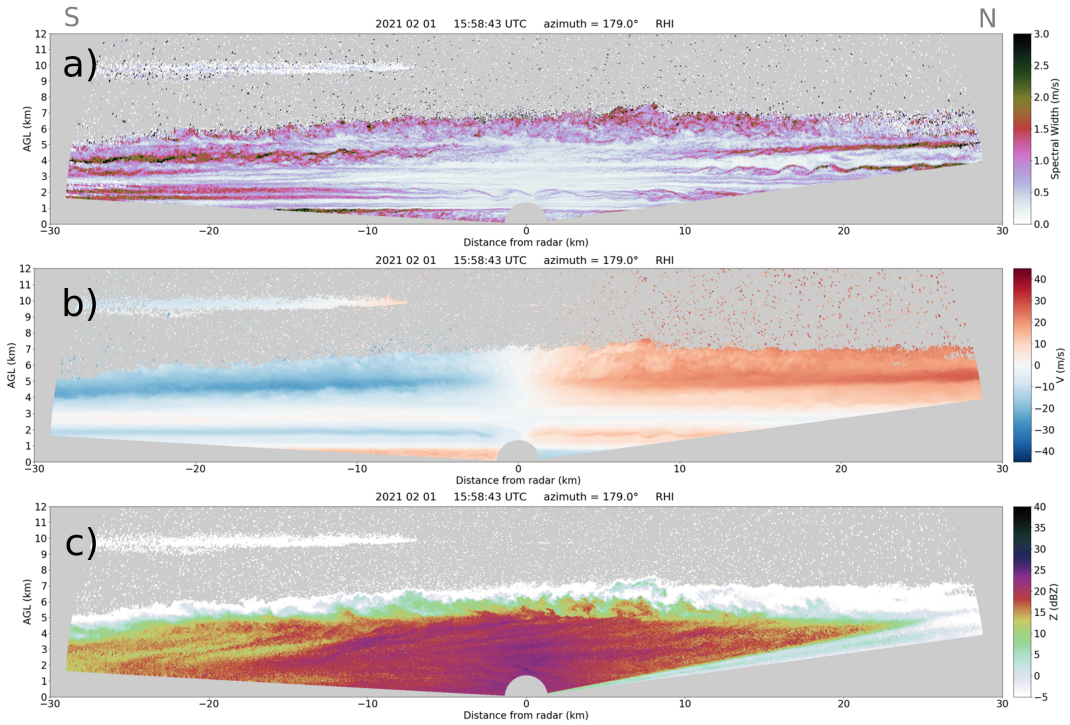

Figure 5.22: RHIs scanned up and over the radar (at 0 km on x-axis) of (a) Spectrum Width [m s^{-1}], (b) Doppler Velocity [m s^{-1}], and (c) Reflectivity [dBZ] from the KASPR radar at Stonybrook University at 15:58:42 UTC on 1 February 2021. Radar beam is partially blocked near edge of scan on right side. Plotted in a 1:1 aspect ratio.

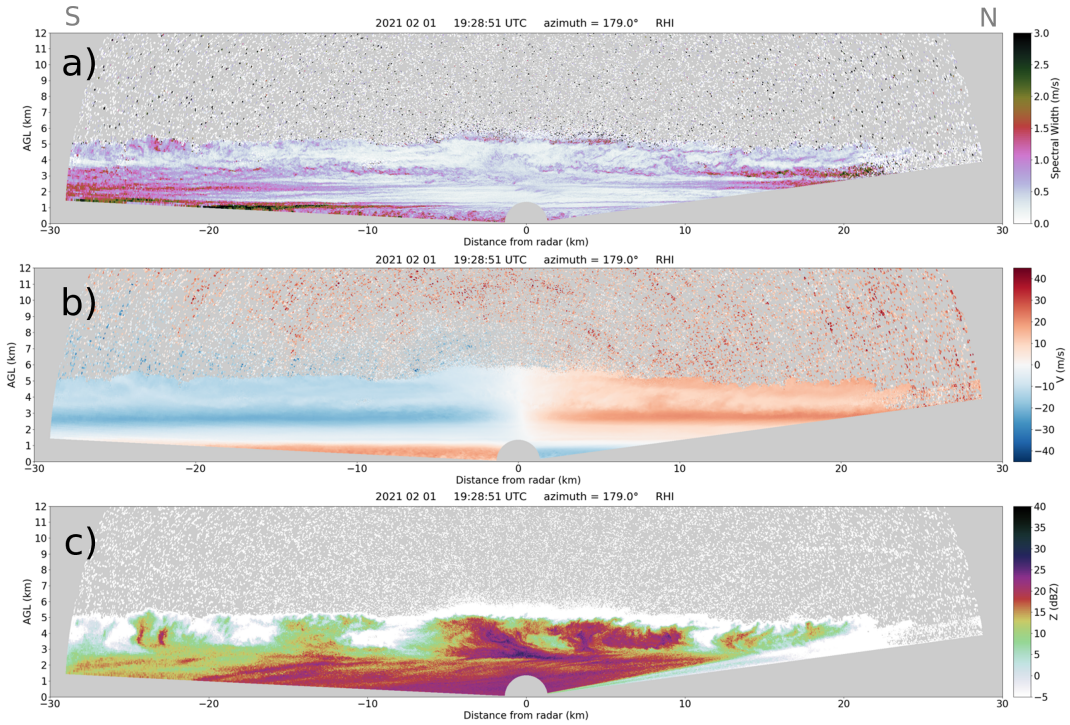

Figure 5.23: RHIs scanned up and over the radar (at 0 km on x-axis) of (a) Spectrum Width [m s^{-1}], (b) Doppler Velocity [m s^{-1}], and (c) Reflectivity [dBZ] from the KASPR radar at Stonybrook University at 19:28:51 UTC on 1 February 2021. Radar beam is partially blocked near edge of scan on right side. Plotted in a 1:1 aspect ratio.

5.2 Velocity waves

In this section we explore the relationship between velocity waves and surface snowfall rates and determine if there is any evidence that velocity waves are associated with heavier snowfall rates or enhanced reflectivity features.

To test the relationship between the presence of velocity waves and the surface snowfall rate, we pair the hourly wave classifications described in Sec. 2.2.5 with the hourly liquid equivalent precipitation rates described in Sec. 2.3. We combine YES and MAYBE observations into a single category and compare the distributions of precipitation rate. Figure 5.24 presents the precipitation rates for each category paired with a 0-hour lag as a scatter plot. Each precipitation rate observation is jittered from the category center so the overlapping points are more easily visible. For the remainder of the analysis we consider the observations from NYC and Massachusetts together. Distributions of precipitation rate for each classification are presented as histograms with a probability density function (Fig. 5.25). Both Fig. 5.24 and 5.25 show that there are very few YES and MAYBE observations (191 hours) compared to NO observations (4105 hours). It is difficult to deduce any sort of relationship from the scatter plot (Fig. 5.24), however, the probability density functions in Fig. 5.25 indicate the precipitation rate distribution is slightly skewed to higher rates for the YES + MAYBE category.

As in Sec. 5.1.4, we test the robustness of our results to the time lag that is used to pair the observations together. The number of hours for each category and each time lag is summarized in Table 5.2. Probability density functions for each category and time lag are shown in Fig. 5.26 and a summary of the distributions is presented in Table 5.3. For hours with NO waves, the distribution is almost identical for all time lags (Fig. 5.26b) and the 25th, 50th, and 75th percentile are identical (Table 5.3). For times with waves (YES + MAYBE) the distribution for 1- and 2-hour time lags is shifted to lower values compared to the 0-hour lag (also described with the median values in Table 5.3). For all times, the means and medians for the times with waves (YES + MAYBE) are higher than the means and medians for the times without waves (NO) [Table 5.3]. This suggests that times and locations with velocity waves have a slightly higher precipitation rates than times without waves. To test the significance of these differences, we use permutation tests, described in the next section.

Table 5.2: Number of observations for each category.

	YES + MAYBE	**NO**	**Total**
0-hour lag	191	4105	4296
1-hour lag	178	4026	4204
2-hour lag	151	3947	4098

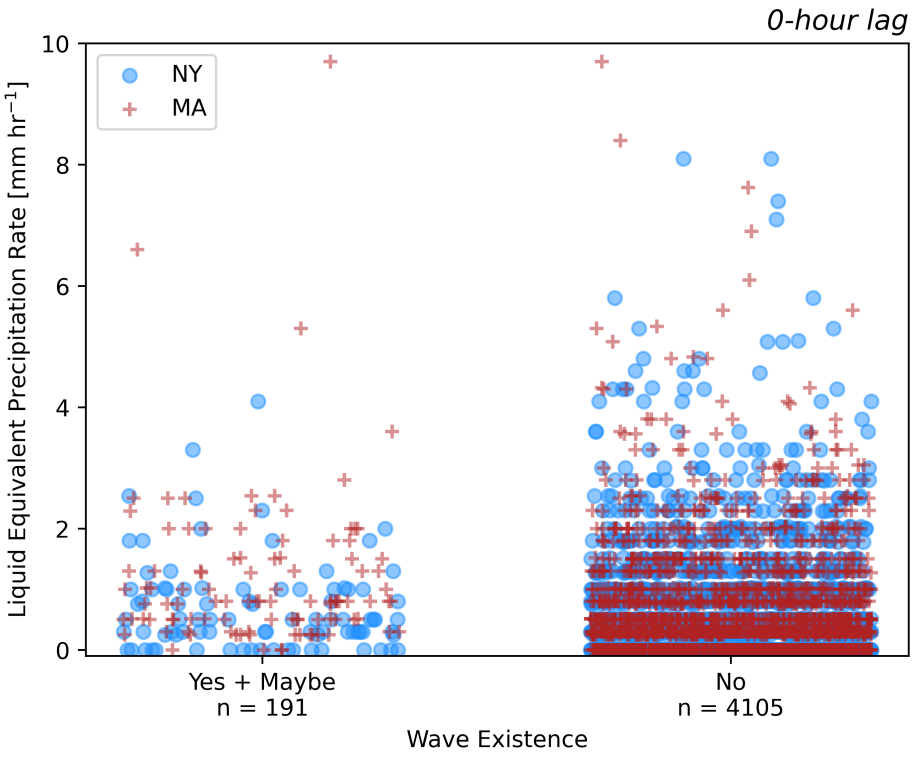

Figure 5.24: Joint occurrence of Doppler velocity waves and snow rates in the same hour. Plot of liquid equivalent precipitation rate [mm hr^{-1}] for times with YES + MAYBE waves and NO waves. Points are "jittered" to limit overlap and colored by the region (New York City metro area - blue, Massachusetts - red).

5.2.1 Permutation tests

To determine if the differences in the distributions of precipitation rates when waves are and are not present are statistically different, we use permutation tests (also known as Monte Carlo permutation tests; LaFleur and Greevy 2009; Holt and Sullivan 2023; Good 2013). Permutation tests are a form of resampling and are more general than other types of significance tests since they do not assume a particular distribution (Good 2013).

The null hypothesis is that the precipitation rate distributions when waves are and are not present are not statistically different (i.e. the distribution of precipitation rates when waves are present could be a random sample of the entire distribution). To perform the testing, we randomly sample 191 liquid equivalent precipitation rates from the entire dataset of 4296 points and calculate the median and mean of these 191 sampled points. We randomly sample 191 points from the entire distribution as this is the number of hours when waves are present for a 0-hour lag.

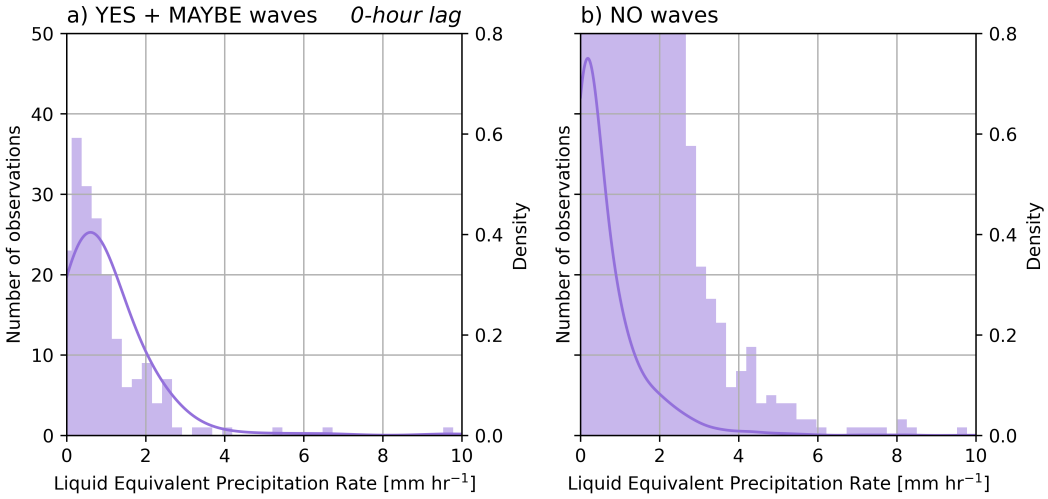

Figure 5.25: Distributions of snow rates during periods with and without velocity waves. Histograms of liquid equivalent precipitation rate [mm hr^{-1}] for times with (a) YES + MAYBE waves and (b) NO waves. Curve on each plot represents the probability density function.

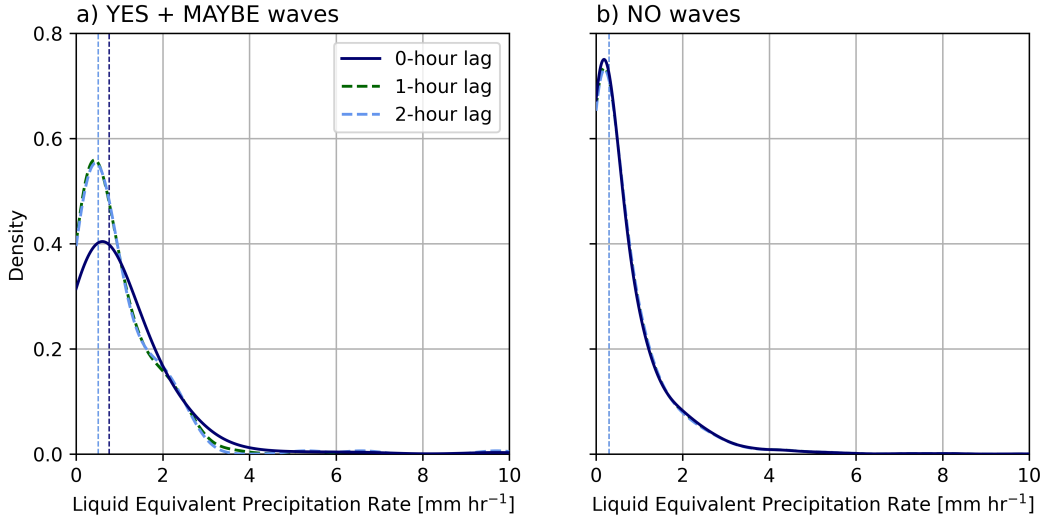

Figure 5.26: Sensitivity of velocity wave occurrence and snow rate distributions by time lag. Probability density functions of liquid equivalent precipitation rate [mm hr^{-1}] for times with (a) YES + MAYBE waves and (b) NO waves. Curves are colored by the time lag. Vertical dashed lines annotate the median values.

Table 5.3: 25th, 50th, 75th percentiles, and mean values for liquid water equivalent precipitation rate distributions for YES + MAYBE and NO waves and for 0-, 1-, and 2-hour time lags. Bottom panel is the 95th percentile of median and mean values from permutation tests (see also Fig. 5.27). Units are mm hr^{-1}.

	YES + MAYBE				**NO**			
	25th	50th	Mean	75th	25th	50th	Mean	75th
0-hour lag	0.3	0.76	1.09	1.3	0	0.3	0.67	0.8
1-hour lag	0.3	0.51	0.95	1.29	0	0.3	0.68	0.8
2-hour lag	0.3	0.51	0.94	1.29	0	0.3	0.67	0.8

	95th percentile of median and mean precip. rates from permutation tests	
	Median	Mean
0-hour lag	0.5	0.94
1-hour lag	0.5	0.937
2-hour lag	0.5	0.951

We repeat the process 10,000 times and then compare the 95th percentile of the medians and means of the randomly sampled precipitation rates to the median and mean of the precipitation rate during time when waves are present. When the median or mean of the distribution when waves are present is greater than the 95th percentile, the distribution is considered unlikely to be from the same distribution as a whole and is interpreted to be not random.

Distributions of the sampled median and mean values for 0-, 1-, and 2-hour lags are shown in Fig. 5.27 and summarized in the bottom half of Table 5.3. For the 0-hour lag, the median (0.76 mm hr^{-1}) and mean (1.09 mm hr^{-1}) of the actual YES+MAYBE distribution are both larger than the 95th percentile of medians (0.5 mm hr^{-1}) and means (0.94 mm hr^{-1}) of the randomly sampled distributions. This indicates that the there is a less than 5% chance that the actual values could be achieved at random. The median and mean for the 1-hour lag and the median for the 2-hour lag barely exceed the criteria (actual median 0.51 mm hr^{-1} and random median 0.5 mm hr^{-1} for both the 1-hour and 2-hour lags).

The results from the permutation tests indicate that for observations paired with a 0-hour lag, times with velocity waves are associated with slightly higher snowfall rates than times without waves. Since pairs of velocity waves are associated with convergence and divergence (Miller et al. 2022), if the ice mass growth in upward moving air (by riming and/or vapor deposition) is not reversed in the downward moving air (by sublimation) then there is net increase in ice mass. To investigate this finding further, future work is needed that is beyond the scope of this thesis. It is possible that the higher snowfall rates in times with waves may be related to an association between velocity waves and frontogenesis. Based on previous work,

waves are often found ahead of a warm front or in the vicinity of an occluded front where stronger frontogenesis can occur. It is possible that the slightly higher snowfall rates are related to upward motions associated with frontogenesis rather than physical processes in the waves independent of frontogenesis.

5.2.2 Relationship to enhanced reflectivity features

In addition to testing the relationship between velocity waves and precipitation rate, we also wanted to investigate any potential relationship between velocity waves and enhanced reflectivity feature area. Hoban (2016) hypothesized that velocity waves may be a mechanism for forming multibands. If this hypothesis is true then we might expect to see higher feature area during times when velocity waves occur. Figure 5.28 shows 2D distributions of feature area × time fraction versus liquid equivalent precipitation rate for times with and without waves. This figure highlights the few observations we have with waves (191) compared to the observations we have without waves (4105). Although we looked at 264 storms over 11 years in both the NY and MA areas, there were *only 8 observations with velocity waves and feature area × time fraction > 0.5*. It is difficult to make any conclusions with so few observations, although the information we do have indicates that velocity waves are likely not frequently related to locally-enhanced reflectivity features.

5.3 Summary

In this chapter we examined the relationship between radar-observed characteristics of winter storms and surface snowfall precipitation rates. Specifically, we looked at the locally-enhanced reflectivity features surrounding ASOS stations and their relationship with surface snow rates. We also examined potential associations between velocity waves and surface snow rates.

When comparing the feature area × time fraction from the feature detection field in the regional radar maps to the liquid equivalent precipitation rate from the ASOS stations, we found little to no relationship between feature area and precipitation rate. This indicates that locally-enhanced reflectivity features, i.e. snow bands, are not good indicators of heavy hourly snow rates at the surface. Rather, the duration of any radar echo over the ASOS station is more informative of hourly snowfall rates. We found that our results were not sensitive to the radius over which we calculate area × time fraction, the time lag that we paired the observations with, the average height of the radar beam above the ASOS station, the amount of mixed precipitation in the region, or the time period the statistics were accumulated over.

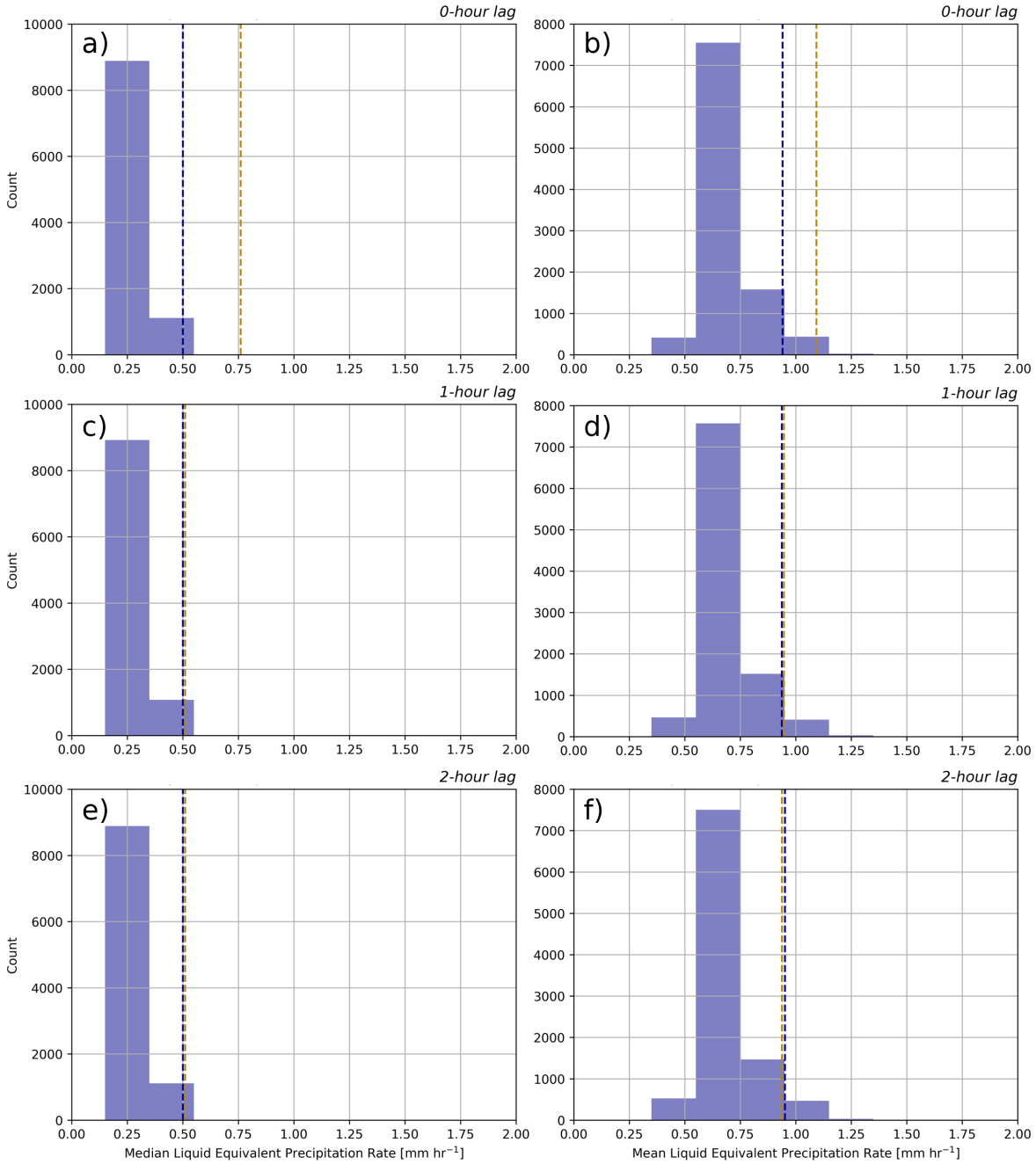

Figure 5.27: Median and mean snow rates in subsets of 191 out of 4396 samples randomly chosen over 10,000 permutation tests. Histograms of (a, c, e) median and (b, d, f) mean liquid equivalent precipitation rate [mm hr^{-1}] for (a, b) 0-hour lag, (c, d) 1-hour lag, and (e, f) 2-hour lag. Dark blue vertical dashed line indicates the 95th percentile of the distribution and Gold vertical dashed line indicates the median or mean precipitation rate of the YES waves distribution.

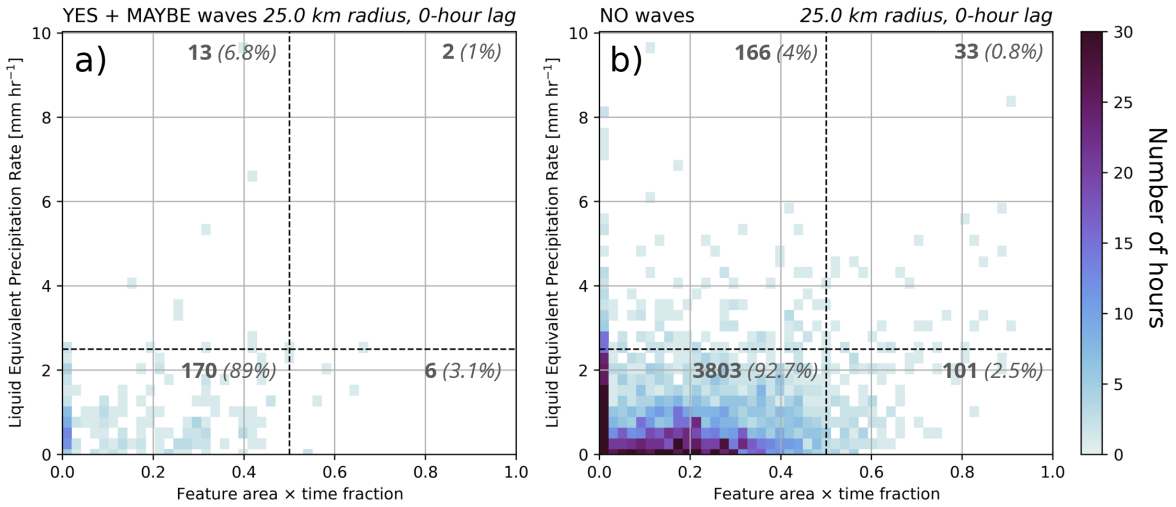

Figure 5.28: Velocity wave occurrence and 2D distribution of feature area × time fraction versus liquid equivalent precipitation rate [mm hr^{-1}] for snow observations. Area × time fraction calculated with a 25 km radius and and observations are paired with the following wave classifications (a) YES + MAYBE, (b) NO. 0.5 area × time fraction is annotated with a vertical black dashed line and 2.5 mm hr^{-1} is annotated with a horizontal black dashed line. Bold annotated numbers indicate number of hours in each quadrant and italicized numbers indicate percent of total observations in each quadrant.

There is considerable uncertainty in relating remote sensing observations within snow to surface snowfall rates (Fujiyoshi et al. 1990; Rasmussen et al. 2003). Our results showing that duration of *any* radar echo is more relevant than the presence of snow bands suggest that it may be better to use area-threshold methods (e.g., Krajewski et al. 1992) rather than pixel by pixel retrievals to estimate snowfall accumulations.

To determine the relationship between velocity waves and snow rate, we compared distributions of liquid equivalent precipitation rate during times with waves (hours classified as YES or MAYBE) and without waves (hours classified as NO). We found that snow rates were slightly higher during times with velocity waves and that this result is unlikely to be by chance at 0-hour lag. There were too few observations with velocity and enhanced reflectivity feature area × time fraction > 0.5 to make any conclusions.

The results here argue that case studies that suggested a strong relationship between snow bands and surface snow rates were not representative of a large sample size. Operational forecasters are better off looking for areas of strong frontogenesis and duration of snow echo since focusing on where snow bands and velocity waves are occurring does not seem to add any skill.

Chapter 6

Variations in snowfall rates with storm structure and evolution

Previous work has shown that primary snow bands are associated with strong frontogenesis (Novak et al. 2004; Ganetis et al. 2018). Frontogenesis is typically observed ahead of the warm front and in the northeast and northwest quadrants relative to the low pressure center, while frontolysis is typically found behind the cold front (Fig. 6.1). Han et al. (2007) created the conceptual diagram in Fig. 6.1 after analyzing the structure and associated frontal circulations of 2 extratropical cyclones using numerical simulations. Colle et al. (2014) observed microphysical properties at Stonybrook University in the context of low pressure centers for 12 northeast US winter storms. They found that riming intensity was dependent on the location relative to the cyclone and the associated patterns of temperature and vertical motion. Their work showed moderate and heavily rimed snow particles tend to occur in the northwest quadrant and closer to low pressure centers and when the vertical motion maximum is lower in the atmosphere at higher temperatures (Fig. 6.2).

In this chapter, we briefly examine some basic relationships among the large-scale structure and evolution of the storm and the surface snow rates. We use the low pressure tracks to determine the location, strength, and evolution of the low pressure center.

6.1 Snow rate and geographic pattern and distribution

To visualize the distribution of hourly snow rates relative to the low pressure center, we present a plot of precipitation rates in a Lagrangian framework, where the center of the plot represents the low pressure center and the points are plotted relative to the low (Fig. 6.3a). Each point in Fig. 6.3 represents an hourly snow rate at an ASOS station. Most of the winter season storms with appreciable snow had low center tracks offshore of the northeast US (Fig.

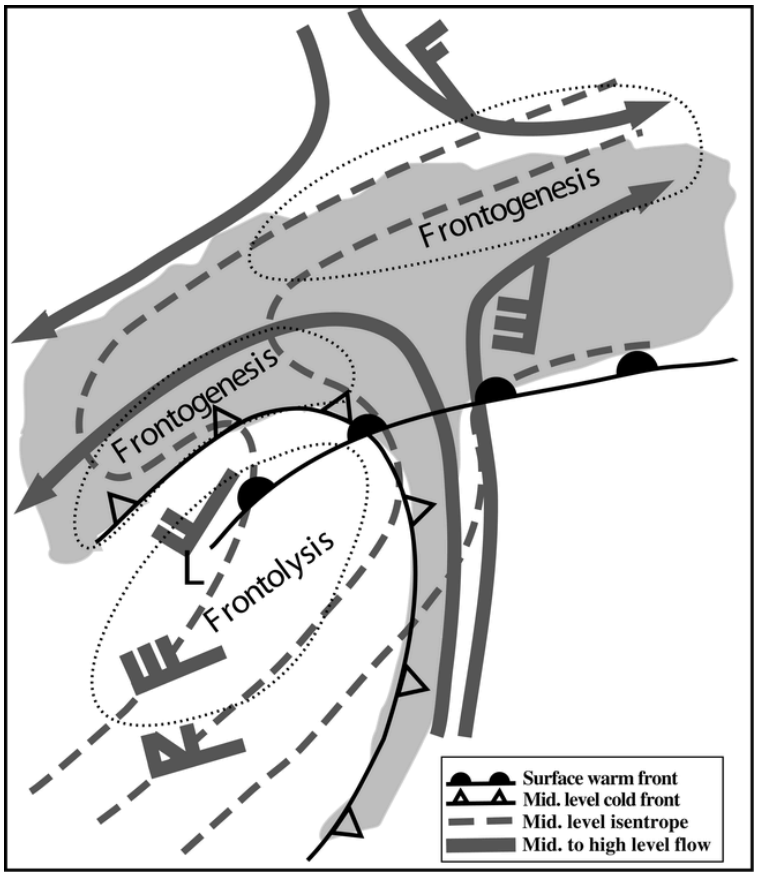

Figure 6.1: Idealized schematic of frontogenesis and deformation in the context of an extratopical low pressure system. Figure 18 from Han et al. (2007).

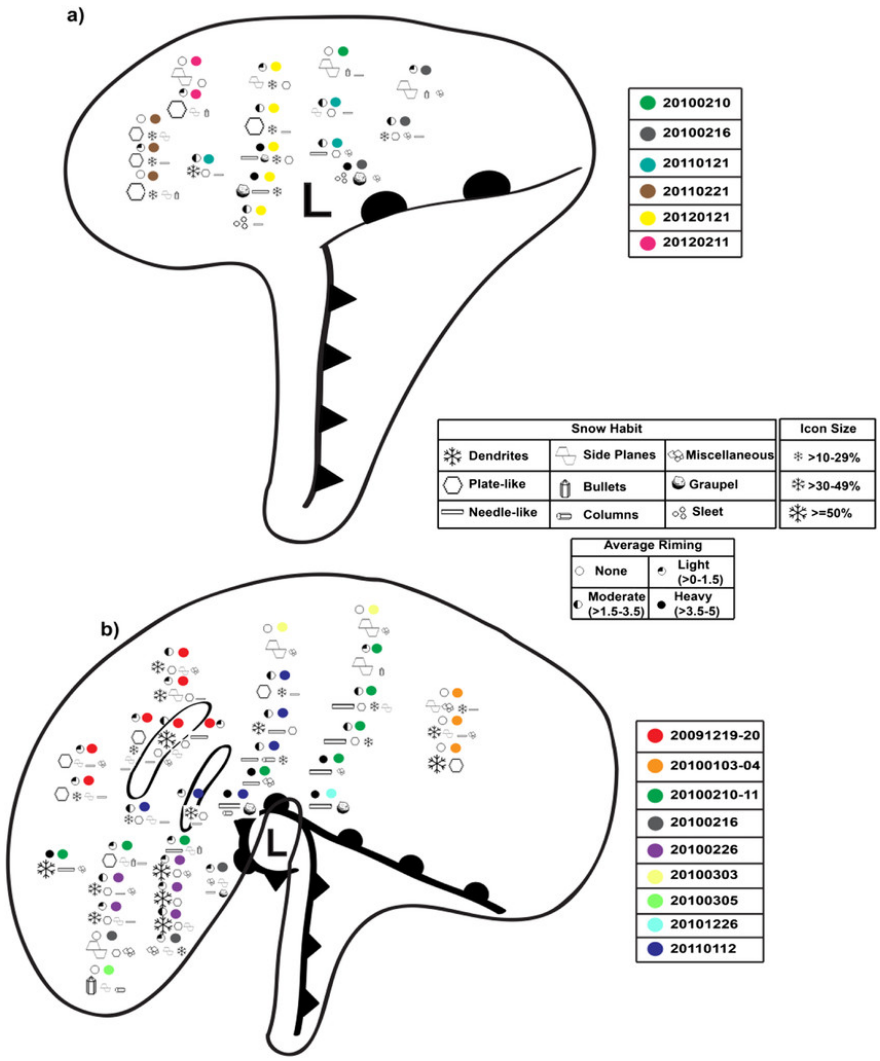

Figure 6.2: Observed snow particle characteristics manually classified based on surface observations in 12 storms and plotted relative to an idealized cloud shield and frontal positions in (a) the developing cyclone stage and (b) the mature cylcone stage. Riming intensity ranges from no riming (open circle) to heavy riming (filled black circle). Figure 3 from Colle et al. (2014).

Table 6.1: Number of observations and median and mean values of precipitation rate distribution by storm quadrant.

	Number of observations	**Liquid Equivalent Precipitation Rate [mm hr^{-1}]**	
		Median	Mean
NW	3329	0.3	0.58
NE	1877	0.5	0.84
SW	913	0	0.35
SE	442	0.3	0.67

2.9). This tendency for the low tracks to be offshore and the shape of the coastline yields a geographic bias of the sample to favor observations in the northwest quadrant relative to the low pressure center (Fig. 6.3a). There is sufficient density of observations in the northwest quadrant to suggest a gradient in snow rates with higher values more common closer to the low pressure center. The northeast quadrant, where frontogenesis typically occurs associated with the warm front, had the highest median and mean hourly snow rates among the four quadrants (Table 6.1).

The low-centric spatial distributions of snow rate align with our expectations given typical spatial patterns of large-scale lifting associated with different storm stages (Fig. 6.3) indicating that frontogenesis and frontolysis are likely dominant mechanisms at play. We did not directly look at the role of frontogenesis in these observations, but our collaborators at Stonybrook University have found that frontogenesis in these storms most commonly occurs in the NE quadrant and stretches into the eastern portion of the NW quadrant (Yeh 2023). More active riming closer to the low, as found in Colle et al. (2014), would be consistent with heavier liquid water equivalents all other factors being equal but ASOS data does not let us assess this hypothesis.

In Figure 6.4, the data in Figure 6.3a are shown in terms of 2D distributions of the distance to low pressure center vs. liquid equivalent precipitation rate. Low snow rates are the most common observations in all four quadrants. Heavy snow rates (> 2.5 mm hr^{-1} liquid water equivalent) are rare and those that do occur tend to be in the northwest or northeast quadrants (Fig. 6.4). Overall in the northwest quadrant of these northeast US winter storms, the occurrence of snow observations is more common between 250 to 1000 km distance from the low pressure center as compared to closer or further away.

As a further check to see if there are any robust relations among our variables, we normalize the 2D distribution in Fig. 6.4a by the snow rate and by the distance to low pressure center (Fig. 6.5). The normalized plots help to visually reduce the skewness in the 2D distribution in Fig. 6.4. The histogram normalized by the snow rate (Fig. 6.5a) indicates that snow rates of all

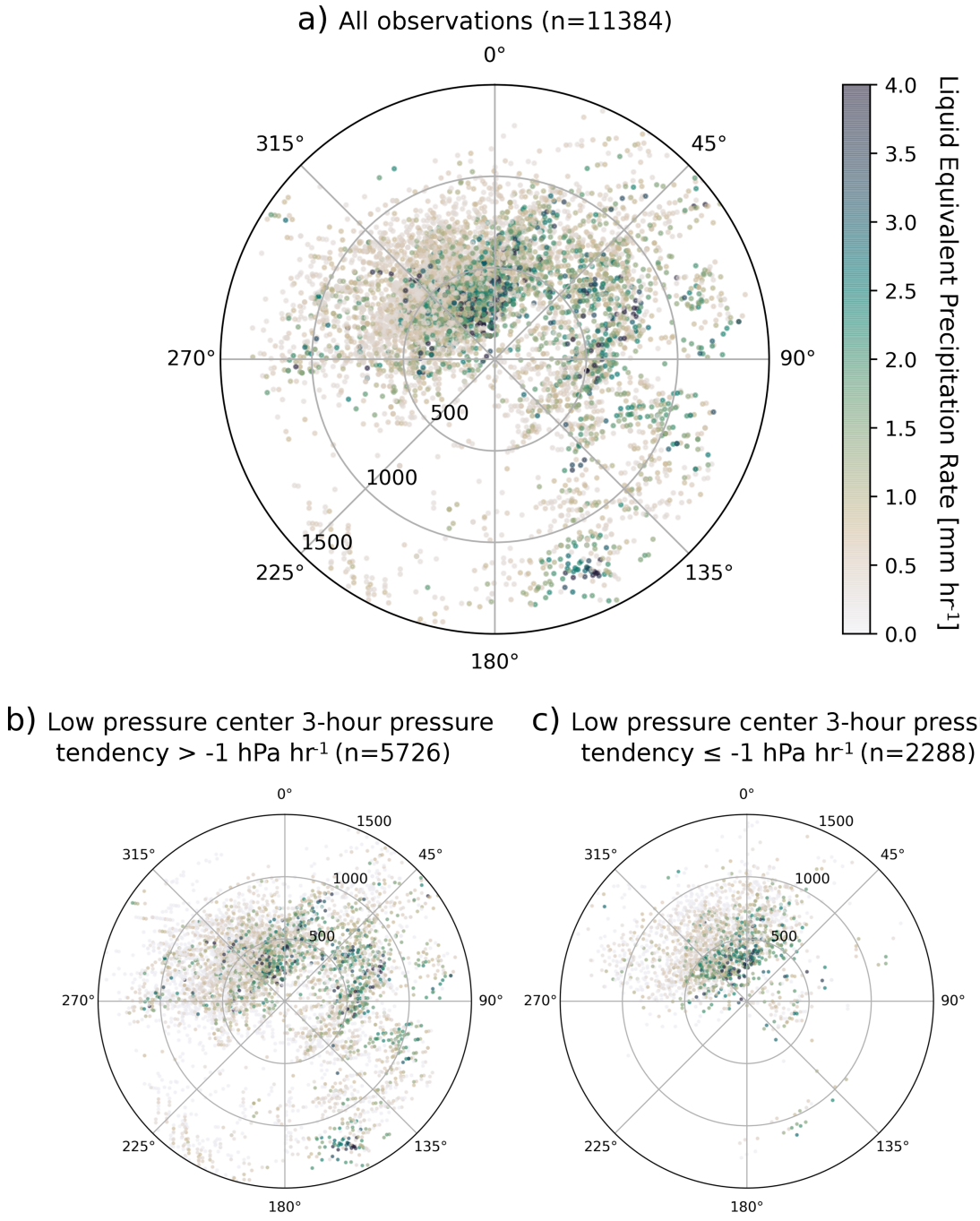

Figure 6.3: Lagrangian low-centric framework plot of hourly snowfall rates. The center of each plot represents the tracked low pressure center and each point represents 1 hour of data from an ASOS station colored by the associated liquid equivalent snowfall rate. (a) shows all data, (b) and (c) are the same data subset by pressure tendency magnitude above and below -1 hPa hr^{-1}.

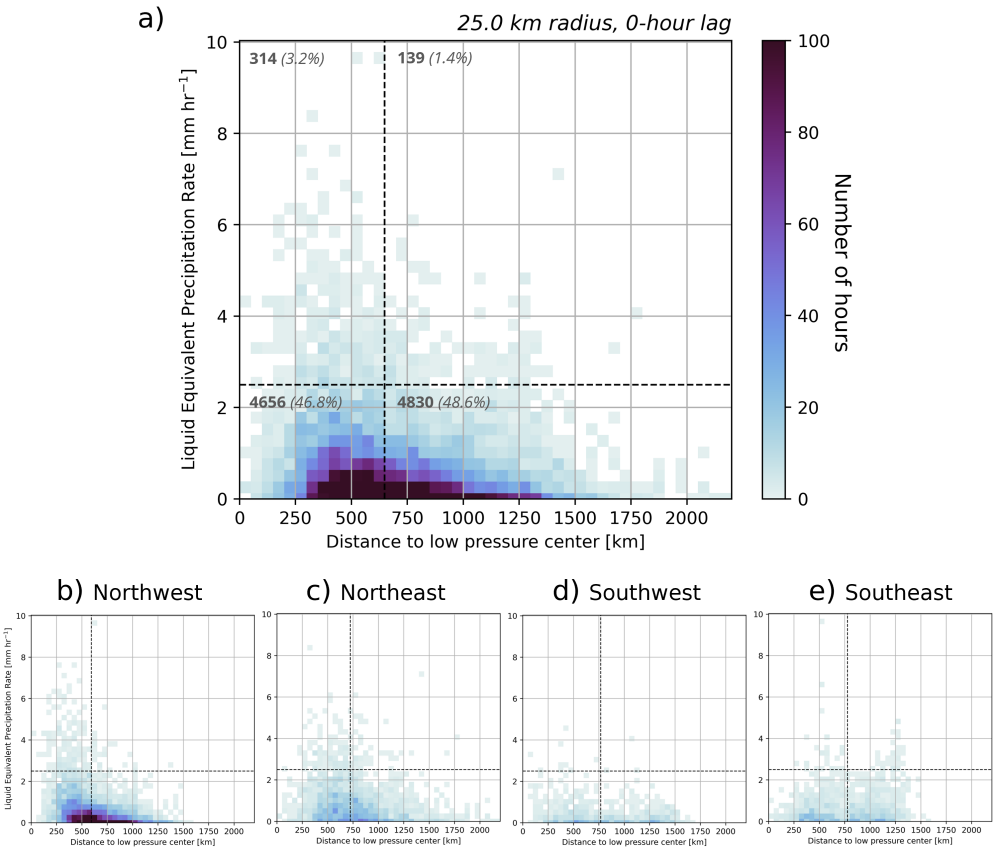

Figure 6.4: 2D distribution of distance to low pressure center [km] versus liquid equivalent precipitation rate [mm hr^{-1}] for (a) all observations (median: 647 km), and observations in the (b) northwest (median: 592 km), (c) northeast (median: 722 km), (d) southwest (median: 768 km), and (e) southeast (median: 777 km) quadrants relative to the low pressure center. In each panel the median distance is annotated with a vertical black dashed line and 2.5 mm hr^{-1} is annotated with a horizontal black dashed line.

magnitudes are most common between 250-750 km from the low pressure center. Normalizing the histogram by the distance to low pressure center (Fig. 6.5b) shows that for any given distance from the low pressure center, very low snow rates (< 0.5 mm hr^{-1} liquid water equivalent) are the most common.

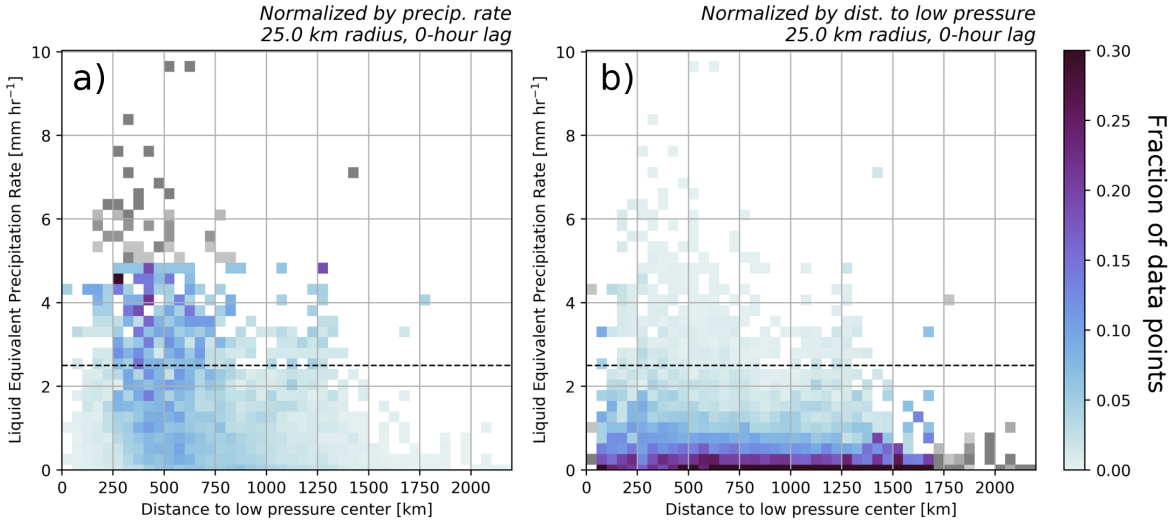

Figure 6.5: Normalized 2D distributions of distance to low pressure center [km] versus liquid equivalent precipitation rate [mm hr^{-1}] for snow observations. (a) Normalized by liquid equivalent precipitation rate and (b) normalized by distance to low pressure center. Bins are colored by the fraction of observations within each (a) precipitation and (b) distance bin. Bins colored in a grey scale indicate those with less than 10 observations. 2.5 mm hr^{-1} is annotated with a horizontal black dashed line.

6.2 Snow rates associated with different storm stages (pressure tendency)

In this section, we explore potential relationships between the storm stage and surface snowfall rates. To do this, we look at the distributions of snow rates in the context of 3-hour pressure tendencies – both of the low pressure center and at the ASOS surface station. Hourly snow rate observations subset on the cyclone's 3-hour pressure tendency (Figure 6.3b,c) indicate that rapid intensification (3-hour pressure tendency ≤ -1 hPa hr^{-1}) occurs for about 30% of the snow observations and those observations are mostly in the northwest and northeast quadrants. Values of 3-hour pressure tendency > -1 hPa hr^{-1} correspond to times when the pressure is increasing, not changing, or only slightly decreasing. Taking into account the geographic bias

of observations associated with the near coastal low pressure tracks, there is some evidence that stronger snow rates during periods of cyclone rapid intensification mostly occur in the northwest quadrant within 500 km of the low pressure center (Fig. 6.3c).

In addition to examining the pressure tendency within the low pressure center, we also evaluated the pressure tendency at the ASOS surface station and the relationship with surface snow rates. Figure 6.6 shows a 2D distributions of 3-hour station pressure tendency [hPa hr^{-1}] and liquid equivalent precipitation rate [mm hr^{-1}]. Roughly 86% of heavy snow observations (> 2.5 mm hr^{-1}) were observed during times when the 3-hour pressure tendency observed at the ASOS station was negative (i.e. pressure was decreasing). When the pressure was increasing, the vast majority (> 98%) of the snow observations were < 2.5 mm hr^{-1} (Fig. 6.6). Stations in the northeast and southeast quadrants have lower median 3-hour pressure tendencies (both -0.77 hPa hr^{-1}) compared to the medians for the stations in the northwest (-0.27 hPa hr^{-1}) and southwest (0.1 hPa hr^{-1}) quadrants (Fig. 6.6). Visually removing the skewness by normalizing the plots by liquid equivalent precipitation rate indicates that for a given snow rate, the 3-hour pressure tendency is likely to decrease as the snow rate increases (Fig. 6.7a). Normalizing by the pressure tendency (Fig. 6.7b) does not add much information to what is shown in Figure 6.6.

6.3 Summary

In this chapter we examined the relationships between hourly snowfall rates and the storm structure and storm stage. Our findings our consistent with previous work in that most hourly heavy snow observations occur in the northwest and northeast storm quadrants, are found closer to the low pressure center (usually within 500 km), and are associated with regions of large-scale lifting (i.e. strong frontogenesis) (e.g. Han et al. 2007; Novak et al. 2010; Colle et al. 2014; Ganetis et al. 2018). Our collaborators at Stonybrook University (P. Yeh, personal communication) are doing a comprehensive analysis of the variability of northeast US winter storm precipitation structures within the cyclone comma head and their relations to lift, stability, and shear which will expand upon and complement the work in this thesis.

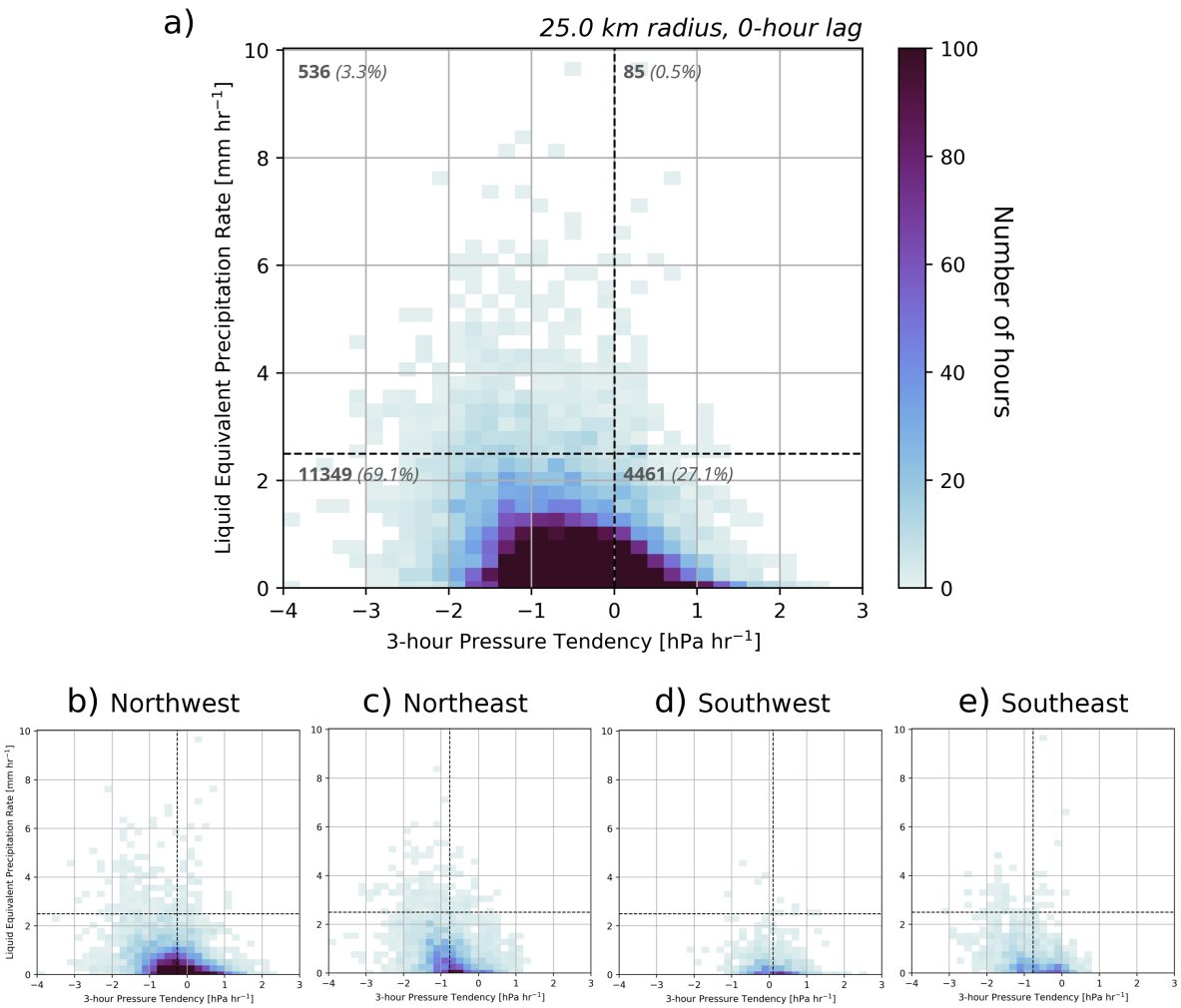

Figure 6.6: 2D distribution of 3-hour station pressure tendency [hPa hr^{-1}] versus liquid equivalent precipitation rate [mm hr^{-1}] for (a) all observations (median: -0.4 hPa hr^{-1}) and observations in the (b) northwest (median: -0.27 hPa hr^{-1}), (c) northeast (median: -0.77 hPa hr^{-1}), (c) southwest (median: 0.1 hPa hr^{-1}), and (d) southeast (median: -0.77 hPa hr^{-1}) storm quadrants relative to the low pressure center. In (a) 0 hPa hr^{-1} is annotated with a vertical black dashed line and 2.5 mm hr^{-1} is annotated with a horizontal black dashed line. Median pressure tendency is annotated with a vertical black dashed line in (b)–(e).

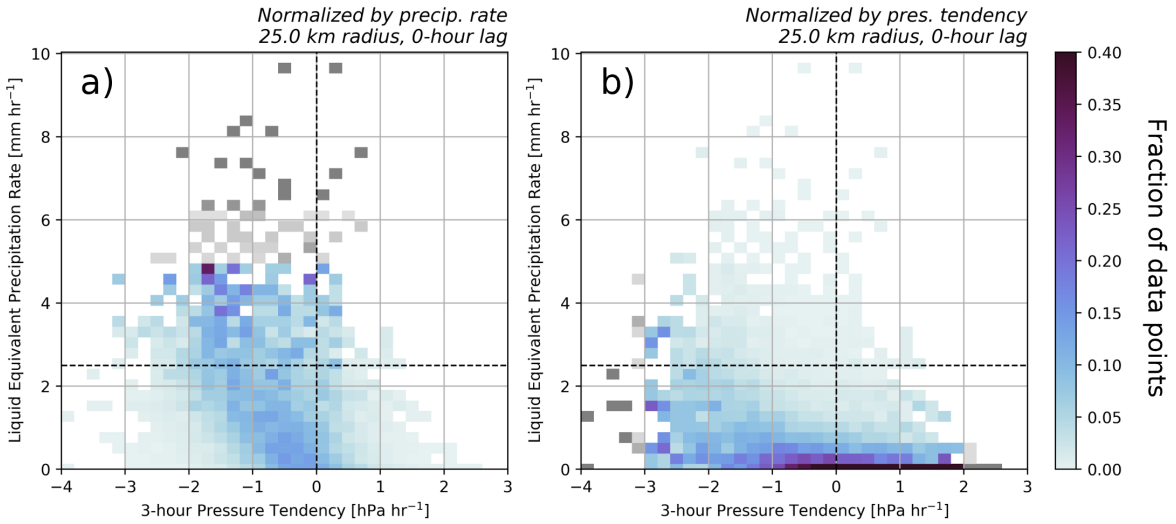

Figure 6.7: Normalized 2D distribution of 3-hour MSLP tendency [hPa hr^{-1}] versus liquid equivalent precipitation rate [mm hr^{-1}] for snow observations (a) normalized by liquid equivalent precipitation rate and (b) normalized by 3-hour MSLP tendency. Bins are colored by the fraction of observations within each (a) precipitation and (b) pressure tendency bin. Bins colored in a grey scale indicate bins with less than 10 observations. 0 hPa hr^{-1} is annotated with a vertical black dashed line and 2.5 mm hr^{-1} is annotated with a horizontal black dashed line.

Chapter 7

Summary and Conclusions

7.1 Summary

Where and when heavy snow is likely to occur in winter storms is both a high impact and thorny problem. We analyzed observations of a large sample of winter storm events in the northeast US from 264 storm days over 11 years (2012-2023) to improve the understanding of how hourly snowfall rates relate to structural characteristics of winter storms. Motivated by previous work, we examined several types of storm characteristics that are "prime suspects" in the occurrence of heavy snowfall: mesoscale snow bands (locally-enhanced reflectivity features), sets of mesoscale waves in velocity, and synoptic scale storm quadrant and pressure tendency. Regional radar mosaics over the northeast US were created from the NWS NEXRAD network including two new objective image processing methods developed specifically for this thesis work; the removal of mixed precipitation areas (image muting) and the identification of locally-enhanced reflectivity features in snow. Potential associations between radar reflectivity structures in the vicinity of ASOS stations and hourly snow rates were examined in terms of incidence of locally-enhanced reflectivity features as well as all snow echo. Regional radar mosaics of Doppler velocity waves were created to analyze the relationship between velocity waves and hourly surface snow rate. Additionally, we extracted low pressure center tracks from ERA5 reanalysis data to analyze the spatial pattern of snow rates relative to the low pressure center.

Evidence from our analysis demonstrates that locally-enhanced reflectivity features are not consistently associated with heavy snowfall rates. This is partially due to the fact that enhanced radar reflectivity in snow does not always imply increased ice mass (i.e. aggregation, Table 1.1) and snow particles do not fall straight down, rather they are usually transported horizontally

10s of km from the location where they originally reached precipitation size. Our work suggests that it is more useful to focus on the duration of snow radar echo over a given location to predict higher snowfall accumulations rather than the locally-enhanced reflectivity features.

We examined the relationship between velocity waves and enhanced precipitation and found that while the precipitation rate during times with waves was slightly higher than times without waves and likely to not be random, the difference is small. We suspect that the slightly higher snow rates during times with waves may have more to do with frontogenesis than the waves themselves but this requires further work to determine. Sets of mesoscale velocity waves are often observed ahead of a warm front and near the occluded front (Hoban 2016), where frontogenesis typically occurs (Fig. 6.1). We also did not find any evidence that velocity waves had an association with enhanced reflectivity features.

Visualizing snow rates in a Lagrangian framework aligns with expectations given the regions where frontogenesis is likely to occur (Fig. 6.1). We found that higher snow rates were typically found closer to the low pressure center, particularly in the northwest and northeast quadrants. Higher snow rates were more prevalent when the pressure at the ASOS station was decreasing indicating that higher snow rates are more likely when the low pressure system is deepening.

7.2 Conclusions

Most of the time in northeast US winter storms, the snow rates are low (75% of hours had liquid equivalent snow rates less than 1 mm hr^{-1} and only 6% of hours had snow rates > 2.5 mm hr^{-1}). Our data set excludes conditions with high winds (> 5 m s^{-1}) so these data are representative of non-blizzard conditions.

While case studies can be informative, they may not be representative. Case studies often focus on extreme examples and the lessons learned can not necessarily be generalized to a large sample winter storms that includes a range of storm intensities and durations. Previous case studies of winter storms have focused on events with high snowfall accumulations and have encouraged the idea that all snow bands are associated with heavy snow at the surface which this work shows is not accurate. Primary bands are associated with strong frontogenesis and high snowfall accumulation but don't occur that often (Novak et al. 2004; Kenyon et al. 2020; Ganetis et al. 2018). Multi-bands occur more frequently but are found in environments with and without frontogenesis (Ganetis et al. 2018). The NASA IMPACTS winter field program was organized around improving understanding of mesoscale snow bands with the goal to improved prediction of snowfall accumulation. Our findings indicate that mesoscale snowbands are features of the reflectivity field that are not that informative about heavy snow.

Our results confirm findings from previous work which suggests that prioritizing times and

locations where the low pressure is deepening and locations of large-scale lifting (i.e. strong frontogenesis) is beneficial when predicting heavy snow rates. Additionally, our work indicates that examining the duration (time and location) of *all* snow precipitation radar echo is more useful for forecasting regions of high snow accumulation rather than focusing on mesoscale snow bands.

7.3 Future Work

It would be useful to thoroughly and quantitatively examine relative skill of using the duration of snowfall above a threshold (e.g. area threshold methods, Krajewski et al. 1992) to estimate snowfall accumulation as compared to conventional methods applying Z-S relations pixel by pixel for each scan. This method could be tested using a variety of snow rate thresholds (e.g. 0.5, 1, 2 mm hr^{-1}) and by using different Z-S relationships to convert to snow rate.

This work covers nearly the entire NEXRAD archive (post dual-polarization implementation) for the northeast US so there are not any more observations for this region available. Similar methods could be applied to storms in the central US and a collaborator (A. Michaelis, personal communication) is working on this. The Western US has too much beam blockage and few storm tracks (Bentley et al. 2019) to be suitable for this type of analysis.

The wind profile plays a role in determining the vertical column continuity of snowfall. It may be useful to explore the Lagrangian patterns of the vertical wind profile using upper air sounding data sets. The New York State Mesonet includes 17 wind profilers which also may be suitable for this purpose (Brotzge et al. 2020).

We are in the early stages of adapting our feature detection method to identify local enhancements in the vertical cross sections of reflectivity from the ER-2 radars which will help to quantify the natures of tilted and smeared features but the ER-2 data set comprises only 74 flight legs with snow to the surface.

Primary snow bands (longer than 200 km) are associated with strong frontogenesis (Novak and Colle 2012). Multibands (sets of snow bands < 200 km) are much more common than primary bands and can occur in conditions with weak to no frontogenesis (Ganetis et al. 2018). We did not distinguish between primary and multi-bands in our enhanced reflectivity feature analysis and rather looked at all local enhancements together. In the near term, we will assess whether the few samples of high feature area×time and heavy snow rates are mostly occurring associated with primary bands.

REFERENCES

Alku, L., D. Moisseev, T. Aittomäki, and V. Chandrasekar, 2015: Identification and Suppression of Nonmeteorological Echoes Using Spectral Polarimetric Processing. *IEEE Transactions on Geoscience and Remote Sensing*, **53 (7)**, 3628–3638, https://doi.org/10.1109/TGRS.2014.2380476.

Ansari, S., and Coauthors, 2018: Unlocking the Potential of NEXRAD Data through NOAA's Big Data Partnership. *Bulletin of the American Meteorological Society*, **99 (1)**, 189–204, https://doi.org/10.1175/BAMS-D-16-0021.1.

Arkin, P. A., and B. N. Meisner, 1987: The Relationship between Large-Scale Convective Rainfall and Cold Cloud over the Western Hemisphere during 1982-84. *Monthly Weather Review*, **115 (1)**, 51–74, https://doi.org/10.1175/1520-0493(1987)115<0051:TRBLSC>2.0.CO;2.

Battan, L. J., 1973: *Radar Observation of the Atmosphere*. Chicago : University of Chicago Press, 1973., Chicago.

Baxter, M. A., and P. N. Schumacher, 2017: Distribution of Single-Banded Snowfall in Central U.S. Cyclones. *Weather and Forecasting*, **32 (2)**, 533–554, https://doi.org/10.1175/WAF-D-16-0154.1.

Bentley, A. M., L. F. Bosart, and D. Keyser, 2019: A Climatology of Extratropical Cyclones Leading to Extreme Weather Events over Central and Eastern North America. *Monthly Weather Review*, **147 (5)**, 1471–1490, https://doi.org/10.1175/MWR-D-18-0453.1.

Bringi, V., and V. Chandrasekar, 2001: *Polarimetric Doppler Weather Radar: Principles and Applications*. Cambridge University Press.

Brotzge, J. A., and Coauthors, 2020: A Technical Overview of the New York State Mesonet Standard Network. *Journal of Atmospheric and Oceanic Technology*, **37 (10)**, 1827–1845, https://doi.org/10.1175/JTECH-D-19-0220.1.

Bullock, RG., BG. Brown, and TL. Fowler, 2016: Method for object-based diagnostic evaluation. *NCAR Technical Note*.

Calvo, L., I. Christel, M. Terrado, F. Cucchietti, and M. Pérez-Montoro, 2021: Users' cognitive load: A key aspect to successfully communicate visual climate information. *Bulletin of the American Meteorological Society*, **103 (1)**, E1–E16.

Churchill, D. D., and R. A. Houze, 1984: Development and Structure of Winter Monsoon Cloud Clusters On 10 December 1978. *Journal of the Atmospheric Sciences*, **41 (6)**, 933–960, https://doi.org/10.1175/1520-0469(1984)041<0933:DASOWM>2.0.CO;2.

Clark, J. H. E., R. P. James, and R. H. Grumm, 2002: A Reexamination of the Mechanisms Responsible for Banded Precipitation. *Monthly Weather Review*, **130 (12)**, 3074–3086, https://doi.org/10.1175/1520-0493(2002)130<3074:AROTMR>2.0.CO;2.

Colle, B. A., D. Stark, and S. E. Yuter, 2014: Surface Microphysical Observations within East Coast Winter Storms on Long Island, New York. *Monthly Weather Review*, **142 (9)**, 3126–3146, https://doi.org/10.1175/MWR-D-14-00035.1.

Colle, B. A., P. Yeh, J. A. Finlon, L. McMurdie, V. McDonald, and A. DeLaFrance, 2023: An Investigation of a Northeast U.S. Cyclone Event Without Well-Defined Snow Banding During IMPACTS. *Monthly Weather Review*, **-1 (aop)**, https://doi.org/10.1175/MWR-D-22-0296.1.

Connelly, R., and B. A. Colle, 2019: Validation of Snow Multibands in the Comma Head of an Extratropical Cyclone Using a 40-Member Ensemble. *Weather and Forecasting*, **34 (5)**, 1343–1363, https://doi.org/10.1175/WAF-D-18-0182.1.

Crawford, A. D., E. A. P. Schreiber, N. Sommer, M. C. Serreze, J. C. Stroeve, and D. G. Barber, 2021: Sensitivity of Northern Hemisphere Cyclone Detection and Tracking Results to Fine Spatial and Temporal Resolution Using ERA5. *Monthly Weather Review*, **149 (8)**, 2581–2598, https://doi.org/10.1175/MWR-D-20-0417.1.

Cressman, G. P., 1959: An Operational Objective Analysis System. *Monthly Weather Review*, **87 (10)**, 367–374, https://doi.org/10.1175/1520-0493(1959)087<0367:AOOAS>2.0.CO;2.

Ferraro, R. R., and Coauthors, 2013: An Evaluation of Microwave Land Surface Emissivities Over the Continental United States to Benefit GPM-Era Precipitation Algorithms. *IEEE Transactions on Geoscience and Remote Sensing*, **51 (1)**, 378–398, https://doi.org/10.1109/TGRS.2012.2199121.

Fujiyoshi, Y., T. Endoh, T. Yamada, K. Tsuboki, Y. Tachibana, and G. Wakahama, 1990: Determination of a Z-R Relationship for Snowfall Using a Radar and High Sensitivity Snow Gauges. *Journal of Applied Meteorology and Climatology*, **29 (2)**, 147–152, https://doi.org/10.1175/1520-0450(1990)029<0147:DOARFS>2.0.CO;2.

Ganetis, S. A., and B. A. Colle, 2015: The Thermodynamic and Microphysical Evolution of an Intense Snowband during the Northeast U.S. Blizzard of 8–9 February 2013. *Monthly Weather Review*, **143 (10)**, 4104–4125, https://doi.org/10.1175/MWR-D-14-00407.1.

Ganetis, S. A., B. A. Colle, S. E. Yuter, and N. P. Hoban, 2018: Environmental Conditions Associated with Observed Snowband Structures within Northeast U.S. Winter Storms. *Monthly Weather Review*, **146 (11)**, 3675–3690, https://doi.org/10.1175/MWR-D-18-0054.1.

Giangrande, S. E., J. M. Krause, and A. V. Ryzhkov, 2008: Automatic Designation of the Melting Layer with a Polarimetric Prototype of the WSR-88D Radar. *Journal of Applied Meteorology and Climatology*, **47 (5)**, 1354–1364, https://doi.org/10.1175/2007JAMC1634.1.

Good, P., 2013: *Permutation Tests: A Practical Guide to Resampling Methods for Testing Hypotheses*. Springer Science & Business Media.

Griffin, E. M., T. J. Schuur, and A. V. Ryzhkov, 2020: A polarimetric radar analysis of ice microphysical processes in melting layers of winter storms using S-band quasi-vertical profiles. *Journal of Applied Meteorology and Climatology*, **59 (4)**, 751–767.

Griffin, E. M., T. J. Schuur, A. V. Ryzhkov, H. D. Reeves, and J. C. Picca, 2014: A Polarimetric and Microphysical Investigation of the Northeast Blizzard of 8–9 February 2013. *Weather and Forecasting*, **29 (6)**, 1271–1294, https://doi.org/10.1175/WAF-D-14-00056.1.

Guarino, J., and T. Firestine, 2010: Effects of the February 2010 Snowstorms on Airline Performance. Tech. Rep. SR-019, US Department of Transportation. https://doi.org/10.21949/1501623.

Han, M., R. M. Rauber, M. K. Ramamurthy, B. F. Jewett, and J. A. Grim, 2007: Mesoscale Dynamics of the Trowal and Warm-Frontal Regions of Two Continental Winter Cyclones. *Monthly Weather Review*, **135 (5)**, 1647–1670, https://doi.org/10.1175/MWR3377.1.

Harrower, M., 2007: The cognitive limits of animated maps. *Cartographica: The International Journal for Geographic Information and Geovisualization*, **42 (4)**, 349–357.

Helms, C. N., M. L. W. McLinden, G. M. Heymsfield, and S. R. Guimond, 2020: Reducing Errors in Velocity–Azimuth Display (VAD) Wind and Deformation Retrievals from Airborne Doppler Radars in Convective Environments. *Journal of Atmospheric and Oceanic Technology*, **37 (12)**, 2251–2266, https://doi.org/10.1175/JTECH-D-20-0034.1.

Helmus, J. J., and S. M. Collis, 2016: The Python ARM Radar Toolkit (Py-ART), a library for working with weather radar data in the Python programming language. *Journal of Open Research Software*, **4**, https://doi.org/10.5334/jors.119.

Hersbach, H., and Coauthors, 2020: The ERA5 global reanalysis. *Quarterly Journal of the Royal Meteorological Society*, **146 (730)**, 1999–2049, https://doi.org/10.1002/qj.3803.

Heymsfield, G. M., and Coauthors, 1996: The EDOP radar system on the high-altitude NASA ER-2 aircraft. *Journal of Atmospheric and Oceanic Technology*, **13 (4)**, 795–809.

Hoban, N. P., 2016: Observed Characteristics of Mesoscale Banding in Coastal Northeast U.S. Snow Storms. M.S. Thesis, North Carolina State University.

Holt, C. A., and S. P. Sullivan, 2023: Permutation tests for experimental data. *Experimental Economics*, **26 (4)**, 775–812, https://doi.org/10.1007/s10683-023-09799-6.

Ivić, I. R., 2019: A simple hybrid technique to reduce bias of copolar correlation coefficient estimates. *Journal of Atmospheric and Oceanic Technology*, **36 (9)**, 1813–1833.

Jamil, N., T. M. T. Sembok, and Z. A. Bakar, 2008: Noise removal and enhancement of binary images using morphological operations. *2008 International Symposium on Information Technology*, Vol. 4, 1–6, https://doi.org/10.1109/ITSIM.2008.4631954.

Kenyon, J. S., D. Keyser, L. F. Bosart, and M. S. Evans, 2020: The Motion of Mesoscale Snowbands in Northeast U.S. Winter Storms. *Weather and Forecasting*, **35 (1)**, 83–105, https://doi.org/10.1175/WAF-D-19-0038.1.

Kocin, P. J., and L. W. Uccellini, 2004: *Northeast Snowstorms.*, Vol. 1. Meteorological Monographs.

Krajewski, W. F., M. L. Morrissey, J. A. Smith, and D. T. Rexroth, 1992: The Accuracy of the Area-Threshold Method: A Model-based Simulation Study. *Journal of Applied Meteorology and Climatology*, **31 (12)**, 1396–1406, https://doi.org/10.1175/1520-0450(1992)031<1396:TAOTAT>2.0.CO;2.

Kumjian, M. R., 2013a: Principles and Applications of Dual-Polarization Weather Radar. Part I: Description of the Polarimetric Radar Variables. *Journal of Operational Meteorology*, **1 (19)**, 226–242.

Kumjian, M. R., 2013b: Principles and Applications of Dual-Polarization Weather Radar. Part II: Warm- and Cold-Season Applications. *Journal of Operational Meteorology*, **1 (20)**, 243–264.

Lackmann, G. M., and G. Thompson, 2019: Hydrometeor Lofting and Mesoscale Snowbands. *Monthly Weather Review*, **147 (11)**, 3879–3899, https://doi.org/10.1175/MWR-D-19-0036.1.

LaFleur, B. J., and R. A. Greevy, 2009: Introduction to Permutation and Resampling-Based Hypothesis Tests∗. *Journal of Clinical Child & Adolescent Psychology*, **38 (2)**, 286–294, https://doi.org/10.1080/15374410902740411.

Li, L., and Coauthors, 2016: The NASA High-Altitude Imaging Wind and Rain Airborne Profiler. *IEEE Transactions on Geoscience and Remote Sensing*, **54 (1)**, 298–310, https://doi.org/10.1109/TGRS.2015.2456501.

Machado, L. a. T., and W. B. Rossow, 1993: Structural Characteristics and Radiative Properties of Tropical Cloud Clusters. *Monthly Weather Review*, **121 (12)**, 3234–3260, https://doi.org/10.1175/1520-0493(1993)121<3234:SCARPO>2.0.CO;2.

Martinaitis, S. M., S. B. Cocks, Y. Qi, B. T. Kaney, J. Zhang, and K. Howard, 2015: Understanding Winter Precipitation Impacts on Automated Gauge Observations within a Real-Time System. *Journal of Hydrometeorology*, **16 (6)**, 2345–2363, https://doi.org/10.1175/JHM-D-15-0020.1.

Mayer, R. E., and R. Moreno, 2003: Nine ways to reduce cognitive load in multimedia learning. *Educational psychologist*, **38 (1)**, 43–52.

McLinden, M. L. W., L. Li, G. M. Heymsfield, M. Coon, and A. Emory, 2021: The NASA GSFC 94-GHz Airborne Solid-State Cloud Radar System (CRS). *Journal of Atmospheric and Oceanic Technology*, **38 (5)**, 1001–1017, https://doi.org/10.1175/JTECH-D-20-0127.1.

McMurdie, L. A., and Coauthors, 2022: Chasing Snowstorms: The Investigation of Microphysics and Precipitation for Atlantic Coast-Threatening Snowstorms (IMPACTS) Campaign. *Bulletin of the American Meteorological Society*, **103 (5)**, E1243–E1269, https://doi.org/10.1175/BAMS-D-20-0246.1.

Menne, M. J., I. Durre, R. S. Vose, B. E. Gleason, and T. G. Houston, 2012: An Overview of the Global Historical Climatology Network-Daily Database. *Journal of Atmospheric and Oceanic Technology*, **29 (7)**, 897–910, https://doi.org/10.1175/JTECH-D-11-00103.1.

Miller, M. A., S. E. Yuter, N. P. Hoban, L. M. Tomkins, and B. A. Colle, 2022: Detecting wave features in Doppler radial velocity radar observations. *Atmospheric Measurement Techniques*, **15 (6)**, 1689–1702, https://doi.org/10.5194/amt-15-1689-2022.

Nicosia, D. J., and R. H. Grumm, 1999: Mesoscale Band Formation in Three Major Northeastern United States Snowstorms. *Weather and Forecasting*, **14 (3)**, 346–368, https://doi.org/10.1175/1520-0434(1999)014<0346:MBFITM>2.0.CO;2.

NOAA, 2017: WSR-88D Meteorological Observations, Federal Meteorological Handbook No. 11, Part C WSR-88D Products and Algorithms. Tech. Rep. FCM-H11C-2017, Office of the Federal Coordinator for Meteorological Services and Supporting Research, NOAA, Silver Spring, MD, 394 pp.

Novak, D. R., L. F. Bosart, D. Keyser, and J. S. Waldstreicher, 2004: An Observational Study of Cold Season–Banded Precipitation in Northeast U.S. Cyclones. *Weather and Forecasting*, **19 (6)**, 993–1010, https://doi.org/10.1175/815.1.

Novak, D. R., and B. A. Colle, 2012: Diagnosing Snowband Predictability Using a Multimodel Ensemble System. *Weather and Forecasting*, **27 (3)**, 565–585, https://doi.org/10.1175/WAF-D-11-00047.1.

Novak, D. R., B. A. Colle, and A. R. Aiyyer, 2010: Evolution of Mesoscale Precipitation Band Environments within the Comma Head of Northeast U.S. Cyclones. *Monthly Weather Review*, **138 (6)**, 2354–2374, https://doi.org/10.1175/2010MWR3219.1.

Novak, D. R., B. A. Colle, and R. McTaggart-Cowan, 2009: The Role of Moist Processes in the Formation and Evolution of Mesoscale Snowbands within the Comma Head of Northeast U.S. Cyclones. *Monthly Weather Review*, **137 (8)**, 2662–2686, https://doi.org/10.1175/2009MWR2874.1.

Novak, D. R., B. A. Colle, and S. E. Yuter, 2008: High-Resolution Observations and Model Simulations of the Life Cycle of an Intense Mesoscale Snowband over the Northeastern United States. *Monthly Weather Review*, **136 (4)**, 1433–1456, https://doi.org/10.1175/2007MWR2233.1.

Novak, D. R., and Coauthors, 2023: Innovations in Winter Storm Forecasting and Decision Support Services. *Bulletin of the American Meteorological Society*, **104 (3)**, E715–E735, https://doi.org/10.1175/BAMS-D-22-0065.1.

Oue, M., B. A. Colle, S. E. Yuter, P. Kollias, P. Yeh, and L. M. Tomkins, 2024: Microscale Updrafts Within Northeast U.S. Coastal Snowstorms Using High-Resolution Cloud Radar Measurements. *Monthly Weather Review*, **-1 (aop)**, https://doi.org/10.1175/MWR-D-23-0055.1.

Oue, M., P. Kollias, E. P. Luke, and J. Mead, 2017: A New Ka-Band Scanning Radar Facility: Polarimetric and Doppler Spectra Measurements of Snow Events. *AGU Fall Meeting Abstracts*, **A31G-2270**.

Picca, J. C., D. M. Schultz, B. A. Colle, S. Ganetis, D. R. Novak, and M. J. Sienkiewicz, 2014: The Value of Dual-Polarization Radar in Diagnosing the Complex Microphysical Evolution of

an Intense Snowband. *Bulletin of the American Meteorological Society*, **95 (12)**, 1825–1834, https://doi.org/10.1175/BAMS-D-13-00258.1.

Powell, S. W., R. A. Houze, and S. R. Brodzik, 2016: Rainfall-Type Categorization of Radar Echoes Using Polar Coordinate Reflectivity Data. *Journal of Atmospheric and Oceanic Technology*, **33 (3)**, 523–538, https://doi.org/10.1175/JTECH-D-15-0135.1.

Radford, J. T., G. M. Lackmann, and M. A. Baxter, 2019: An Evaluation of Snowband Predictability in the High-Resolution Rapid Refresh. *Weather and Forecasting*, **34 (5)**, 1477–1494, https://doi.org/10.1175/WAF-D-19-0089.1.

Rasmussen, R., M. Dixon, S. Vasiloff, F. Hage, S. Knight, J. Vivekanandan, and M. Xu, 2003: Snow Nowcasting Using a Real-Time Correlation of Radar Reflectivity with Snow Gauge Accumulation. *Journal of Applied Meteorology and Climatology*, **42 (1)**, 20–36, https://doi.org/10.1175/1520-0450(2003)042<0020:SNUART>2.0.CO;2.

Rasmussen, R., and Coauthors, 2001: Weather Support to Deicing Decision Making (WSDDM): A Winter Weather Nowcasting System. *Bulletin of the American Meteorological Society*, **82 (4)**, 579–596, https://doi.org/10.1175/1520-0477(2001)082<0579:WSTDDM>2.3.CO;2.

Rasmussen, R., and Coauthors, 2012: How Well Are We Measuring Snow: The NOAA/FAA/NCAR Winter Precipitation Test Bed. *Bulletin of the American Meteorological Society*, **93 (6)**, 811–829, https://doi.org/10.1175/BAMS-D-11-00052.1.

Rasmussen, R. M., J. Vivekanandan, J. Cole, B. Myers, and C. Masters, 1999: The Estimation of Snowfall Rate Using Visibility. *Journal of Applied Meteorology and Climatology*, **38 (10)**, 1542–1563, https://doi.org/10.1175/1520-0450(1999)038<1542:TEOSRU>2.0.CO;2.

Rauber, R. M., and S. W. Nesbitt, 2018: *Radar Meteorology: A First Course*. John Wiley & Sons.

Rinehart, R. E., 2004: *Radar for Meteorologists*. 4th ed., Rinehart, Columbia, Mo.

Ryzhkov, A. V., 2007: The Impact of Beam Broadening on the Quality of Radar Polarimetric Data. *Journal of Atmospheric and Oceanic Technology*, **24 (5)**, 729–744, https://doi.org/10.1175/JTECH2003.1.

Saltikoff, E., A. Huuskonen, H. Hohti, J. Koistinen, and H. Järvinen, 2010: Quality assurance in the FMI Doppler weather radar network. *Boreal Environment Research*.

Schiffer, R. A., and W. B. Rossow, 1983: The International Satellite Cloud Climatology Project (ISCCP): The First Project of the World Climate Research Programme. *Bulletin of the American Meteorological Society*, **64 (7)**, 779–784, https://doi.org/10.1175/1520-0477-64.7.779.

Schultz, D. M., and Coauthors, 2019: Extratropical cyclones: A century of research on meteorology's centerpiece. *Meteorological monographs*, **59**, 16–1.

Schweizer, J., J. Bruce Jamieson, and M. Schneebeli, 2003: Snow avalanche formation. *Reviews of Geophysics*, **41 (4)**, https://doi.org/10.1029/2002RG000123.

Shields, M. T., R. M. Rauber, and M. K. Ramamurthy, 1991: Dynamical Forcing and Mesoscale Organization of Precipitation Bands in a Midwest Winter Cyclonic Storm. *Monthly Weather Review*, **119 (4)**, 936–964, https://doi.org/10.1175/1520-0493(1991)119<0936:DFAMOO>2.0.CO;2.

Stark, D., B. A. Colle, and S. E. Yuter, 2013: Observed Microphysical Evolution for Two East Coast Winter Storms and the Associated Snow Bands. *Monthly Weather Review*, **141 (6)**, 2037–2057, https://doi.org/10.1175/MWR-D-12-00276.1.

Steiner, M., R. A. Houze, and S. E. Yuter, 1995: Climatological Characterization of Three-Dimensional Storm Structure from Operational Radar and Rain Gauge Data. *Journal of Applied Meteorology and Climatology*, **34 (9)**, 1978–2007, https://doi.org/10.1175/1520-0450(1995)034<1978:CCOTDS>2.0.CO;2.

Straka, J. M., D. S. Zrnić, and A. V. Ryzhkov, 2000: Bulk Hydrometeor Classification and Quantification Using Polarimetric Radar Data: Synthesis of Relations. *Journal of Applied Meteorology and Climatology*, **39 (8)**, 1341–1372, https://doi.org/10.1175/1520-0450(2000)039<1341:BHCAQU>2.0.CO;2.

Suchow, J. W., and G. A. Alvarez, 2011: Motion silences awareness of visual change. *Current Biology*, **21 (2)**, 140–143.

Sweller, J., P. L. Ayres, and S. Kalyuga, 2011: *Cognitive Load Theory*. New York : Springer, 2011., New York.

Tessendorf, S. A., and Coauthors, 2019: A Transformational Approach to Winter Orographic Weather Modification Research: The SNOWIE Project. *Bulletin of the American Meteorological Society*, **100 (1)**, 71–92, https://doi.org/10.1175/BAMS-D-17-0152.1.

Tomkins, L., S. Yuter, M. Miller, N. Corbin, and N. Hoban, 2023a: Northeast US Regional NEXRAD radar mosaics of winter storms from 1996-2023, part 1. Dryad, https://doi.org/10.5061/dryad.zcrjdfnk6.

Tomkins, L., S. Yuter, M. Miller, N. Corbin, and N. Hoban, 2023b: Northeast US Regional NEXRAD radar mosaics of winter storms from 1996-2023, part 2. Dryad, https://doi.org/10.5061/dryad.zcrjdfnk6.

Tomkins, L. M., S. E. Yuter, M. A. Miller, and L. R. Allen, 2022: Image muting of mixed precipitation to improve identification of regions of heavy snow in radar data. *Atmospheric Measurement Techniques*, **15 (18)**, 5515–5525, https://doi.org/10.5194/amt-15-5515-2022.

Varcie, M. M., and Coauthors, 2022: Precipitation Growth Processes in the Comma-Head Region of the 7 February 2020 Northeast Snowstorm: Results from IMPACTS. *Journal of the Atmospheric Sciences*, **80 (1)**, 3–29, https://doi.org/10.1175/JAS-D-22-0118.1.

Vivekanandan, J., V. Bringi, M. Hagen, and P. Meischner, 1994: Polarimetric radar studies of atmospheric ice particles. *IEEE Transactions on Geoscience and Remote Sensing*, **32 (1)**, 1–10, https://doi.org/10.1109/36.285183.

Warren, R. A., and A. Protat, 2019: Should Interpolation of Radar Reflectivity be Performed in Z or dBZ? *Journal of Atmospheric and Oceanic Technology*, **36 (6)**, 1143–1156, https://doi.org/10.1175/JTECH-D-18-0183.1.

Woodman, M., 1988: Yourdon dataflow diagrams: A tool for disciplined requirements analysis. *Information and Software Technology*, **30 (9)**, 515–533, https://doi.org/10.1016/0950-5849(88)90131-0.

Yeh, P., 2023: Variability of Cool Season Precipitation Structures Within the Cyclone Comma Head. Anapolis, MD.

Yeh, P., 2024: Identification of Cool-Season Precipitation Structures in the Northeast U.S. *in preparation*.

Yuter, S. E., and R. A. Houze, 1995: Three-Dimensional Kinematic and Microphysical Evolution of Florida Cumulonimbus. Part II: Frequency Distributions of Vertical Velocity, Reflectivity, and Differential Reflectivity. *Monthly Weather Review*, **123 (7)**, 1941–1963, https://doi.org/10.1175/1520-0493(1995)123<1941:TDKAME>2.0.CO;2.

Yuter, S. E., and R. A. Houze, 1997: Measurements of Raindrop Size Distributions over the Pacific Warm Pool and Implications for Z–R Relations. *Journal of Applied Meteorology and Climatology*, **36 (7)**, 847–867, https://doi.org/10.1175/1520-0450(1997)036<0847:MORSDO>2.0.CO;2.

Yuter, S. E., R. A. Houze, E. A. Smith, T. T. Wilheit, and E. Zipser, 2005: Physical Characterization of Tropical Oceanic Convection Observed in KWAJEX. *Journal of Applied Meteorology and Climatology*, **44 (4)**, 385–415, https://doi.org/10.1175/JAM2206.1.

Zaremba, T. J., R. M. Rauber, L. D. Girolamo, J. R. Loveridge, and G. M. McFarquhar, 2023: On the Radar Detection of Cloud Seeding Effects in Wintertime Orographic Cloud Systems. *Journal of Applied Meteorology and Climatology*, **63 (1)**, 27–45, https://doi.org/10.1175/JAMC-D-22-0154.1.

Zrnić, D. S., V. M. Melnikov, and A. V. Ryzhkov, 2006: Correlation Coefficients between Horizontally and Vertically Polarized Returns from Ground Clutter. *Journal of Atmospheric and Oceanic Technology*, **23 (3)**, 381–394, https://doi.org/10.1175/JTECH1856.1.

APPENDICES

Appendix A

List of storms

Table A.1: List of storm days between 1996-2023 used in the analysis. Dates are in YYYYMMDD format.

19960102	19960103	19960104	19960107	19960108	19960109	19960110	19960112
19960129	19960131	19960202	19960203	19960208	19960211	19960214	19960216
19960217	19960302	19960305	19960306	19960307	19960308	19960329	19961126
19961127	19961206	19961231	19970109	19970110	19970111	19970124	19970127
19970128	19970131	19970204	19970208	19970214	19970216	19970217	19970303
19970306	19970308	19970310	19970314	19970331	19971114	19971116	19971122
19971210	19971223	19971227	19971229	19971230	19980116	19980118	19980119
19980123	19980124	19980125	19980224	19980314	19980322	19981224	19981229
19981230	19990108	19990109	19990112	19990113	19990114	19990115	19990128
19990129	19990208	19990212	19990225	19990306	19990307	19990314	19990315
19990322	20000113	20000120	20000121	20000125	20000126	20000130	20000131
20000203	20000214	20000218	20000219	20000317	20001214	20001219	20001220
20001222	20001230	20001231	20010105	20010106	20010108	20010109	20010119
20010121	20010127	20010202	20010205	20010206	20010208	20010222	20010223
20010225	20010301	20010302	20010304	20010305	20010306	20010309	20010310
20010326	20010330	20011208	20011209	20020106	20020107	20020117	20020119
20020121	20020131	20020211	20020318	20020320	20021116	20021117	20021118
20021127	20021202	20021205	20021206	20021211	20021212	20021216	20021225
20021226	20030102	20030103	20030104	20030105	20030106	20030107	20030108
20030109	20030111	20030126	20030127	20030129	20030202	20030207	20030210
20030212	20030216	20030217	20030218	20030306	20030313	20030330	20031205

20031206 20031207 20031214 20031215 20031217 20040102 20040112 20040113
20040114 20040115 20040118 20040126 20040127 20040128 20040203 20040206
20040207 20040222 20040308 20040316 20040317 20040318 20040319 20041112
20041113 20041206 20041220 20041226 20041227 20050105 20050106 20050108
20050111 20050112 20050116 20050117 20050119 20050120 20050122 20050123
20050124 20050126 20050204 20050210 20050211 20050220 20050221 20050224
20050225 20050228 20050301 20050302 20050308 20050309 20050311 20050312
20050323 20050324 20051124 20051204 20051206 20051209 20051216 20051231
20060101 20060103 20060105 20060114 20060115 20060123 20060125 20060211
20060212 20060225 20060226 20060302 20070119 20070122 20070128 20070202
20070213 20070214 20070222 20070223 20070225 20070226 20070227 20070307
20070316 20070317 20070319 20070324 20071118 20071119 20071202 20071203
20071205 20071213 20071216 20071220 20071227 20071230 20071231 20080101
20080114 20080115 20080117 20080127 20080207 20080209 20080210 20080212
20080213 20080222 20080226 20080229 20080301 20080315 20080328 20081206
20081207 20081211 20081216 20081217 20081219 20081220 20081221 20081231
20090107 20090108 20090110 20090111 20090115 20090118 20090119 20090128
20090203 20090218 20090219 20090220 20090222 20090301 20090302 20090309
20091205 20091209 20091219 20091220 20091228 20091231 20100101 20100102
20100103 20100108 20100117 20100118 20100119 20100128 20100202 20100203
20100205 20100206 20100209 20100210 20100216 20100223 20100224 20100225
20100226 20100227 20101213 20101214 20101220 20101226 20101227 20110107
20110108 20110111 20110112 20110118 20110119 20110121 20110125 20110126
20110127 20110201 20110202 20110208 20110220 20110221 20110225 20110227
20110307 20110321 20110323 20110324 20110331 20111027 20111029 20111030
20111207 20120112 20120116 20120117 20120119 20120120 20120121 20120224
20120229 20120301 20121107 20121108 20121127 20121221 20121222 20121225
20121226 20121227 20121229 20130116 20130121 20130125 20130128 20130208
20130209 20130216 20130217 20130224 20130227 20130307 20130308 20130318
20130319 20131112 20131126 20131206 20131208 20131210 20131214 20131215
20131217 20131224 20131226 20131229 20140102 20140103 20140110 20140118
20140121 20140122 20140125 20140129 20140203 20140205 20140209 20140213
20140214 20140215 20140218 20140219 20140313 20141114 20141126 20141127
20141209 20141210 20141211 20150103 20150106 20150109 20150112 20150124
20150126 20150127 20150130 20150131 20150201 20150202 20150205 20150208
20150209 20150212 20150214 20150215 20150217 20150218 20150219 20150221

20150222 20150225 20150301 20150303 20150305 20150315 20150320 20150321
20150328 20151229 20160112 20160117 20160118 20160122 20160123 20160205
20160208 20160209 20160210 20160215 20160321 20161027 20161119 20161120
20161205 20161212 20161217 20161229 20161230 20170106 20170107 20170114
20170118 20170124 20170131 20170201 20170207 20170209 20170211 20170212
20170213 20170215 20170216 20170310 20170313 20170314 20170315 20170331
20171209 20171212 20171213 20171214 20171215 20171222 20171225 20171230
20180104 20180113 20180116 20180117 20180130 20180201 20180204 20180207
20180217 20180218 20180222 20180302 20180307 20180308 20180309 20180312
20180313 20180314 20180321 20180322 20181115 20181116 20181119 20181120
20181127 20181213 20190109 20190119 20190120 20190129 20190130 20190212
20190218 20190220 20190221 20190227 20190228 20190301 20190302 20190303
20190304 20190310 20190322 20191112 20191201 20191202 20191203 20191206
20191211 20191217 20191218 20191230 20200116 20200118 20200119 20200202
20200206 20200207 20200209 20200213 20200218 20200323 20201030 20201205
20201209 20201216 20201217 20201220 20201225 20210101 20210102 20210103
20210126 20210127 20210131 20210201 20210202 20210203 20210207 20210209
20210211 20210218 20210219 20210222 20211126 20211128 20211208 20211218
20211219 20211224 20220107 20220116 20220117 20220124 20220128 20220129
20220204 20220213 20220214 20220225 20220309 20220312 20221115 20221211
20221215 20221216 20230106 20230116 20230120 20230122 20230123 20230125
20230222 20230223 20230225 20230227 20230228 20230303 20230304 20230311
20230314

Appendix B

Using visibility to estimate snowfall intensity

Previous work from Rasmussen et al. (1999) demonstrates how visibility can be useful for determining snowfall intensity. In their work, they use observations with a high temporal frequency that correspond well to the precipitation rate observations. We had hoped to use the hourly visibility observations from the ASOS stations to refine our precipitation rate definitions. In practice, with the hourly observations, a relationship is less established. This is likely due to the fact that the hourly precipitation observations are time-integrated, whereas the visibility observations are only observed at the top of the hour and are not necessarily representative of the conditions over the whole hour. There are cases where there is a clear relationship between visibility and snow rate (Fig. B.1), but there are also examples where the relationship is more complicated (Fig. B.2). Density plots of visibility and precipitation rate over multiple events and stations indicate that there is not a clear relationship for these observations (Fig. B.3). Based on this analysis, we decided to not use visibility as a proxy for snowfall intensity.

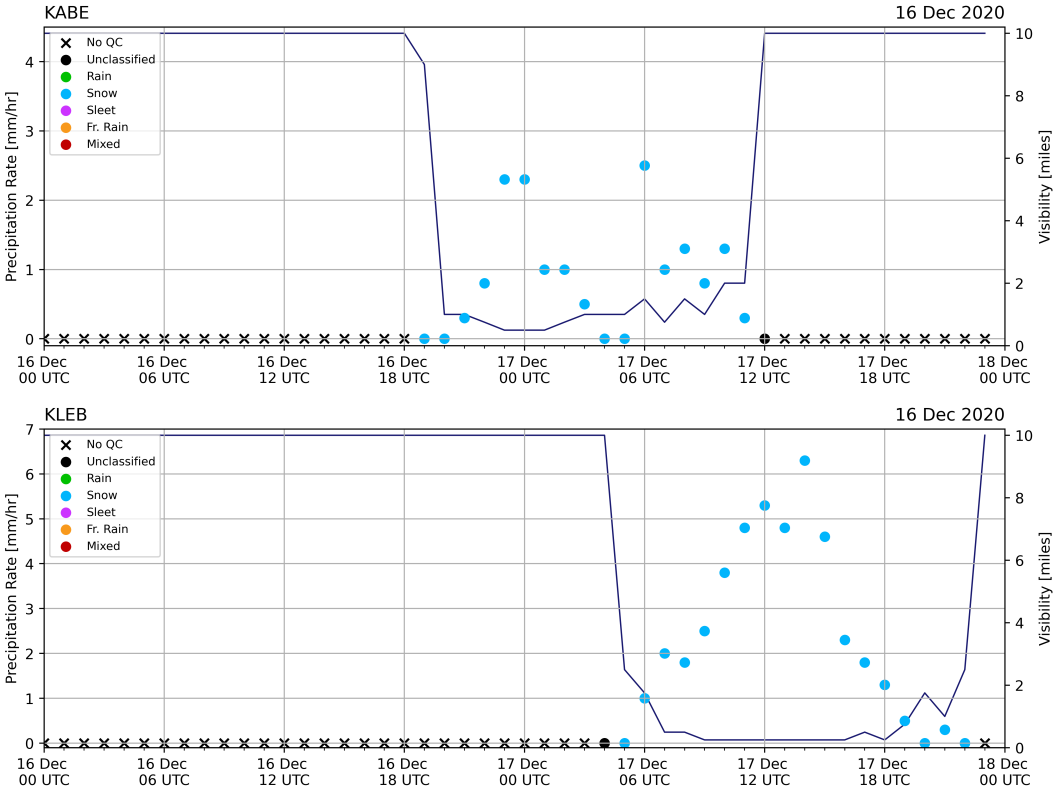

Figure B.1: Two time series of visibility (navy line) and liquid equivalent precipitation rate (points as in legend) from ASOS stations in Lehigh County, PA (KABE; top) and Lebanon, NH (KLEB; bottom) between 16 December 2020 00:00 UTC and 18 December 2020 00:00 UTC. These two examples show a strong relationship between decreased visibility and increased precipitation rate.

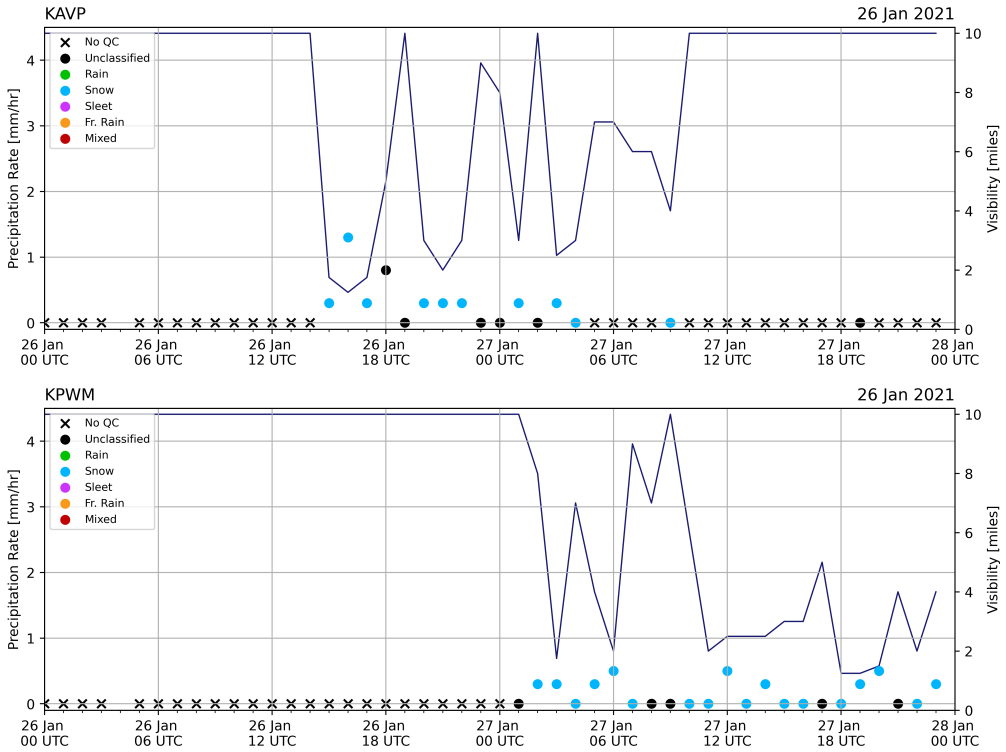

Figure B.2: Two time series of visibility (navy line) and liquid equivalent precipitation rate (points as in legend) from ASOS stations in Scranton, PA (KAVP; top) and Portland, ME (KPWM; bottom) between 26 January 2021 00:00 UTC and 28 January 2021 00:00 UTC. These two examples show a weak relationship between decreased visibility and increased precipitation rate.

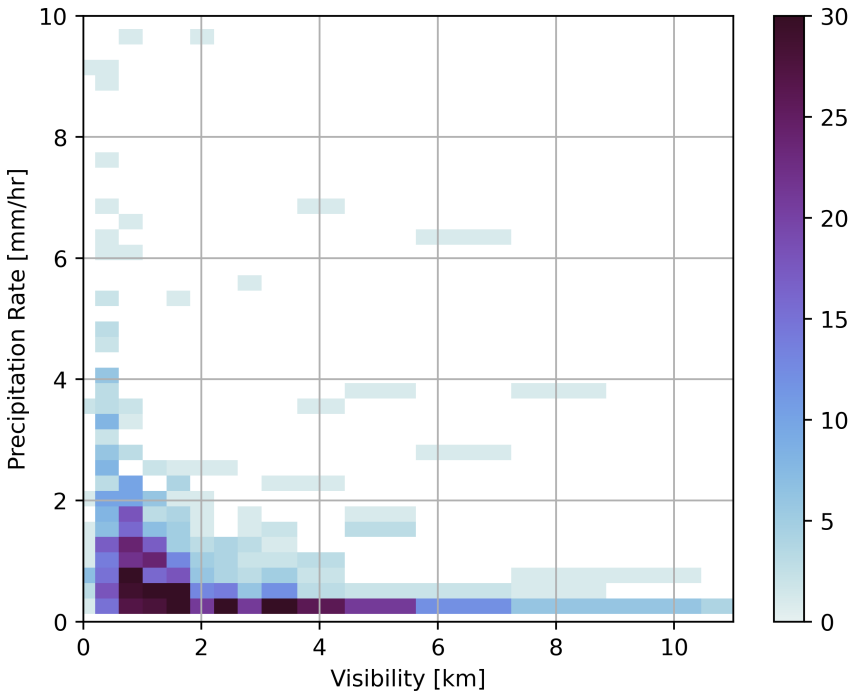

Figure B.3: Density plot of visibility and liquid equivalent precipitation rate from 29 ASOS stations during 7 events in the Northeast US.